A Wide Field Narrowband Survey for Star Forming Galaxies at Different Epochs

Everhardus Antonius Metske Westra

A thesis submitted for the degree of

Doctor of Philosophy

of The Australian National University

Research School of Astronomy & Astrophysics

May 2007

Disclaimer

I hereby declare that the work of this thesis is that of the candidate alone, except where indicated below or in the text of the thesis.

Chapters 2 and 3 of this thesis have been published as papers. Chapter 4 has been submitted to a journal. A list of authors is given at the beginning of each of these chapters.

Chapter 2: C. Lidman reduced the spectroscopic data presented here. The candidate has independently re-reduced these data subsequently.

Chapter 3: The imaging with WFI on the ESO/MPI 2.2 m and the spectroscopy with VLT/FORS2 were taken by ESO staff in service mode. C. Lidman performed preliminary reductions on the WFI frames to remove instrumental signatures. Remaining processing and all subsequent analysis was done by the candidate.

Chapter 4: Some of the AAOmega spectroscopic data were taken by AAO staff as part of service observations.

Further acknowledgements have been made at the end of each chapter.

Eduard Westra
May 2007

Acknowledgements

There are several people who I would like to thank for their assistance during the course of my thesis. First of all, my principal supervisor Heath Jones, for making me part of the survey on which this thesis is built upon. He has always helped me along the way, which is much appreciated. My local supervisor Frank Briggs, for taking over the Stromlo supervisory tasks when Heath was in Sydney. Also Chris Lidman, a close collaborator, for all his help with and suggestions to proposals, data reduction and the survey itself.

I am indebted to my friend Anna Frebel. Her honesty, support, laughs, company and so much more have meant a lot to me. I can not thank you enough for that.

Furthermore, I am extremely grateful to my parents and sister for their ongoing and loving support. It is really a pity that it has been at this large distance. Hopefully this will change in the (near) future.

What would Stromlo be without its students? I have had a lot of fun with them. Thanks for all the great parties, drinks at the pub and all other stuff we did. Also, I have enjoyed playing Stromlo Sunday Social Soccer. It has been good fun, guys!

Also, I would like to thank Mike Pracy, Philip Lah, Brian Schmidt and Frank Briggs for the discussions during our star formation lunches. I appreciate the efforts of Bill Roberts, Kim Sebo, the sysmen/syswomen and all the other members of the computer section. Also, they taught me much about computers and networks.

Thanks to all the academic and general staff members for answering all my questions about life, the universe and everything. I really benefited from the suggestion from Penny Sackett of doing a PhD at Stromlo. If it were not for her, I would have never been here.

I acknowledge the Anglo-Australian Observatory in Sydney for their hospitality and financial support.

Thank you all very very much!

Abstract

Narrowband surveys are a well-established tool for finding star-forming galaxies at different epochs. This thesis presents the Wide Field Imager Lyman Alpha Search (WFILAS), a survey originally designed to find Lyman-α (Lyα) emission-line galaxies at redshift $z \sim 5.7$, and subsequently utilised to find Hydrogen-α (Hα) emitting galaxies at redshift $z \sim 0.24$. The survey covers three 0.25 sq. deg. fields each observed in three narrowband filters, an intermediate band filter (encompassing all narrowband filters), and two broadband filters.

A sample of seven luminous Lyα-emitting galaxies was identified ($L_{\mathrm{Ly}\alpha} \geq 1.8 \times 10^{43}$ ergs), complementing existing surveys by further constraining the bright end of the Lyα luminosity function. Three candidates identified in one of the three fields, the well-studied Chandra Deep Field South, were grouped together, supporting claims of an overdensity at this redshift by other groups.

Two of the seven candidate Lyα emitting galaxies have been confirmed through spectroscopy, one of which is the most luminous at this redshift to date. The spectra of both objects displayed the asymmetric line profiles common in Lyα at these redshifts. Furthermore, tentative evidence of a second Lyα component, redward of the Lyα line was found. Additional high-resolution imaging showed that both objects were unresolved.

Spectroscopic follow-up was used to determine the fraction of Hα-emitting galaxies in two of the fields from a total sample of 707 candidate emission line galaxies. This yielded two independent Hα luminosity functions and star formation densities at $z \sim 0.24$ following corrections for extinction, imaging and spectroscopic incompleteness. These values were found to agree with those of other recent surveys within the limits of uncertainty. A detailed error analysis found that both cosmic variance and differences in selection criteria remain the dominant sources of uncertainty between various Hα luminosity functions at $z \lesssim 0.4$. While the star formation rates were consistent with the typical field galaxy densities probed by the fields, a tentative increase in star formation rate per galaxy with increasing density of star forming galaxies was found. This observation supports galaxy formation scenarios in which galaxy-galaxy interactions are triggers for star formation.

CONTENTS

LIST OF FIGURES

LIST OF TABLES

"Numquam ponenda est pluralitas sine necessitate"
"(It is vain to do with more than which can be done with less)"

or

"Entia non sunt multiplicanda praeter necessitatem"
"(Entities should not be multiplied beyond necessity)"

Occam's Razor

1. INTRODUCTION

1.1 Star Formation History of the Universe

The past decade has witnessed significant changes in what is known about the universe. Measurements of distant supernovae have shown that Hubble expansion is accelerating (Riess et al. 1998; Schmidt et al. 1998; Perlmutter et al. 1999), implying the existence of a "dark energy" as the driving force. The Wilkinson Microwave Anisotropy Probe (WMAP; Bennett et al. 2003) has revealed the best view yet of unfolding primordial structures when the universe was a mere 400,000 years old, through temperature fluctuations in the cosmic microwave background. Locally, large scale surveys such as the Sloan Digital Sky Survey (SDSS; York et al. 2000) and Two degree Field Galaxy Redshift Survey (2dFGRS; Colless et al. 2001) have mapped the nearby universe in unprecedented detail. Together, WMAP, 2dFGRS and SDSS have put tight constraints on the key parameters quantifying the Λ-Cold Dark Matter model (Spergel et al. 2006). In the same period, the limit of the observed universe has increased from redshift 4 to 7 (Fan et al. 2003; Iye et al. 2006). At these redshifts, measurements of the rest-frame UV spectra of quasars around redshift 6 and beyond have shown the neutral hydrogen fraction of the intergalactic medium increasing with redshift (Fan et al. 2002), the first measurement of the Gunn-Peterson effect (Gunn & Peterson 1965). These results have started to constrain the end of the epoch of reionisation at this redshift, whereby reionising radiation from the first sources was sufficient to render the intergalactic medium translucent to electromagnetic radiation.

Likewise, computer models such as the Millennium Simulation (Springel et al. 2005), have greatly improved over the past ten years to provide descriptions of galaxy evolution on both large and small scales with unprecedented detail. The enormous increases in size and resolution seen in recent times allow these simulations to cover sufficient volume to contain representative populations of rare objects such as galaxy clusters and quasars (Baugh 2006).

Following this period of success, the focus of observational cosmology has shifted from constraining fundamental cosmological parameters to understanding the details of galaxy formation and mass assembly. Central to both these processes is the rate of stellar production within individual galaxies, quantified in terms of their star formation rate (in solar masses per year). On global scales, the cosmic star formation history (the production rate of stellar mass per unit volume, as a function of look-back time) provides important constraints on models of galaxy

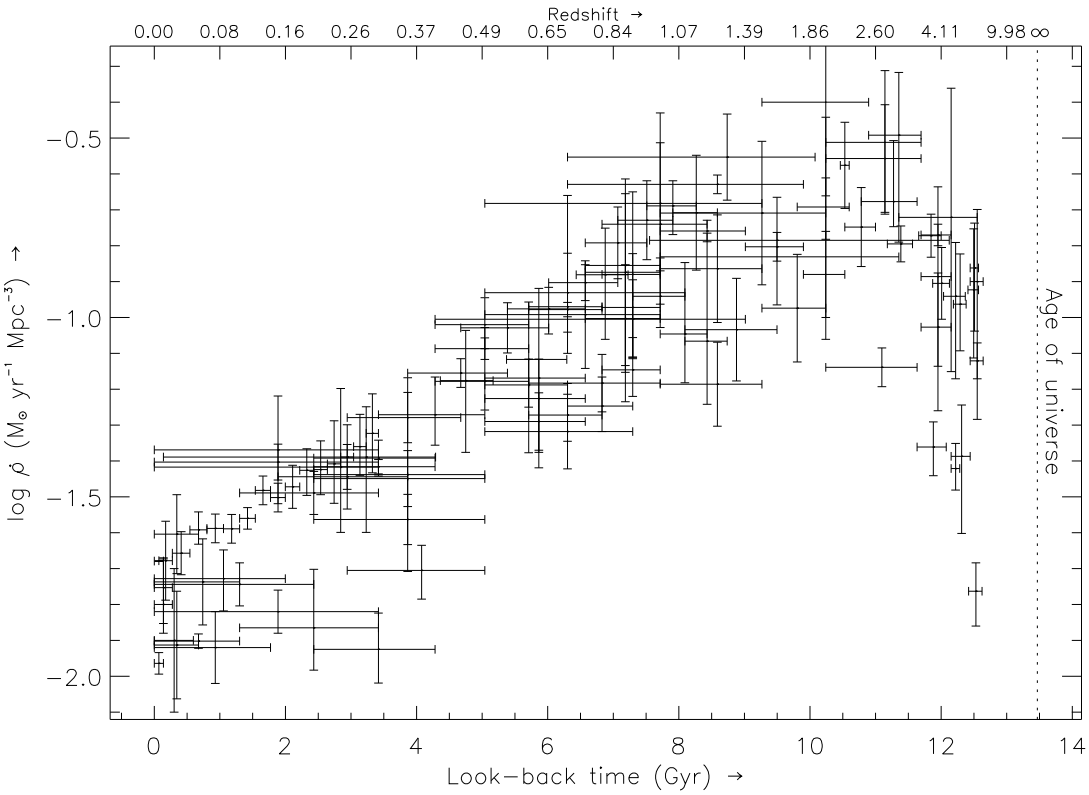

Fig. 1.1: Star formation density as a function of look-back time, after the compilation from Hopkins & Beacom (2006). A wide variety of selection methods, star formation indicators and survey volumes are spanned by the data shown. The vertical dotted line indicates the current estimate of the age of the universe (13.7 Gyr).

formation and evolution (Pei et al. 1999; Somerville et al. 2001). A plot of star formation density against either the redshift or the look-back time is sometimes referred to as the Lilly-Madau (or Madau) diagram, after the seminal papers of Lilly et al. (1996) and Madau et al. (1996). A recent compilation of the star formation history is shown in Fig. 1.1 (after Hopkins & Beacom 2006). It shows that the star formation density peaked around 10 Gyr ago ($z \sim 1-2$) and has rapidly declined subsequently. Observe that the redshift range of $z = 0$ to 1 covers more than half the age of the universe. The earlier third covers the peak in star-forming activity all the way back to the epoch of reionisation ($z \gtrsim 7$). Accurately knowing the rate at which star formation has declined over the past $8-10$ Gyr has important links to both the local stellar mass and metal fraction, as well as for constraining models of galaxy evolution.

There are several issues that need to be borne in mind when viewing these trends in evolution of the star formation density: *(i)* the use of different star formation indicators at various redshifts, *(ii)* the influence of extinction and attenuation by dust, *(iii)* differences in selection criteria and samples between surveys,

and *(iv)* limited volume sampling in some cases and the related impact of cosmic variance.

A variety of star formation indicators exist across the electromagnetic spectrum that either probe the UV flux of newborn stars directly or infer it through indirect means. The use of different star formation indicators is difficult to avoid, because different galaxy rest-frame wavelengths are accessible at different redshifts. The problem is compounded by the comparatively narrow range of wavelengths easily observable from the ground. As a consequence, different indicators are needed to compare the star formation rate at different epochs.

In the absence of dust, the most direct way to infer the star formation rate of a galaxy is by means of its ultra-violet (UV) continuum. This spectral region probes wavelengths where newly formed OB-stars dominate the spectral energy distribution of a galaxy. Alternatively, the hydrogen emission lines, in particular Hα at low redshift (Kennicutt 1998; Kewley et al. 2004), or Lyα at high redshift (Partridge & Peebles 1967) can be used. The hydrogen lines probe the amount of UV continuum due to the absorption of photons shortward of the Lyman limit and subsequent emission upon recombination.

Emission lines are a typical feature in the spectra of star-forming galaxies. The most distinctive ones in the optical, from bluest to reddest, are [OII] $\lambda\lambda$3726,3728, Hβ λ4863, [OIII] $\lambda\lambda$4959,5007 and Hα λ6564[1]. At redshifts beyond 0.4, the Hα line is lost in the night-sky background of the near-infrared. Then other optical emission lines at shorter wavelengths can then be used as indicators, but their use is limited by various factors (Kennicutt 1992). The most important of these emission lines is [OII]. While [OII] line flux is a fair indicator of star formation rate, it is also influenced by the electron temperature and metallicity of the gas from which the stars are formed (Kewley et al. 2004). In the case of Hβ, although the line fluxes of Hα and Hβ have a straightforward ratio in the Balmer decrement (e.g. Osterbrock 1989), extinction, stellar absorption and the fact that Hβ is weaker than Hα (and therefore harder to observe) make it difficult to use Hβ as an indicator[2]. [OIII] generally shows too large a scatter to be particularly useful as a star formation calibrator (Kennicutt 1992).

Both the star formation rates derived from UV and Lyα are heavily influenced by the effects of extinction due to their short wavelengths. The Hα line being in the red suffers to a far lesser degree and has been extensively used to measure star formation in the nearby universe (e.g. Gallego et al. 1995; Tresse & Maddox 1998). Commonly employed extinction laws such as those of Cardelli et al. (1989) or Calzetti et al. (1994) are largely empirical, although Fischera et al. (2003) argue

[1] There are many more, such as [OI] λ6302, [N II] $\lambda\lambda$6550,6585 and [S II] $\lambda\lambda$6733,6718, but these are usually either too faint to be observed at large distances or there does not exist a very good calibration of the line flux to the star formation rate.

[2] However, the fixed flux ratio between the Hα and Hβ lines makes Hβ a very useful line for determining the extinction.

that the latter can be explained by a turbulent interstellar medium. Typical values for extinction in star-forming galaxies are $A_{\mathrm{H}\alpha} = 0.5 - 1.8\,\mathrm{mag}$ (Kennicutt 1998; Tresse & Maddox 1998; Fujita et al. 2003; Ly et al. 2007). This has led some groups to use star formation calibrators unaffected by extinction such as those based on far-infrared or radio continua (e.g. Flores et al. 1999; Cram et al. 1998). However, these are necessarily more indirect as estimators of the total instantaneous star formation rate in a galaxy.

Differences in survey selection also play a crucial role in shaping the samples of galaxies used to determine global star formation rates. For example, broadband-selected redshift surveys select an entire galaxy population biased towards the particular passband used, which may be less or more sensitive to the underlying star-forming population than other selection techniques. In another example, only $\sim 50\,\%$ of the widely used Lyman break galaxies (e.g. Steidel et al. 1995) at redshifts 2 and beyond show the emission line signatures of star formation (Steidel et al. 2000; Shapley et al. 2003; Stanway et al. 2004; Dow-Hygelund et al. 2007). Furthermore, it has been shown that Lyα emitters at redshifts $3 - 6$ have bluer colours than their Lyman break selected counterparts (Shapley et al. 2003; Lai et al. 2007). In the case of emission line selected surveys, different techniques such as the use of objective prisms, narrowband filters or Fabry-Perot interferometers all have differing sensitivities and equivalent width limits. In addition to these peculiarities, there are more obvious survey differences such as depth, sensitivity, image quality, and so forth.

Finally, the different surveys represented in Fig. 1.1 have widely different geometries and volumes, and so they differ in the degree to which cosmic variance plays a role. In the case of smaller survey volumes, natural variations exist due to the inhomogeneous distribution of galaxies due to large scale structure. To overcome this statistical variance (often referred to as cosmic variance) large individual surveys, or a large number of surveys at similar redshifts need to be done to ensure truly representative samples.

1.2 Surveys for Star-Forming Galaxies

The earliest attempts to determine global star formation rates using emission lines in the local universe were undertaken using objective-prism surveys on Schmidt telescopes (e.g. Smith 1975; Gallego et al. 1995). However, Hα-emitting galaxies could only be found to redshifts less than 0.04 due to the sensitivity drop-off at 6850 Å of photographic plates (Zamorano et al. 1994, 1996). Furthermore, the plates had a very low detection sensitivity, further limiting observations to bright galaxies in the local universe. Despite the small aperture, the use of a Schmidt telescope gives the necessary sky coverage, and hence the volume, to yield useful sample sizes of star-forming galaxies from the local universe. Around the same time, various blind narrowband surveys were being undertaken with CCDs on

larger telescopes. While these afforded much greater sensitivities and greater choice of wavelength, they were limited by coverage due to the relative small sizes of the CCDs in use at the time.

Narrowband surveys are a powerful tool to find emission line galaxies at any redshift. Thompson et al. (1995) show in a quantitative manner how emission line galaxies can appear up to several magnitudes brighter through the use of a suitable narrowband filter. This is clearly demonstrated in Fig. 1.2. Here, images of five emission line galaxies at widely different redshift are shown in six different filters: an intermediate band filter, three narrowband filters, and two broadband filters. In each case, the object is significantly brighter in the narrowband filter used to capture the emission line. In Fig. 1.3 the results of spectroscopy for the same galaxies is shown. In all cases it is possible to identify the emission line and thus the redshift of the galaxy. The spectral region covered by the intermediate and narrowband filters are shown in Fig. 1.3.

The night-sky becomes the dominant source of background at wavelengths longer than ~ 6800 Å. As can be seen in the night-sky spectrum of Fig. 1.4, there are groups of night-sky emission lines due to vibrational and rotational transitions of atmospheric hydroxyls (OH) and molecular oxygen. However, there are three dark windows between these OH-bands at 7070 Å, 8150 Å and 9090 Å, in which the night-sky is relatively low. Careful placement of intermediate and/or narrowband filters between these lines greatly reduces the background. Much of the power of narrowband imaging comes from this ability to separate faint galaxy light from contaminating sky background.

Forty years ago Partridge & Peebles (1967) proposed the use of narrowband filters to find young, primordial galaxies. They suggested that these galaxies should have, in addition to a sharp break at the Lyman limit (912 Å), a strong Lyα-line (1216 Å), due to the conversion of ionising photons produced by the hot, young stars to Lyman photons. Various attempts to search for these galaxies used both fixed narrowband filters as well as tunable Fabry-Perot interferometers (e.g. Pritchet & Hartwick 1987; Thompson et al. 1995; Thommes et al. 1998). All were unsuccessful, however, due to insufficient depth and limited volume. The increasing availability of wide-field CCD-mosaic cameras during the late 1990s boosted imaging areas by factors of ~ 20 or so, with corresponding growth in their capacity to find distant galaxies (e.g. Rhoads et al. 2000; Wolf et al. 2001, 2003; Hu et al. 2004; Ouchi et al. 2005). Furthermore, the introduction of narrowband filters physically large enough to cover the unprecedented beam sizes of these cameras has provided larger samples of line-emitting galaxies at redshifts both low (Fujita et al. 2003; Ajiki et al. 2006; Ly et al. 2007) and high (Hu et al. 1999; Rhoads & Malhotra 2001; Ajiki et al. 2003; Kodaira et al. 2003; Ouchi et al. 2005; Iye et al. 2006). At the same time, the advent of large telescopes (8–10 m apertures) with high-throughput spectrographs has enabled the spectroscopic confirmation of distant star-forming galaxies beyond the reach of smaller apertures. At present,

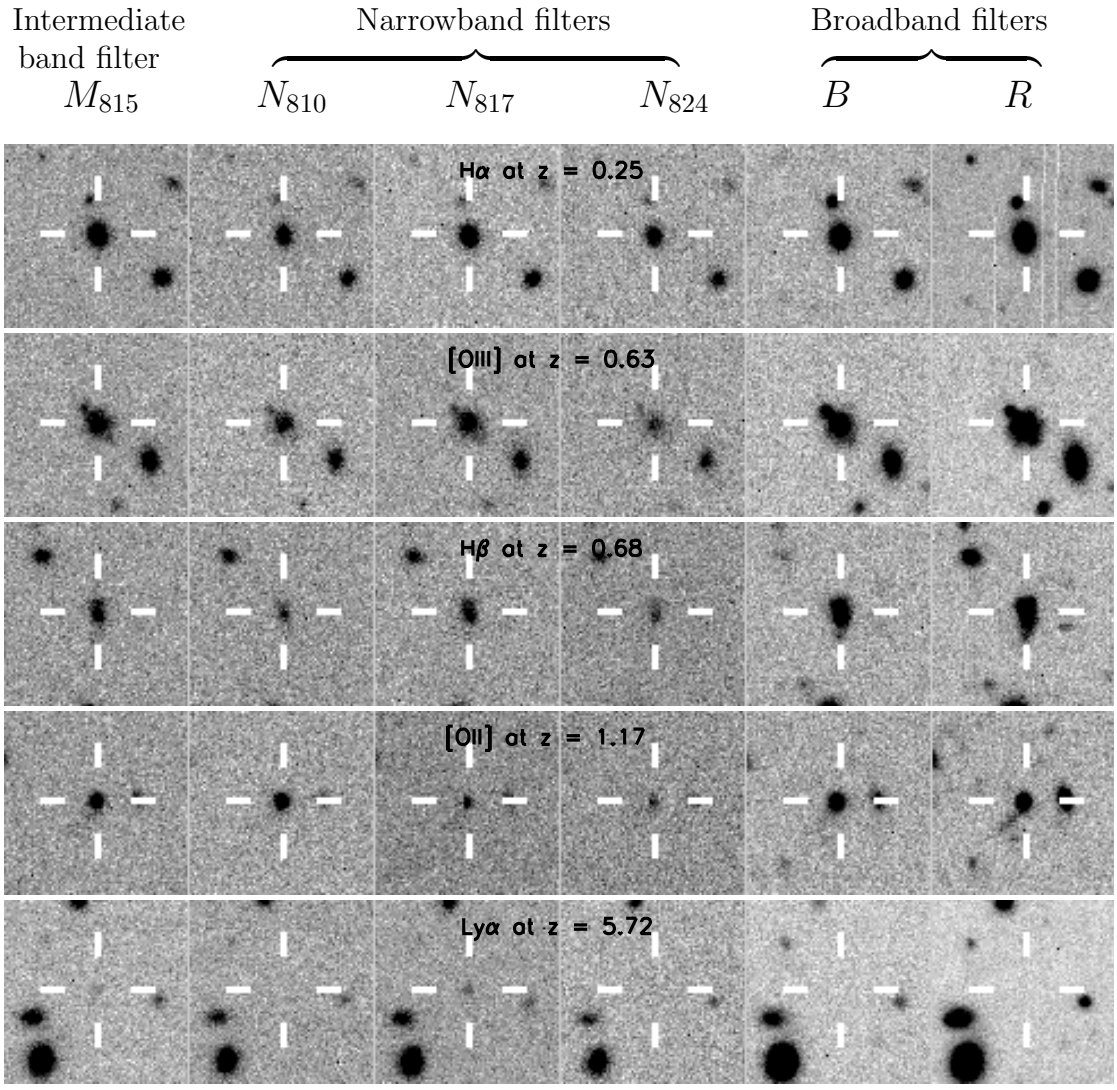

Fig. 1.2: Postage stamp images (19″ on a side) of emission-line galaxies at different redshifts as seen through a narrowband survey. From left to right, frames show intermediate band (8150 Å/220,Å), three narrowband ($FWHM$ = 70 Å at 8100, 8170 and 8240 Å), and broadband B and R images. Observe how the galaxy is the brightest in the narrowband filter where the emission line falls. This is the N_{817} filter in all cases, except for the $z = 1.17$ galaxy, where it is N_{810}. The redshifts of these galaxies have been confirmed using spectroscopy.

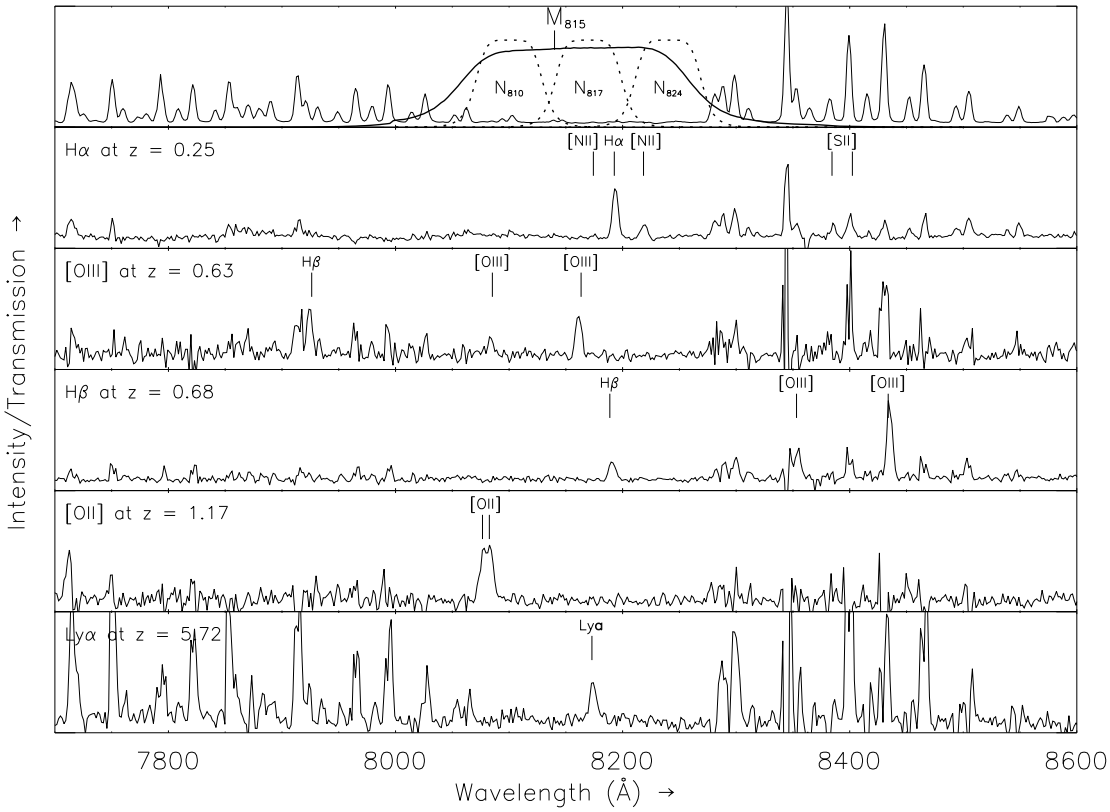

Fig. 1.3: Spectra of the same narrowband galaxies as shown in Fig. 1.2. The top panel shows the night-sky spectrum alongside the intermediate and narrowband filter-profiles used for galaxy selection. Key emission lines are indicated.

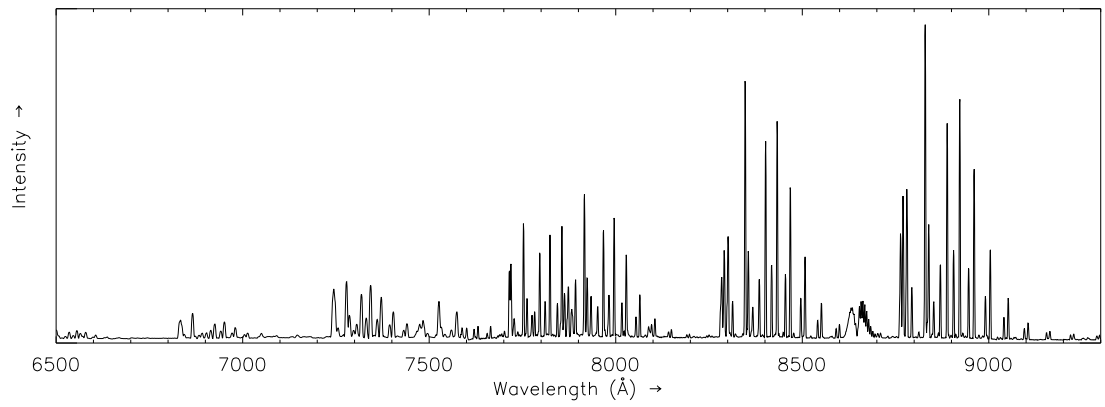

Fig. 1.4: A spectrum of the night-sky background redwards of 6500 Å. Most sky features are emission lines from vibrational and rotational transitions of telluric hydroxyls and molecular oxygen.

the redshift probed by narrowband searches for Lyα-emitting galaxies is being pushed to redshifts $z \sim 7-9$ (e.g. Willis & Courbin 2005; Iye et al. 2006; Cuby et al. 2007). Furthermore, broadband-selected Lyman break galaxies at $z \gtrsim 8$ have been identified (Pelló et al. 2004; Henry et al. 2007), pushing the boundary of the "visible" universe even further.

1.3 A New Wide-Field Narrowband Survey for Star-Forming Galaxies

In 2001 a narrowband survey for Lyα-emitting galaxies at $z \sim 5.7$ commenced called the Wide Field Imager Lyman Alpha Search (WFILAS). It was undertaken as a joint project between a group at the European Southern Observatory (Santiago, Chile) and members of the COMBO-17 team at the Max-Planck-Institut für Astronomie (Heidelberg, Germany). The primary science drivers of the survey were to define the L^* turn-over in the Lyα luminosity function and to ascertain whether these sources could be responsible for reionising the universe at $z \sim 6$. The luminous $L > L^*$ galaxies, that would be needed to accomplish this are rare objects, requiring a large volume to be probed. Large narrowband survey volumes can be achieved by having: *(i)* a large imaging area on the sky, and/or *(ii)* a wide redshift range through the use of multiple filters leading to an extended wavelength coverage.

WFILAS achieves the large imaging area by employing the Wide Field Imager (WFI; Baade et al. 1999) on the ESO/MPIA 2.2 m telescope. With a field-of-view of $0.5^\circ \times 0.5^\circ$ this instrument is one of the largest CCD-mosaic imagers available. Given the moderate aperture of the telescope, the survey is not as deep as those on $8-10$ m telescopes, but sufficiently deep to find the most luminous Lyα-emitting galaxies. Three separate fields were targeted around the sky.

The large redshift range coverage was achieved by using a special set of custom-made intermediate and narrowband filters placed in the low-background window at 8150 Å. The narrowband filters each have a full-width at half-maximum (FWHM) of 70 Å, while the intermediate band filter (FWHM of 220 Å) encompasses the three narrowband filters. The bandpasses of these filters relative to the dark night-sky window they occupy are indicated in Fig. 1.3 (top panel). The combined wavelength coverage (and hence redshift range) of the narrowband filters exceeds that of the intermediate band filters commonly used for this kind of work by previous surveys (∼120 Å; e.g. Ajiki et al. 2003; Hu et al. 2004). Furthermore, the use of additional imaging with the intermediate filter affords a significant reduction in the number of spurious detections in the narrowband images (noise peaks and the like) given the repeated wavelength sampling built into the imaging strategy. The combined large imaging area and broad redshift coverage combined give a Lyα search volume that has only recently been surpassed by Ouchi et al. (2005)

and Murayama et al. (2007) using SuprimeCam on the 8 m Subaru telescope.

Supporting images taken in broadband B and R make it possible to distinguish between emission line galaxies detected in Lyα at $z \sim 5.7$ and foreground [OII] and Hα galaxies at $z \sim 1.2$ and $z \sim 0.24$, respectively. This feature was exploited to furnish a sample of Hα emission line galaxies to measure the star formation density of the nearby universe. The enhanced volume and widely separated fields of WFILAS give the opportunity to remove the contribution of survey systematics over distinct cosmic volumes. Furthermore, the spread of volume helps to mitigate the effects of cosmic variance on star formation density and related quantities..

1.4 Thesis Layout

This thesis describes the Wide Field Imager Lyman Alpha Search (WFILAS), a survey for Lyα-emitting galaxies at $z \sim 5.7$. It also details a survey for Hα-emitting galaxies at $z \sim 0.24$ found through the same narrowband imaging.

In Chapter 2 the discovery and analysis of the first Lyα-emitting galaxy at $z = 5.7$ from WFILAS is presented. The spectrum of this galaxy showed the type of asymmetric line profile commonly seen in Lyα at these redshifts. It also showed a tentative second component redwards of Lyα, indicating an expanding shell of neutral hydrogen surrounding the central Lyα source. Such a feature has only been detected in a handful of Lyα emitters so far. A detailed description of WFILAS in general is deferred to Chapter 3 to preserve publishing chronology of the work. In addition to survey design, Chapter 3 details the analysis of the entire sample of candidate Lyα emitters resulting from WFILAS. Ultimately, seven luminous candidate Lyα-emitting galaxies at $z \sim 5.7$ were found, complementing other deeper but less voluminous surveys. Spectroscopic confirmation of the brightest Lyα-emitting galaxy[3] in the sample is presented and the components of its asymmetric line profile are fit and analysed.

Chapter 4 presents the selection, spectroscopic follow-up and analysis of a large sample of Hα-emitting galaxies at $z \sim 0.24$ selected from the same imaging. The Hα luminosity function and star formation density at this redshift are determined and compared to other Hα surveys at similar redshifts. Furthermore, the influence of the local density on the star formation rate was investigated with respect to both the general galaxy population and star-forming galaxies. While star formation rates were consistent with those expected for the typical field galaxy densities probed, a small increase was detected in denser regions of the star-forming galaxy population.

Concluding remarks and some discussion of future prospects from this work are made in Chapter 5.

[3] To date, not only is this galaxy the most luminous compact Lyα source at redshift 5.7, but also at any redshift. (This comparison excludes so-called Lyα-blobs, which are very luminous, very extended regions of Lyα emission at high redshift, e.g. Steidel et al. 2000).

Chapters 2 and 3 of this thesis were published in *Astronomy & Astrophysics* (Westra et al. 2005, 2006, respectively). Chapter 4 has been submitted to the *Monthly Notices of the Royal Astronomical Society*. In accordance with journal style, each chapter contains an Abstract, Introduction, Conclusion and Bibliography of its own.

References

Ajiki, M., Shioya, Y., Taniguchi, Y., Murayama, T., Nagao, T., Sasaki, S. S., Sumiya, R., Morioka, T., et al., 2006, PASJ, 58, 113

Ajiki, M., Taniguchi, Y., Fujita, S. S., Shioya, Y., Nagao, T., Murayama, T., Yamada, S., Umeda, K., et al., 2003, AJ, 126, 2091

Baade, D., Meisenheimer, K., Iwert, O., Alonso, J., Augusteijn, T., Beletic, J., Bellemann, H., Benesch, W., et al., 1999, The Messenger, 95, 15

Baugh, C. M. 2006, Reports of Progress in Physics, 69, 3101

Bennett, C. L., Halpern, M., Hinshaw, G., Jarosik, N., Kogut, A., Limon, M., Meyer, S. S., Page, L., et al., 2003, ApJS, 148, 1

Calzetti, D., Kinney, A. L., & Storchi-Bergmann, T., 1994, ApJ, 429, 582

Cardelli, J. A., Clayton, G. C., & Mathis, J. S., 1989, ApJ, 345, 245

Colless, M., Dalton, G., Maddox, S., Sutherland, W., Norberg, P., Cole, S., Bland-Hawthorn, J., Bridges, T., et al., 2001, MNRAS, 328, 1039

Cram, L., Hopkins, A., Mobasher, B., & Rowan-Robinson, M., 1998, ApJ, 507, 155

Cuby, J.-G., Hibon, P., Lidman, C., Le Fèvre, O., Gilmozzi, R., Moorwood, A., & van der Werf, P., 2007, A&A, 461, 911

Dow-Hygelund, C. C., Holden, B. P., Bouwens, R. J., Illingworth, G. D., van der Wel, A., Franx, M., van Dokkum, P. G., Ford, H., et al., 2007, ApJ, 660, 47

Fan, X., Narayanan, V. K., Strauss, M. A., White, R. L., Becker, R. H., Pentericci, L., & Rix, H.-W., 2002, AJ, 123, 1247

Fan, X., Strauss, M. A., Schneider, D. P., Becker, R. H., White, R. L., Haiman, Z., Gregg, M., Pentericci, L., et al., 2003, AJ, 125, 1649

Fischera, J., Dopita, M. A., & Sutherland, R. S., 2003, ApJ, 599, L21

Flores, H., Hammer, F., Thuan, T. X., Césarsky, C., Desert, F. X., Omont, A., Lilly, S. J., Eales, S., et al., 1999, ApJ, 517, 148

Fujita, S. S., Ajiki, M., Shioya, Y., Nagao, T., Murayama, T., Taniguchi, Y., Umeda, K., Yamada, S., et al., 2003, ApJ, 586, L115

Gallego, J., Zamorano, J., Aragon-Salamanca, A., & Rego, M., 1995, ApJ, 455, L1+

Gunn, J. E. & Peterson, B. A. 1965, ApJ, 142, 1633

Henry, A. L., Malkan, M. A., Colbert, J. W., Siana, B., Teplitz, H. I., McCarthy, P., & Yan, L., 2007, ApJ, 656, L1

Hopkins, A. M. & Beacom, J. F. 2006, ApJ, 651, 142

Hu, E. M., Cowie, L. L., Capak, P., McMahon, R. G., Hayashino, T., & Komiyama, Y., 2004, AJ, 127, 563

Hu, E. M., McMahon, R. G., & Cowie, L. L., 1999, ApJ, 522, L9

Iye, M., Ota, K., Kashikawa, N., Furusawa, H., Hashimoto, T., Hattori, T., Matsuda, Y., Morokuma, T., et al., 2006, Nature, 443, 186

Kennicutt, Jr., R. C. 1992, ApJ, 388, 310

—. 1998, ARA&A, 36, 189

Kewley, L. J., Geller, M. J., & Jansen, R. A., 2004, AJ, 127, 2002

Kodaira, K., Taniguchi, Y., Kashikawa, N., Kaifu, N., Ando, H., Karoji, H., Ajiki, M., Akiyama, M., et al., 2003, PASJ, 55, L17

Lai, K., Huang, J.-S., Fazio, G., Cowie, L. L., Hu, E. M., & Kakazu, Y., 2007, ApJ, 655, 704

Lilly, S. J., Le Fevre, O., Hammer, F., & Crampton, D., 1996, ApJ, 460, L1+

Ly, C., Malkan, M. A., Kashikawa, N., Shimasaku, K., Doi, M., Nagao, T., Iye, M., Kodama, T., et al., 2007, ApJ, 657, 738

Madau, P., Ferguson, H. C., Dickinson, M. E., Giavalisco, M., Steidel, C. C., & Fruchter, A., 1996, MNRAS, 283, 1388

Murayama, T., Taniguchi, Y., Scoville, N. Z., Ajiki, M., Sanders, D. B., Mobasher, B., Aussel, H., Capak, P., et al., 2007, astro-ph/0702458

Osterbrock, D. E. 1989, Astrophysics of gaseous nebulae and active galactic nuclei (Research supported by the University of California, John Simon Guggenheim Memorial Foundation, University of Minnesota, et al. Mill Valley, CA, University Science Books, 1989, 422 p.)

Ouchi, M., Shimasaku, K., Akiyama, M., Sekiguchi, K., Furusawa, H., Okamura, S., Kashikawa, N., Iye, M., et al., 2005, ApJ, 620, L1

Partridge, R. B. & Peebles, P. J. E. 1967, ApJ, 147, 868

Pei, Y. C., Fall, S. M., & Hauser, M. G., 1999, ApJ, 522, 604

Pelló, R., Schaerer, D., Richard, J., Le Borgne, J.-F., & Kneib, J.-P., 2004, A&A, 416, L35

Perlmutter, S., Aldering, G., Goldhaber, G., Knop, R. A., Nugent, P., Castro, P. G., Deustua, S., Fabbro, S., et al., 1999, ApJ, 517, 565

Pritchet, C. J. & Hartwick, F. D. A. 1987, ApJ, 320, 464

Rhoads, J. E. & Malhotra, S. 2001, ApJ, 563, L5

Rhoads, J. E., Malhotra, S., Dey, A., Stern, D., Spinrad, H., & Jannuzi, B. T., 2000, ApJ, 545, L85

Riess, A. G., Filippenko, A. V., Challis, P., Clocchiatti, A., Diercks, A., Garnavich, P. M., Gilliland, R. L., Hogan, C. J., et al., 1998, AJ, 116, 1009

Schmidt, B. P., Suntzeff, N. B., Phillips, M. M., Schommer, R. A., Clocchiatti, A., Kirshner, R. P., Garnavich, P., Challis, P., et al., 1998, ApJ, 507, 46

Shapley, A. E., Steidel, C. C., Pettini, M., & Adelberger, K. L., 2003, ApJ, 588, 65

Smith, M. G. 1975, ApJ, 202, 591

Somerville, R. S., Primack, J. R., & Faber, S. M., 2001, MNRAS, 320, 504

Spergel, D. N., Bean, R., Doré, O., Nolta, M. R., Bennett, C. L., Dunkley, J., Hinshaw, G., Jarosik, N., et al., 2006, arXiv:astro-ph/0603449

Springel, V., White, S. D. M., Jenkins, A., Frenk, C. S., Yoshida, N., Gao, L., Navarro, J., Thacker, R., et al., 2005, Nature, 435, 629

Stanway, E. R., Bunker, A. J., McMahon, R. G., Ellis, R. S., Treu, T., & McCarthy, P. J., 2004, ApJ, 607, 704

Steidel, C. C., Adelberger, K. L., Shapley, A. E., Pettini, M., Dickinson, M., & Giavalisco, M., 2000, ApJ, 532, 170

Steidel, C. C., Pettini, M., & Hamilton, D., 1995, AJ, 110, 2519

Thommes, E., Meisenheimer, K., Fockenbrock, R., Hippelein, H., Roeser, H.-J., & Beckwith, S., 1998, MNRAS, 293, L6

Thompson, D., Djorgovski, S., & Trauger, J., 1995, AJ, 110, 963

Tresse, L. & Maddox, S. J. 1998, ApJ, 495, 691

Westra, E., Jones, D. H., Lidman, C. E., Athreya, R. M., Meisenheimer, K., Wolf, C., Szeifert, T., Pompei, E., et al., 2005, A&A, 430, L21

Westra, E., Jones, D. H., Lidman, C. E., Meisenheimer, K., Athreya, R. M., Wolf, C., Szeifert, T., Pompei, E., et al., 2006, A&A, 455, 61

Willis, J. P. & Courbin, F. 2005, MNRAS, 357, 1348

Wolf, C., Meisenheimer, K., Rix, H.-W., Borch, A., Dye, S., & Kleinheinrich, M., 2003, A&A, 401, 73

Wolf, C., Meisenheimer, K., Röser, H.-J., Beckwith, S. V. W., Chaffee, Jr., F. H., Fried, J., Hippelein, H., Huang, J.-S., et al., 2001, A&A, 365, 681

York, D. G., Adelman, J., Anderson, Jr., J. E., Anderson, S. F., Annis, J., Bahcall, N. A., Bakken, J. A., Barkhouser, R., et al., 2000, AJ, 120, 1579

Zamorano, J., Gallego, J., Rego, M., Vitores, A. G., & Alonso, O., 1996, ApJS, 105, 343

Zamorano, J., Rego, M., Gallego, J. G., Vitores, A. G., Gonzalez-Riestra, R., & Rodriguez-Caderot, G., 1994, ApJS, 95, 387

2. THE WIDE FIELD IMAGER LYMAN-ALPHA SEARCH (WFILAS) FOR GALAXIES AT REDSHIFT ~ 5.7: I. A SPATIALLY COMPACT Lyα EMITTING GALAXY AT REDSHIFT 5.721[1]

E. Westra, D. H. Jones, C. E. Lidman, R. M. Athreya, K. Meisenheimer, C. Wolf, T. Szeifert, E. Pompei and L. Vanzi, 2005 A&A 430, L21–L24

Abstract

We report the spectroscopic confirmation of a compact Lyα emitting galaxy at $z = 5.721$. A FORS2 spectrum of the source shows a strong asymmetric line with a flux of $5{\times}10^{-17}$ erg s^{-1} cm^{-2}, making it one of the brightest Lyα emitting galaxies at this redshift, and a line-of-sight velocity dispersion of 400 km s^{-1}. We also have a tentative detection of a second, narrower component that is redshifted by 400 km s^{-1} with respect to the main peak. A FORS2 image shows that the source is compact, with a *FWHM* of $0\farcs5$, which corresponds to 3.2 kpc at this redshift[2]. This source is a brighter example of J1236.8+6215 (Dawson et al. 2002, ApJ, 570, 92), another Lyα emitting galaxy at $z \sim 5.2$.

2.1 Introduction

Wide-field imaging surveys with specially selected narrow-band filters are an effective means of discovering high redshift ($z \gtrsim 5$) Lyα emitting galaxies (see Hu et al. 2004, and references therein). Spectra of these galaxies are dominated by a single, asymmetric emission line. One of the strongest arguments for associating this line with Lyman-α (Lyα) is the asymmetry in the line profile (e.g. Stern et al. 2000), which can only be detected if the spectral resolution is high enough ($R \gtrsim 2000$).

The profile of the Lyα line is the end result of emission from HII regions and resonant scattering by HI. The bulk of the Lyα emission comes from the recombination of hydrogen that has been ionised by UV flux of massive stars. Part of the ionisation may be due to shocks (Bland-Hawthorn & Nulsen 2004) or

[1] Based on observations taken at the Cerro La Silla (ESO programs 67.A-0063, 68.A-0363, 69.A-0314 and MPG time) and Cerro Paranal Observatories (ESO program 272.A-5029).

[2] Throughout this Letter, a cosmology with $H_0 = 70$ km s^{-1} Mpc^{-1}, $\Omega_{\rm M} = 0.3$ and $\Omega_\Lambda = 0.7$ is assumed. Magnitudes are on the AB-system.

from an AGN, although in a study of Lyα emitting galaxies at $z \sim 4.5$, Wang et al. (2004) found no evidence of AGN activity. The shape of the line profile is sensitive to the geometry, density and kinematics of both the HII gas, where the line is produced, and the HI gas, where it is scattered (Ahn et al. 2003; Santos et al. 2004). Dust can also play a role. Hence, the Lyα emission line can be viewed as a tool, albeit a rather blunt one, that might be used to constrain the spatial and kinematic distribution of the hydrogen gas in these distant galaxies.

In this letter, we present the $0\farcs5$ resolution seeing-limited imaging and $R \sim 3600$ spectroscopy of a Lyα emitting galaxy that was selected from Lyα emitting candidates in the WFILAS catalog (see Chap. 3).

2.2 WFILAS and Candidate Selection

WFILAS is a survey for bright Lyα emitting galaxies at $z \sim 5.7$. The selection strategy is similar to the successful strategies employed in other Lyα surveys at these redshifts (Ajiki et al. 2003; Rhoads et al. 2003; Hu et al. 2004). WFILAS covers a larger volume ($\sim 1.2\times10^6$ Mpc^3), a larger area ($\sim 1\,\square^\circ$) and has a brighter detection limit (2σ limit magnitude $\sim$24.0–24.5) than these surveys. Hence the candidate Lyα emitting galaxies in the WFILAS catalogue will, on average, be brighter than the Lyα emitting galaxies in these other catalogs.

The survey used the Wide Field Imager (WFI) on the ESO/MPI 2.2m telescope at the Cerro La Silla Observatory and targeted three fields. The WFI consists of a mosaic of eight (4 x 2) 2k x 4k CCDs arranged to give a field of view of $34'$ x $33'$ with a pixel scale of $0\farcs238$ pixel^{-1}. Images were taken with the standard broad-band B and R filters, and four narrower filters - an intermediate-band ($\Delta\lambda = 22$ Å) filter at 815 nm (M_{815}) and three custom-made narrow-band ($\Delta\lambda = 7$ Å) filters with central wavelengths at 810 nm (N_{810}), 817 nm (N_{817}) and 824 nm (N_{824}). They lie in a spectral region where the emissivity of the night-sky is relatively low, which improves the sensitivity to Lyα emission.

Candidate Lyα galaxies are those that appear in one of the narrow band filters, but are undetected in the broad band filters. Given the relatively low signal-to-noise ratios of the candidates, we also require a detection in the intermediate band filter. This limits the number of spurious candidates. We refer the interested reader to Chap. 3 for a description of the observations, reduction and candidate selection.

2.3 Confirmed Lyα Emitter at $z = 5.721$

In a pilot study to test the effectiveness of the selection strategy one of the brighter candidates (J114334.98-014433.9, hereafter S11_13368) was observed with FORS2 on Yepun (UT4) at the Cerro Paranal Observatory (Fig. 2.1).

A pre-image with an intermediate-band filter (13 nm) centered at 815 nm was

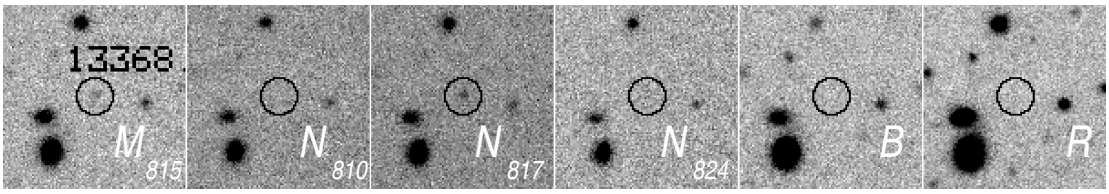

Fig. 2.1: From left to right, thumbnails of the confirmed Lyα emitter S11_13368 at redshift 5.721. Each thumbnail covers a $24'' \times 24''$ region with a pixel scale of $0\overset{''}{.}238\,\mathrm{pix}^{-1}$. The emitter is only detected in the M_{815} and N_{817} images.

taken with FORS2 on 2004 February 16th in which S11_13368 clearly was detected. Figure 2.2 shows a $30''$ region around S11_13368. The *FWHM* of stars in this field are $0\overset{''}{.}5$ and S11_13368 is unresolved.

Three 1200 s exposures were taken on 2004 March 18th with FORS2 using the 1028z grism and a $1''$ slit. Frames were bias-subtracted and flatfielded and were then combined with suitable pixel rejection to remove cosmic rays. The 2D-spectrum (without subtracting the sky lines) and the extracted sky-subtracted spectrum are shown in Figs. 2.3a,b, where one can clearly see a single emission line with a broad red wing. No continuum is detected, implying a 2σ upper-limit for the continuum of $7{\times}10^{-20}\,\mathrm{erg\,s^{-1}\,cm^{-2}\,\AA^{-1}}$ over the rest frame wavelength range 1220 to 1230 Å.

Stern et al. (2000) have reviewed the different ways in which high redshift Lyα can be verified and suggest that line asymmetry is the surest way. Our spectral resolution ($R \sim 3600$) is high enough to securely confirm this asymmetry. This resolving power is also more than adequate to rule out [OII] $\lambda\lambda$3726,3728 at $z = 1.19$, since we do not resolve the line into the close doublet. The separation of this doublet at $z = 1.19$ is 6.1 Å and therefore easily resolvable. Similarly, we can rule out the possibility that the line is [OIII] $\lambda\lambda$4959,5007 at $z = 0.63$, due to the absence of the accompanying line in that doublet. We can also rule out Hα at $z = 0.25$. If the line was Hα, then we should have either detected [N II] and/or some flux in the R-band due to the contributions of Hβ, [OIII] $\lambda\lambda$4959,5007 and the continuum (e.g. Kniazev et al. 2004). In Fig. 2.1, one can see that there is no detection in the R-band image. Given the absence of all of these potential neighbouring features, and also the clear asymmetry of the line, we identify it as Lyα emission at $z = 5.721$.

The integrated line flux of the line derived from the spectrum is $5{\times}10^{-17}\,\mathrm{erg\,s^{-1}\,cm^{-2}}$, making it one of the brightest Lyα emitting sources at this redshift (cf. Ajiki et al. 2003; Rhoads et al. 2003; Maier et al. 2003). The 2σ lower limit on the rest frame equivalent width is ∼100 Å. At $z = 5.721$, this translates to a Lyα luminosity of $1.8{\times}10^{43}\,\mathrm{erg\,s^{-1}}$ suggesting an apparent star-formation rate of 16 $\mathrm{M_\odot\,yr^{-1}}$, using the conversion rate from Ajiki et al. (2003).

Following earlier works (Dawson et al. 2002; Hu et al. 2004), we fit both two-

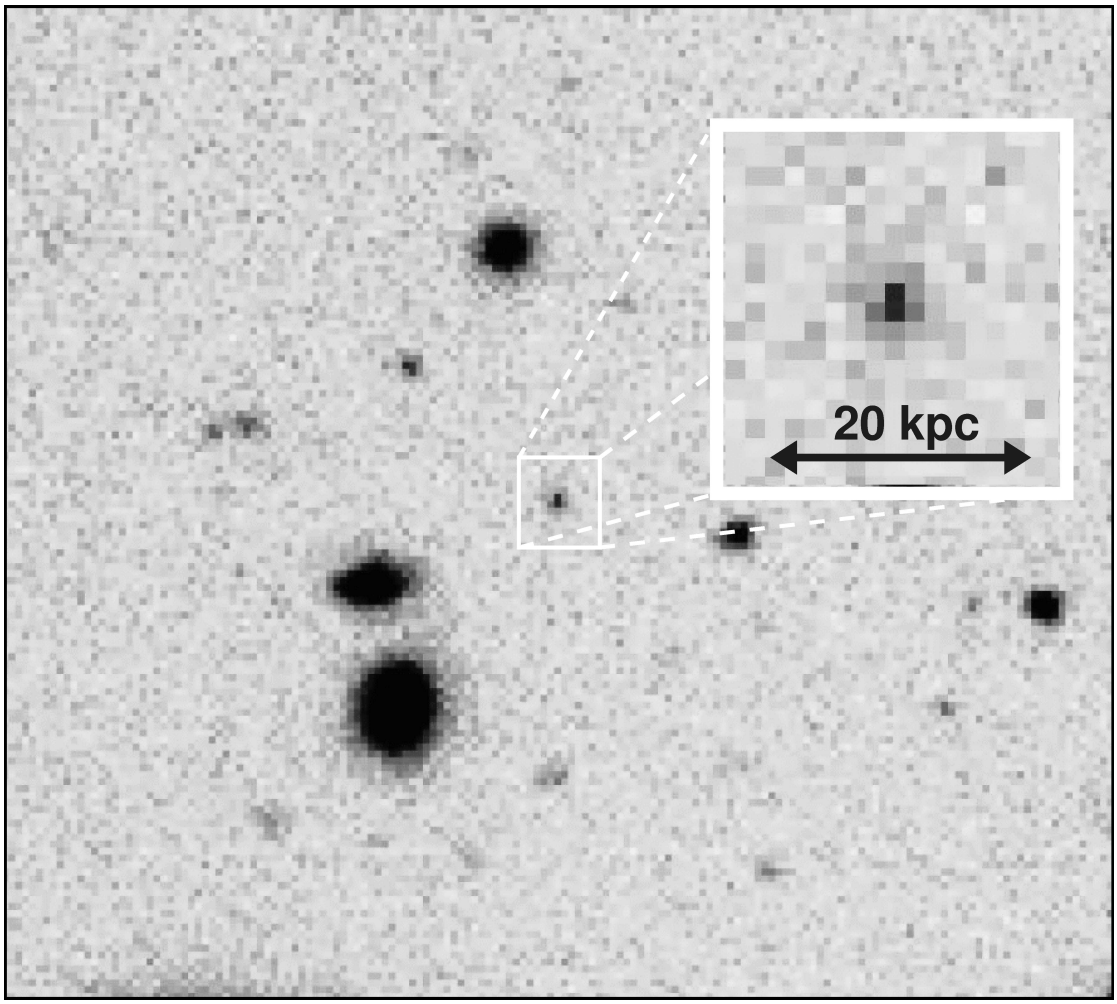

Fig. 2.2: A 30″ x 30″ region around the confirmed Lyα galaxy S11_13368 at $z = 5.721$ from the pre-image taken with FORS2. The image has a pixel scale of $0\farcs252\,\mathrm{pix}^{-1}$. The object is unresolved in this image. The seeing at the time of these observations was $\sim 0\farcs5$. The exposure time was 3600 s.

and single-component models to the Lyα line. The two-component fit consists of a truncated Gaussian with complete absorption bluewards of Lyα line center and a redshifted Gaussian that is not truncated (e.g. Hu et al. 2004). The one-component fit consists solely of a truncated Gaussian (Figs. 2.3b and c). Since the seeing was narrower than the width of the slit, we convolve the model with a Gaussian that has a *FWHM* of 2.3 Å. At 8175 Å this corresponds to a resolution of $R \sim 3600$. We use the Levenberg-Marquardt nonlinear least-squares algorithm to find the best fit.

Two different two-component models fit the data with a similar reduced χ^2_ν values of ~ 1.3. We refer to these two models as the "broad" model and the "spiky" model. In the "broad" model, the redshifted component is broader and weaker and the central component is narrower and stronger in comparison to the

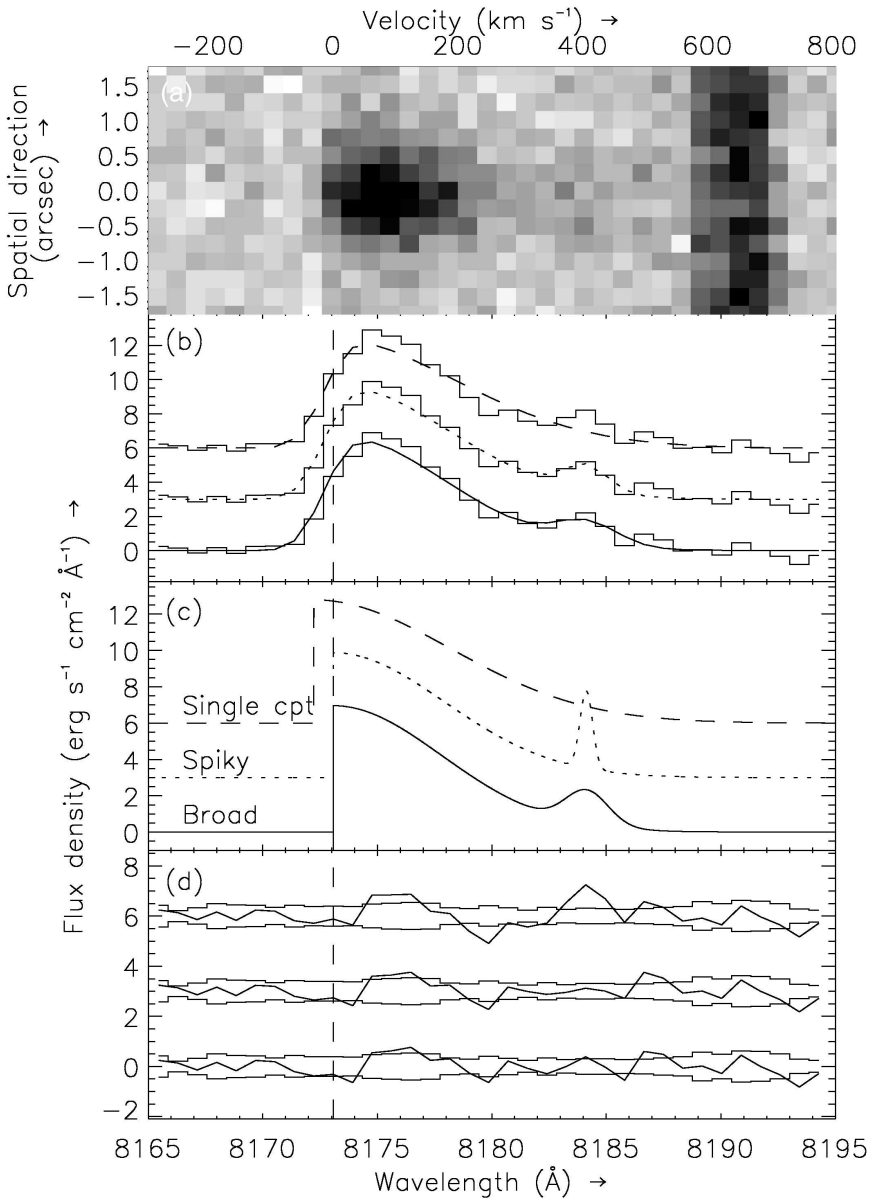

Fig. 2.3: A fit of both one- and two-component models to the profile of the Lyα line. **a**) The two dimensional spectrum centered on the Lyα line. In this unrectified spectrum, the night sky emission lines are not removed. The pixel scale for this image is $0\farcs252\,\mathrm{pix}^{-1}$ in the spatial direction and $0.86\,\text{Å}\,\mathrm{pix}^{-1}$ in the dispersion direction. **b**) Observed Lyα line (*histograms*) with the three best-fitting models. For clarity, the models are offset by 3 $\mathrm{erg\,s^{-1}\,cm^{-2}\,Å^{-1}}$. The two-component models consist of a two components: a broad, truncated Gaussian and a narrower redshifted Gaussian. The one-component model consists of only a broad, truncated Gaussian. See Table 2.1 for the parameters of the 'broad' (*solid*), 'spiky' (*dotted*) and 'single component' (*dashed*) models. **c**) Same model line profiles as in **b**) but before convolution with the instrument profile. **d**) Observed data minus model fit (as plotted in **b**)) residuals, demonstrating a random scatter about the zero flux line. Also shown (*histograms*) is the 1σ-error spectrum from the observed data, which includes both sky- and Poisson noise. Note that the red peak is not N v. At this redshift it would appear around 8334 Å.

Table 2.1. Model fit parameters as described in Section 2.3 and indicated in Figure 2.3.

Component [1]	λ_c [2]	$f_{\rm peak}$ [3]	$FWHM$ [4]	$FWHM$ [5]	Δv [6]	Δv [7]
'Broad' model						
Main peak	8173.1	7.0	11.1	408	...	...
Red peak	8184.2	1.9	2.2	81	+11.1	406
'Spiky' model						
Main peak	8173.1	6.9	11.4	419	...	...
Red peak	8184.1	4.3	0.6	24	+11.0	405
'Single component' model						
Main peak	8172.2	6.8	14.0	514	...	...

[1]Component of the fit

[2]Central wavelength of the fitted component in Å

[3]Peak flux density in 10^{-18} erg s^{-1} cm^{-2} Å^{-1}

[4,5]$FWHM$ of full Gaussian of the profile in Å and km s^{-1}, respectively

[6,7]Line-of-sight outflow velocity in Å and km s^{-1}, respectively.

"spiky" model. After convolving with the instrumental profile both fits have similar residuals. Both models have a central peak at a wavelength corresponding to Lyα at $z = 5.721$. The redshifted component is clearly detected in both models and lies $\sim +400$ km s^{-1} away from the central peak. Given the similar reduced χ^2_ν, we cannot favour one model over the other.

The single-component model has a broader main peak, which is slightly bluer. This model does not fit the profile as well as the two-component cases, particularly in the region of the red peak ($\chi^2_\nu = 2.2$).

Table 2.1 summarises the different model components.

The integrated line fluxes for the two-component models are very similar. If one were to include the flux that was missing from the blue side of the truncated Gaussian, the total a line flux is $8.3{\times}10^{-17}$ erg s^{-1} cm^{-2}. This corresponds to a star-formation rate of ~ 27 M$_\odot$ yr^{-1}, using the conversion rate from Ajiki et al. (2003). The width on the blueward side of the profile is solely due to instrumental broadening.

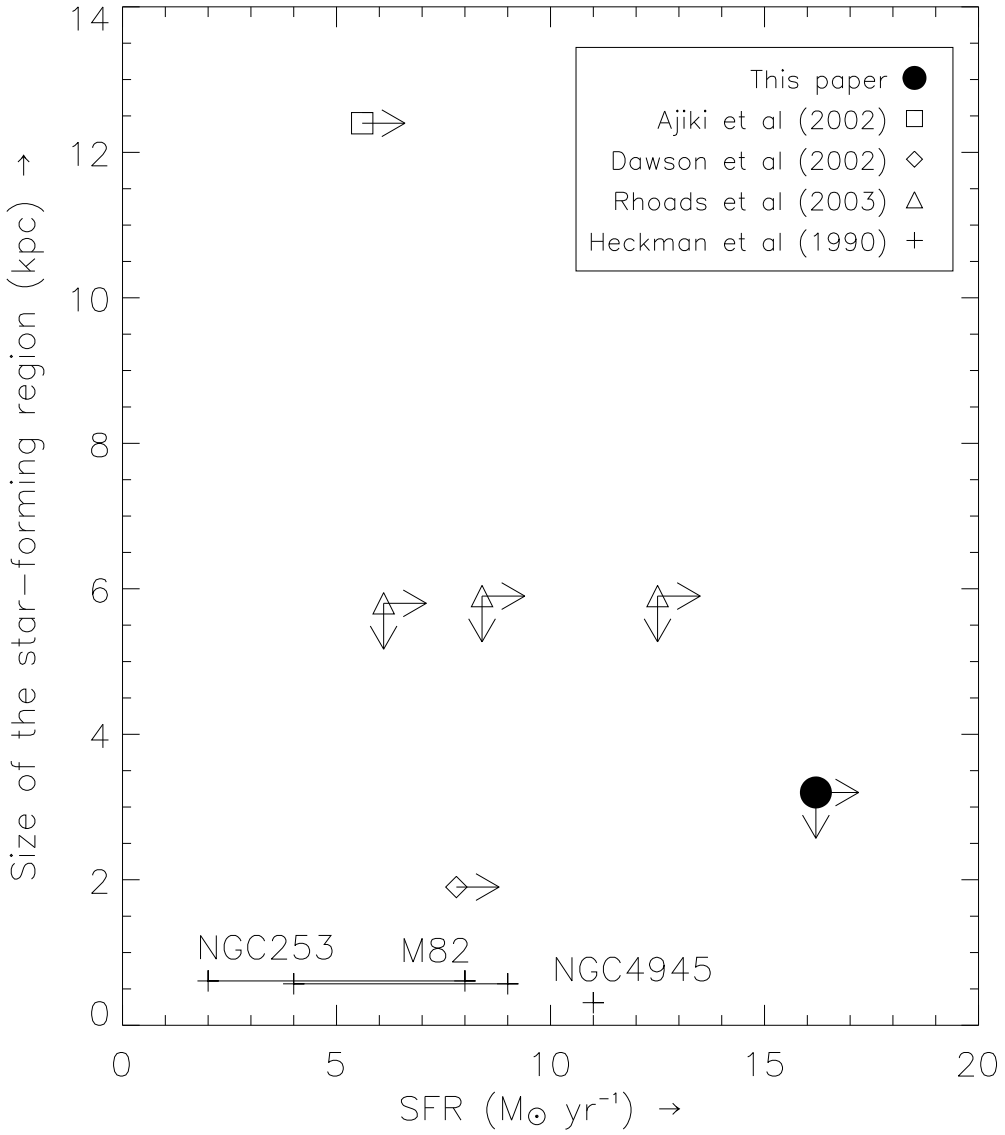

Fig. 2.4: Size of the star-forming region versus the star-formation rate. The SFR of two galaxies from Heckman et al. (1990) is indicated by a bar, as there are two measurements of the SFR. The arrows represent lower-limits to the SFR and upper-limits to the size of the major axis, (due to seeing limited observations). Error-bars are not included. The plus signs represent three well-known local starbursting galaxies (Heckman et al. 1990).

2.4 Discussion

We have presented a medium resolution spectrum of a bright Lyα emitting galaxy at $z = 5.721$. The spectrum consists of a single emission line and no continuum. The line shows a distinct asymmetry, which undoubtedly confirms it as Lyα. We model the line with two components: a one-sided Gaussian and a narrower, redshifted component. The profile of the blue side of the line is entirely defined by the instrument profile.

Generally, the second component is less frequently observed, although it is possible that it has been missed in the spectra of other Lyα emitting galaxies. Most of these spectra were taken at lower resolution and are considerably noisier. A second peak in the Lyα line is a clear signature of an expanding shell of neutral hydrogen (Dawson et al. 2002; Ahn et al. 2003). The strength and shape of the secondary peak depends on the kinematics and the quantity of neutral hydrogen in the expanding shell and the amount and distribution of dust throughout the galaxy (Ahn 2004).

S11_13368 appears to be a brighter and more distant example of J1235.8+6215 at $z = 5.190$ (Dawson et al. 2002). The line profile is strongly asymmetric in both objects, and both suggest a second redshifted component. Both objects are also very compact. However, there are some noteworthy differences. The Lyα line in S11_13368 is considerably broader, and the redshifted component is a lot narrower, even in our "broad" model.

The intrinsic Lyα profile is heavily modified by the surrounding gas and the fraction of the line that is finally observed is very model dependent (Santos 2004; Ahn 2004). In general, it is only a fraction of the intrinsic flux. Hence, star formation rates that are estimated from the observed Lyα flux directly, as they are done in this paper, could drastically underestimate the true star formation rate. Similarly, the centroid of the observed profile is also model dependent. This directly leads to an uncertainty in the redshift of about 0.01, if no other lines are visible, which is usually the case for such high redshift galaxies.

S11_13368, like J1235.8+6215, is very compact. With a projected size of $\sim$ 3 kpc or less, it is comparable to the size of the star forming regions in local starbursting galaxies; however, the star formation rate is much higher. Not all Lyα emitting galaxies at $z \sim 5.7$ are as compact. In Fig. 2.4, we plot apparent size of the star forming region versus the inferred star formation rate for a sample of local starbursts and distant galaxies. The emission line region in LAE J1044-0130 occurs over a region that is an order of magnitude larger than emission line regions in S11_13368 and J1235.8+6215 even though the inferred star formation rate is significantly less. Given that the projected star formation rate per unit area in S11_13368 far exceeds 0.1 $M_\odot\,yr^{-1}\,kpc^{-2}$, it is likely that a hot, enriched starburst-driven gas is outflowing into the halo of S11_13368, facilitating the enrichment of the halo and the escape of Lyman continuum photons (Heckman et al. 2000;

Tenorio-Tagle et al. 1999).

Acknowledgements

The authors wish to thank the Max-Planck-Institut für Astronomie and the DDT grant of the European Southern Observatory for providing the narrow band filters which are crucial to the WFILAS survey. We also like to thank the anonymous referee for his/her useful suggestions and comments, which made us improve the article a lot. D. H. Jones is supported as a Research Associate by Australian Research Council Discovery-Projects Grant (DP-0208876), administered by the Australian National University. C. Wolf was supported by a PPARC Advanced Fellowship. Reduction was done with IRAF, which is distributed by the National Optical Astronomy Observatories, which are operated by the Association of Universities for Research in Astronomy, Inc., under cooperative agreement with the National Science Foundation.

References

Ahn, S. 2004, ApJ, 601, L25

Ahn, S., Lee, H., & Lee, H. M., 2003, MNRAS, 340, 863

Ajiki, M., Taniguchi, Y., Fujita, S. S., Shioya, Y., Nagao, T., Murayama, T., Yamada, S., Umeda, K., et al., 2003, AJ, 126, 2091

Bland-Hawthorn, J. & Nulsen, P. E. J. 2004, arXiv:astro-ph/0404241

Dawson, S., Spinrad, H., Stern, D., Dey, A., van Breugel, W., de Vries, W., & Reuland, M., 2002, ApJ, 570, 92

Heckman, T. M., Armus, L., & Miley, G. K., 1990, ApJS, 74, 833

Heckman, T. M., Lehnert, M. D., Strickland, D. K., & Armus, L., 2000, ApJS, 129, 493

Hu, E. M., Cowie, L. L., Capak, P., McMahon, R. G., Hayashino, T., & Komiyama, Y., 2004, AJ, 127, 563

Kniazev, A. Y., Pustilnik, S. A., Grebel, E. K., Lee, H., & Pramskij, A. G., 2004, ApJS, 153, 429

Maier, C., Meisenheimer, K., Thommes, E., Hippelein, H., Röser, H. J., Fried, J., von Kuhlmann, B., Phleps, S., et al., 2003, A&A, 402, 79

Rhoads, J. E., Dey, A., Malhotra, S., Stern, D., Spinrad, H., Jannuzi, B. T., Dawson, S., Brown, M. J. I., et al., 2003, AJ, 125, 1006

Santos, M. R. 2004, MNRAS, 349, 1137

Santos, M. R., Ellis, R. S., Kneib, J., Richard, J., & Kuijken, K., 2004, ApJ, 606, 683

Stern, D., Bunker, A., Spinrad, H., & Dey, A., 2000, ApJ, 537, 73

Tenorio-Tagle, G., Silich, S. A., Kunth, D., Terlevich, E., & Terlevich, R., 1999, MNRAS, 309, 332

Wang, J. X., Rhoads, J. E., Malhotra, S., Dawson, S., Stern, D., Dey, A., Heckman, T. M., Norman, C. A., et al., 2004, ApJ, 608, L21

3. THE WIDE FIELD IMAGER LYMAN-ALPHA SEARCH (WFILAS) FOR GALAXIES AT REDSHIFT ∼5.7: II. SURVEY DESIGN AND SAMPLE ANALYSIS[1]

E. Westra, D. Heath Jones, C. E. Lidman, K. Meisenheimer, R. M. Athreya, C. Wolf, T. Szeifert, E. Pompei and L. Vanzi, 2006 A&A

Abstract

Context: Wide-field narrowband surveys are an efficient way of searching large volumes of high-redshift space for distant galaxies.
Aims: We describe the Wide Field Imager Lyman-Alpha Search (WFILAS) over 0.74 sq. degree for bright emission-line galaxies at $z \sim 5.7$.
Methods: WFILAS uses deep images taken with the Wide Field Imager (WFI) on the ESO/MPI 2.2 m telescope in three narrowband (70 Å), one encompassing intermediate band (220 Å) and two broadband filters, B and R. We use the novel technique of an encompassing intermediate band filter to exclude false detections. Images taken with broadband B and R filters are used to remove low redshift galaxies from our sample.
Results: We present a sample of seven Lyα emitting galaxy candidates, two of which are spectroscopically confirmed. Compared to other surveys all our candidates are bright, the results of this survey complements other narrowband surveys at this redshift. Most of our candidates are in the regime of bright luminosities, beyond the reach of less voluminous surveys. Adding our candidates to those of another survey increases the derived luminosity density by ∼30%. We also find potential clustering in the Chandra Deep Field South, supporting overdensities discovered by other surveys. Based on a FORS2/VLT spectrum we additionally present the analysis of the second confirmed Lyα emitting galaxy in our sample. We find that it is the brightest Lyα emitting galaxy (1×10^{-16} erg s^{-1} cm^{-2}) at this redshift to date and the second confirmed candidate of our survey. Both objects exhibit the presence of a possible second Lyα component redward of the line.

[1] Based on observations made with ESO Telescopes at the La Silla Observatory (Programmes 67.A-0063, 68.A-0363 and 69.A-0314).

3.1 Introduction

Detections of both galaxies and QSOs at $z \sim 6$ (Fan et al. 2002; Becker et al. 2001; Djorgovski et al. 2001) indicate that the Universe was largely reionised at that epoch. The recent three-year *WMAP* results combined with other cosmological surveys suggest an epoch of reionisation around $z \sim 10$ (Spergel et al. 2006), consistent with both QSO results (Fan et al. 2002) and the epoch predicted by structure formation models (Gnedin & Ostriker 1997; Haiman & Loeb 1998). While the UV contributions of QSOs and AGN are almost certainly not responsible for reionisation (Barger et al. 2003), faint star forming galaxies need to exist in extraordinary numbers if they are to be the cause (Yan & Windhorst 2004). However, analyses of the Hubble Ultra Deep Field failed to find sufficient numbers of faint galaxies to support this idea (Bunker et al. 2004; Bouwens et al. 2005). Therefore, it is crucial to investigate what the contribution to the ionising UV flux is from young stellar populations of star forming galaxies.

Broadly speaking, two classes of star-forming galaxy dominate high redshift surveys: Lyman Break Galaxies (LBGs) and Lyman-α Emitters (LAEs). LBG surveys, which now number in the thousands of objects at $z = 3$ to 5, find clumpy source distributions and a two-point angular correlation function indicative of strong clustering (Giavalisco & Dickinson 2001; Foucaud et al. 2003; Adelberger et al. 2003; Ouchi et al. 2004; Hildebrandt et al. 2005; Allen et al. 2005). LAEs also show evidence for clustering although many of the LAE surveys target fields surrounding known sources such as proto-clusters, radio galaxies and QSOs (e.g. Steidel et al. 2000; Møller & Fynbo 2001; Stiavelli et al. 2001; Venemans et al. 2002; Ouchi et al. 2005). On average, LAEs number $1.5 \times 10^4\,\mathrm{deg}^{-2}$ per unit redshift down to $1.5 \times 10^{-17}\,\mathrm{erg\,s^{-1}\,cm^{-2}}$ at $z = 3.4$ and 4.5 (Hu et al. 1998). Also, their consistently small size ($\lesssim 0.6\,h^{-1}\,\mathrm{kpc}$) suggests they are subgalactic clumps residing in the wind-driven outflows of larger unseen hosts (e.g. Bland-Hawthorn & Nulsen 2004). Such mechanisms provide a straightforward means of UV photon escape from the host galaxy, efficiently reionising the surrounding IGM in a way than ordinary LBGs can not.

The most efficient way to find LAEs is through imaging surveys using a combination of broad- and narrowband filters. The advent of wide field cameras has allowed systematic imaging searches that have been carried out to build up samples of candidate LAEs at high redshifts (e.g. Rhoads et al. 2003; Ajiki et al. 2003; Hu et al. 2004; Wang et al. 2005). The availability of high throughput spectrographs on 8 to 10 m-class telescopes has enabled the spectroscopic confirmation of these galaxies. Such direct imaging searches typically cover $10^2 - 10^3$ times the volume of blind long-slit spectroscopic searches (e.g. Table 4 in Santos et al. 2004). Furthermore, candidates from narrowband surveys *always* have an identifiable emission feature that is well separated from sky lines courtesy of the filter design. This is in contrast to other methods, including the widely-used "dropout" technique (e.g.

Steidel et al. 1999).

The narrowband filter design leads to a higher candidate LAE selection efficiency than other techniques. The only way to secure the identification of the emission line is spectroscopic follow-up. The most common low redshift interlopers are the emission line doublets of [OII] $\lambda\lambda$3726,3728 and [OIII] $\lambda\lambda$4959,5007. These can be identified by obtaining spectra with a resolution $R \gtrsim 1500$ to separate the line pair. Other emission lines, such as Hα and Hβ, can be identified by neighbouring lines. The narrowband technique has been successfully applied by many authors in order to discover galaxies at redshift 5−6 (e.g. Ajiki et al. 2003; Maier et al. 2003; Rhoads et al. 2003; Dawson et al. 2004; Hu et al. 2004) and to locate galaxies at redshift 6−7 (Cuby et al. 2003; Kodaira et al. 2003; Stanway et al. 2004). Likewise, we employ the narrowband technique in the Wide Field Imager Lyman-Alpha Search (WFILAS) to find galaxies at $z \sim 5.7$. In Paper I in this series (see Chap. 2), we described a compact LAE at $z = 5.721$ discovered by our survey.

In this Paper, we describe the survey design and sample analysis of WFILAS. In Sect. 3.2 we describe the scope of the survey and the observing strategy. The data reduction is described in Sect. 3.3. Section 3.4 outlines the candidate selection and Sect. 3.5 outlines sample properties and comparison to other surveys. We discuss the spectroscopic follow-up of two candidates in Sect. 3.6. Throughout this paper we assume a flat Universe with $(\Omega_{\rm m}, \Omega_\Lambda) = (0.3, 0.7)$ and a Hubble constant $H_0 = 70\,{\rm km\,s^{-1}\,Mpc^{-1}}$. All quoted magnitudes are in the *AB* system (Oke & Gunn 1983)[2].

3.2 WFILAS Survey Design and Observations

The sky area surveyed by the WFILAS is ∼0.74 sq. degree. We observed three fields in broadbands B, R and in an intermediate width filter centred at 815 nm encompassing three narrowband filters (Fig. 3.1). The adoption of an additional intermediate width filter encompassing the multiple narrowband width filters is a novel approach compared to previous narrowband surveys. The application of the intermediate band filter enables us to drastically reduce the number of spurious detections in the narrowband filters. The narrow width of the narrowband filters ($FWHM = 7$ nm) gives a prominent appearance to emission line objects. Furthermore, the three chosen fields are spread across the sky to enable us to average out variations in cosmic variance. Our search has covered one of the largest co-moving volumes compared to other surveys. Table 3.1 compares WFILAS with other published surveys.

The observations were taken with the Wide Field Imager (WFI; Baade et al. 1999) on the ESO/MPI 2.2 m telescope at the Cerro La Silla Observatory, Chile.

[2] $m_{AB} = -2.5 \log f_\nu + 48.590$, where m_{AB} is the *AB* magnitude and f_ν is the flux density in ${\rm ergs\,s^{-1}\,cm^{-2}\,Hz^{-1}}$

Table 3.1. Narrowband surveys for Lyα at $z = 5.7$

Survey	Fields	Total Area (sq. degree)	Narrowband Filters	Filter Width (Å)	Co-moving Volume ($Mpc^3 3$)	Narrowband Detection Limit (μJy)
LALA (Rhoads & Malhotra 2001)	1	0.19	2	75	0.2×10^6	0.41
CADIS (Maier et al. 2003)	4	0.11	8−9[a]	20	0.04×10^6	3.33
SDF (Ajiki et al. 2003)	1	0.26	1	120	0.2×10^6	0.14
SSA22 (Hu et al. 2004)	1	0.19	1	120	0.2×10^6	0.30
WFILAS (this paper)	3	0.74	3[b]	70	1.0×10^6	1.06–1.74

[a]CADIS is based on imaging with a tunable Fabry-Perot interferometer scanning at equally spaced wavelength steps (Hippelein et al. 2003).

[b]An additional encompassing mediumband filter was used here.

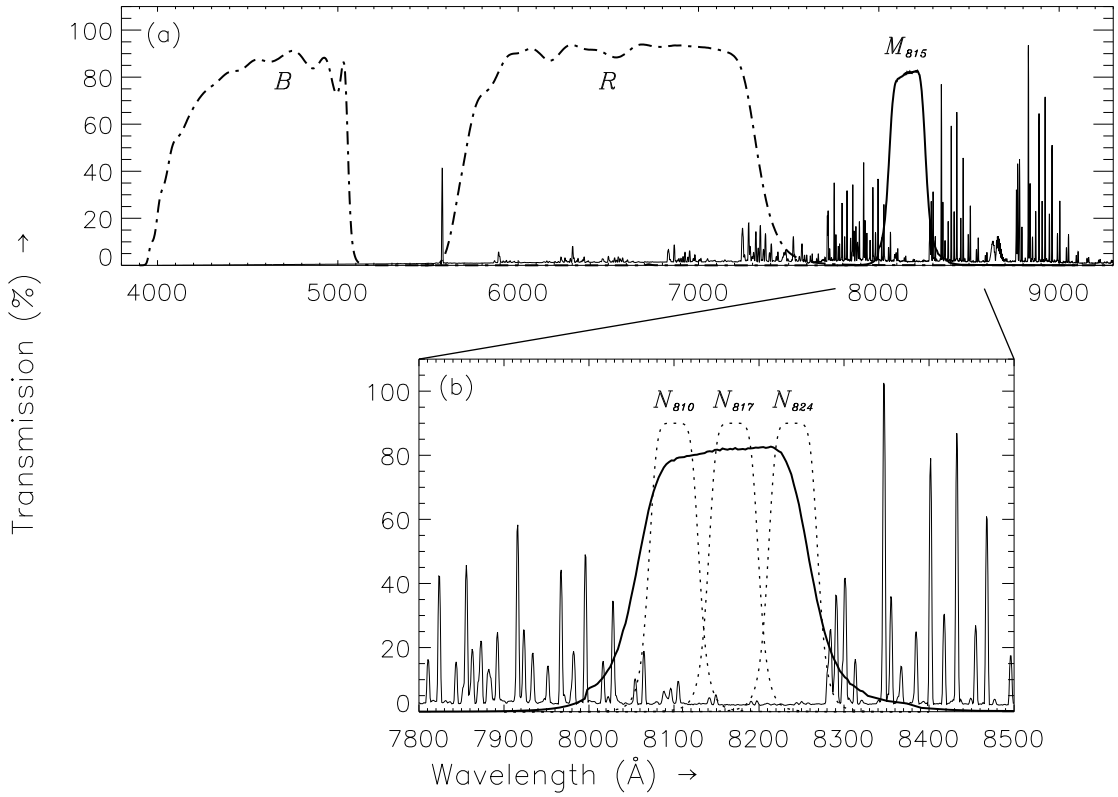

Fig. 3.1: Filter set used for the WFILAS Survey. **a)** The broadband BR and intermediate M_{815} (815/22 nm) passbands. **b)** The M_{815} intermediate passband (*solid* line) and three purpose-built narrowbands N_{810} (810/7), N_{817} (817/7) and N_{824} (824/7), shown over the wavelength region targeted for Lyα line detections. The transmission curves of the narrowband filters are for illustrative purposes only. The OH night sky line background is also shown.

The data were taken over 65 separate nights from 2001 January 19 to 2003 December 1. The WFI is a mosaic of eight (4×2) 2k $\times$ 4k CCDs arranged to give a field of view of $34' \times 33'$. The pixels are $0\farcs238$ on a side.

As WFILAS was planned as joint project of ESO Santiago and the COMBO-17 team at MPIA Heidelberg, three fields were selected to overlap with the COMBO-17 survey, i.e. their extended Chandra Deep Field South (CDFS), SGP (South Galactic Pole) and S11 fields. The coordinates of the field centres and the exposure times in each of the filters for each field are given in Table 3.2. All three fields are at high Galactic latitude ($|b| > 54°$) and have extinctions less than $E(B-V) = 0.022$ mag (Schlegel et al. 1998).

We employ standard broadband B and R filters. The intermediate band ($FWHM = 22$ nm) observatory filter is centred at 815 nm. The three custom made narrowband ($FWHM = 7$ nm) filters are centred at 810 nm, 817 nm and 824 nm. The transmission profiles of the filters are shown in Fig. 3.1. The intermediate and narrowband filters are designed to fit in the atmospheric 815 nm OH-airglow

Table 3.2. WFILAS fields, filter set exposure times and detection limits.

Filter	Passband/ *FWHM* (nm)	**CDFS field** $03^h\ 32^m\ 25\overset{s}{.}134$ $-27°\ 48'\ 49\overset{''}{.}75$			**S11 field** $11^h\ 42^m\ 59\overset{s}{.}933$ $-01°\ 42'\ 46\overset{''}{.}44$			**SGP field** $00^h\ 45^m\ 55\overset{s}{.}024$ $-29°\ 34'\ 55\overset{''}{.}05$		
		(*a*)	(*b*)	(*c*)	(*a*)	(*b*)	(*c*)	(*a*)	(*b*)	(*c*)
Narrowband N_{810}	810/7	48.0	0.57	0.79	44.4	0.55	0.80	31.5	0.87	1.03
Narrowband N_{817}	817/7	41.1	0.55	0.79	79.9	0.53	0.92	0.0	-	-
Narrowband N_{824}	824/7	41.0	0.72	0.80	43.5	0.81	0.87	42.8	0.62	0.89
Mediumband M_{815}[a]	815/20	52.7	0.29	0.85	33.3	0.38	0.88	18.9	0.41	0.90
Broadband B[a]	458/97	5.0	0.07	1.09	9.4	0.07	0.98	10.0	0.14	1.22
Broadband R[a]	648/160	15.1	0.05	0.75	21.2	0.07	0.75	21.5	0.07	0.76

(*a*)Total exposure time (ks)

(*b*)Flux for a 2σ detection on 6 pixel diameter aperture (μJy)

(*c*)Final seeing ($''$), in each filter

[a]Broadband B and R and part of the intermediate band M_{815} taken from the COMBO-17 survey (Wolf et al. 2004)

Table 3.3. The median, first and last decile of background and seeing for the WFILAS narrowband imaging for all three fields combined.

Filter	No. of Frames	Background (μJy/$\square''$) 10%	50%	90%	Seeing ($''$) 10%	50%	90%
N_{810}	92	17	27	36	0.65	0.79	1.12
N_{817}	75	19	30	41	0.64	0.84	1.16
N_{824}	77	17	27	36	0.63	0.80	1.10
M_{815}	80	17	22	33	0.65	0.83	1.09

One pixel corresponds to $0\overset{''}{.}238$.

window, where the brightness of the sky background is low and hence favourable to detect Lyα emission at redshift $\sim$5.7. The data taken with the intermediate band filter confirm detections of the Lyα line in one of the narrowband filters. The broadband B and R data, which were taken from the COMBO-17 survey (Wolf et al. 2004), are used to confirm the absence of continuum blueward of the Lyα line and to avoid sample contamination by lower redshift emission line galaxies (e.g. Hα at $z \sim 0.24$, or [OII] at $z \sim 1.2$).

To establish the photometric zero-point of the intermediate and narrowband filters two spectrophotometric standard stars (LTT3218 and LTT7987; Bessell 1999) were observed.

Between 10–50 exposures were taken for each intermediate and narrowband filter for each field. The exposure times varied between 1000 and 1800 sec per frame, with a typical exposure time of around 1600 sec. All frames are background-limited despite the low night sky emission in this spectral region. The median, first and last decile of both seeing and background are given in Table 3.3.

3.3 Data Reduction

The data were processed with standard IRAF[3] routines (MSCRED TASK) and our own specially designed scripts. The initial steps in the reduction process consist of removing the zero level offset with bias frames, normalising pixel-to-pixel sensitivity differences with twilight flatfield frames and removal of fringes with fringe frames. During these steps, the 8 CCDs that make up a single WFI image are treated independently. These processes are described in detail below.

[3] IRAF is distributed by the National Optical Astronomy Observatories, which are operated by the Association of Universities for Research in Astronomy, Inc., under cooperative agreement with the National Science Foundation.

Normally, the overscan region of the science frames can be used to remove the zero level offset. However, it was noticed that the bias frames contained significant intermediate scale structure (10-30 pixels). To remove this, bias frames were taken on every day of our observations and averaged into a bias frame for that day. In order to minimise the noise added to the data by subtracting the bias, the bias frames were smoothed by 5 pixels and 30 pixels in horizontal and vertical direction of the CCDs, respectively, and subsequently medianed. The structures are stable over periods of several months. Therefore, it was possible to use bias frames from different nights without degrading the quality of the data.

Typically, five twilight flatfield frames were taken in one night for one or more filters. The frames were medianed and the science data was divided by the median. Hence pixel-to-pixel sensitivity differences were removed. The structure in the individual flatfield frames was stable over a period of several weeks. Frames taken on different nights could thus be reused. Any differences between flatfield frames were due to the appearance or disappearance of dust features, or large scale illumination differences. The differences rarely amounted to more than a few percent.

The raw data in the intermediate and narrowband filters show fringe patterns with amplitudes of up to 10% which was only partially removed after the data had been flatfielded. To entirely remove the fringe pattern, we subtracted a fringe frame created from 10–30 science frames. The fringing is very stable over time, so we were able to use data spanning several months. Certain science frames still show fringe patterns because they are contaminated by either moonlight or twilight. Residual differences in the level of the background between the different CCDs were removed by subtracting the median background level from each CCD.

To produce the final deep images we only used images with a seeing of less than 5 pixels ($=1\farcs2$) and without significant residual fringing. To make the combining of the images possible, we had to apply an astrometric correction based on stars from the USNO CCD Astrograph Catalogue 2 (UCAC2; Zacharias et al. 2004) in the three observed fields. The frames have a set pixel scale of $0\farcs238$ pixel^{-1} with North up and East left. The images were weighted according to their exposure time and combined using the IRAF "mscstack" routine rejecting deviant pixels. Table 3.2 summarises the depth, image quality and total exposure time, for each coadded frame.

3.4 Sample Selection and Completeness

3.4.1 Photometry and Noise Characteristics

Initial source catalogues were created for each of the 8 narrowband images. Each catalogue contains the photometry for the sources in all 6 filters. We used the *SExtractor* source detection software (version 2.3.2, double image mode; Bertin

& Arnouts 1996). Sources were selected when at least 5 pixels were 0.8σ above the noise level in the narrowband image used for detection. The photometry was measured in two apertures, 6 and 10 pixels in diameter ($=1\farcs4$ and $2\farcs4$, respectively). The 6 pixel aperture was used to maximise the signal-to-noise of the flux of the objects, while the larger 10 pixel aperture was used for the more accurate determination of the total flux and hence the star formation rate.

Some authors have found that *SExtractor* underestimates flux uncertainties (Feldmeier et al. 2002; Labbé et al. 2003). *SExtractor* estimates the uncertainties using various assumptions that are often not valid (e.g. perfect flatfielding, perfect sky subtraction). The pixel-to-pixel noise in our data is slightly correlated because the scatter in the counts summed in 6 pixel apertures is about 10% higher than what one would derive from the measured pixel-to-pixel RMS.

We devised a method to correct the uncertainties given by *SExtractor* to their true values as follows. First, sources with flux in all filters and their M_{815} magnitude between 16 and 23 were selected. Sources brighter than $M_{815}=16$ are typically saturated, while those fainter than $M_{815}=23$ are incomplete (see Sect. 3.4.3 for a further discussion of incompleteness). The M_{815}–N colour (where N is any of narrowband filters N_{810}, N_{817}, or N_{824}) is the same for any flat continuum source. Therefore, the spread in the M_{815}–N colour will be the same as the true flux uncertainty from the two contributing filters. Next, the sources were binned into 200-source bins based on their M_{815} magnitude. In Fig. 3.2 we plot the M_{815}–N colour versus the M_{815} magnitude of one of our S11 catalogues. Mean values for the M_{815}–N colour, M_{815}, N magnitude and the mean of the *SExtractor* uncertainty were calculated for each bin. The uncertainty in the colour for each object was determined by adding the uncertainty of M_{815} and N in quadrature ($\sigma_{col}^2=\sigma_M^2+\sigma_N^2$). The interval in which 68.3% of the objects were closest to this mean colour was used to infer the actual 1σ colour uncertainty. We assumed that the ratio between the old uncertainties σ_M and σ_N was the same for the new uncertainties σ'_M and σ'_N. We related between the new and old uncertainty in the intermediate and narrowband flux using the function $\sigma'_{\rm filter}=\sqrt{a^2+(b\sigma_{\rm filter})^2}$, where a is the zero-offset for the uncertainty in the flux of bright sources and b is the ratio between the new and old uncertainty for the flux of the faintest sources. The parameters a and b correspond to imperfections in the photometry and wrongly assumed background by *SExtractor*, respectively.

Typically, the correction factors are moderate (between $\sim$30$-$50%) for the faint sources in the catalogues. Even though the correction factors are moderate, we assume that the corrections for the uncertainties in the broadband B and R are irrelevant, since they are used in a different way than the intermediate and narrowband images (see Sect. 3.4.2).

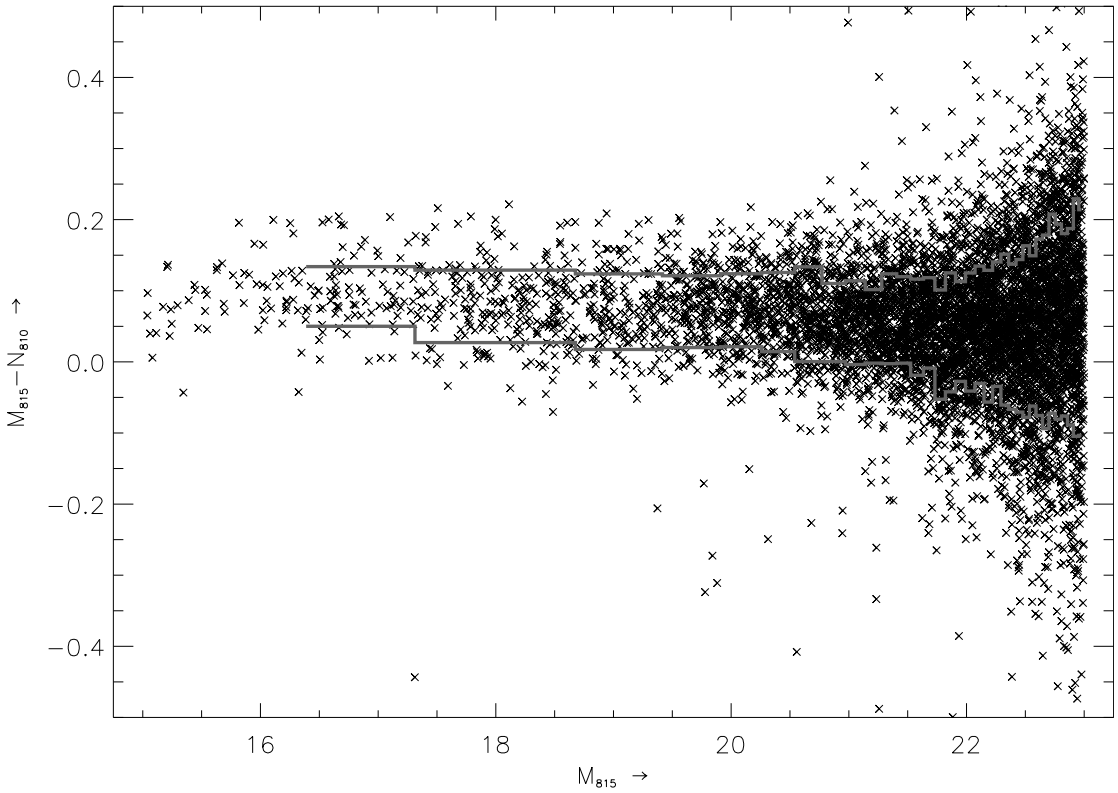

Fig. 3.2: M_{815}–N colour as seen in the S11 field with the N_{810} filter as the detection image. The mean colour term is ∼0.05. The heavy bold lines indicate the 68.3% interval of objects colours closest to the mean colour in each bin. Each bin contains 200 data points. The new uncertainty is inferred from this interval.

3.4.2 Selection criteria

The following four criteria were applied to select our candidate LAEs from the eight initial source catalogues:

1. the narrowband image used as the detection image must have the most flux of all the narrowband images and the source must have a 4σ detection or better;

2. the narrowband image with the least flux needs to be a non-detection, i.e. less than 2σ;

3. there must be at least a 2σ detection in the intermediate band image;

4. none of the broadband images, i.e. neither B nor R, must have a detection above 2σ.

Table 3.2 contains the values of the 2σ detection thresholds of the images used for the 6 pixel aperture. In total 33 candidates were selected using the above criteria. Visual inspection showed that 26 sources arose from artefacts of which the vast

majority were out-of-focus ghost rings from bright stars. The final sample contains seven candidate LAEs.

We note here the importance of the usage of the intermediate band filter. If we were to reapply all the criteria except for criterion 3, i.e. we do not use the intermediate band images, we would obtain 284 candidates instead of the 33 for visual inspection.

The *AB*-magnitudes, derived line fluxes and luminosities for the candidates are shown in Table 3.4. To convert between *AB*-magnitudes and line flux in $\mathrm{erg\,s^{-1}\,cm^{-2}}$ we use the following relation:

$$F_{\mathrm{line}} = 3 \times 10^{18}\, 10^{-0.4(m_{AB}+48.590)}\, \frac{\Delta\lambda}{\lambda_c^2} \tag{3.1}$$

where $\Delta\lambda$ and λ_c are the *FWHM* and the central wavelength of the narrowband filter in Å, respectively, and m_{AB} the *AB*-magnitude of the object. In Fig. 3.3 the thumbnails of the seven candidate LAEs at $z \sim 5.7$ are shown. We defer a more detailed discussion about the sample properties to Sect. 3.5.

3.4.3 Completeness corrections

From the Hubble Deep Field (HDF) galaxy number-count data for the *F*814*W* filter (Williams et al. 1996) we computed completeness corrections for our eight source catalogues. The HDF counts are determined over the magnitude range $I_{814} = 22 - 29$, and agree well with our galaxy counts over all narrowband filters in the range $N = 22 - 24$. Figure 3.4 shows the counts for the *F*814*W* filter in the HDF and for the N_{817} filter in the S11 field. Figure 3.4 also shows the linear fit used as the basis for the calculation of the detection completeness. The fit is done to the combined number count data over two intervals: $N_{817} = [20, 22.5]$, where the WFILAS counts are complete, and $I_{814} = [22.5, 25]$, where the HDF counts are linear.

Detection completeness is defined as the ratio of WFILAS sources to the number expected from the number-count relation. Figure 3.5 shows the derived detection completeness for each filter-field combination used for WFILAS. The differences are mainly due to unequal exposure times, although filter throughput and image quality also play a role. These could explain the overall lower sensitivity of the N_{824} filter, as can be inferred from Fig. 3.5. Additionally, we correct for detection completeness arising due to the intermediate band selection criterion. We constructed a noise image by stacking the intermediate band images without registering. The completeness is defined as the rate of recovery of artificially inserted objects.

Given the different sensitivities of each filter-field combination, we define a homogeneous subsample of our initial candidate sample, using the candidates from our four most sensitive field-filter combinations. We call this our "complete" sample (4 of the 7 LAEs; marked in Table 3.4), because once defined, we use the

Table 3.4. The candidate list of the WFILAS survey after the selection as described in Sect. 3.4.

SExtractor ID	Object ID	B	R	M_{815}	N_{810}	N_{817}	N_{824}	Line flux ($10^{-17}\,\mathrm{erg\,s^{-1}\,cm^{-2}}$)	Luminosity ($10^{43}\,\mathrm{erg\,s^{-1}}$)
CDFS_1864[a]	J033215.14-280013.9	>26.25	>26.56	24.72 ± 0.46	23.14 ± 0.26	>24.27	>23.93	6.5 ± 1.5	2.3 ± 0.5
CDFS_4928[a]	J033145.97-275316.4	>26.25	>26.56	24.59 ± 0.41	23.38 ± 0.32	24.11 ± 0.47	23.61 ± 0.41	5.2 ± 1.6	1.8 ± 0.5
CDFS_5388[a]	J033202.37-275211.3	>26.25	>26.56	24.70 ± 0.45	23.32 ± 0.31	>24.27	>23.93	5.5 ± 1.5	1.9 ± 0.5
S11_5236[a b]	J114334.98-014433.7	>26.63	>26.59	24.31 ± 0.42	>24.13	23.05 ± 0.18	>23.74	7.0 ± 1.2	2.5 ± 0.4
S11_8921[c]	J114218.90-013544.6	>26.63	26.38 ± 0.45	23.88 ± 0.28	23.98 ± 0.47	23.41 ± 0.26	>23.75	5.0 ± 1.2	1.8 ± 0.4
S11_10595	J114312.46-013049.6	>26.63	>26.60	24.44 ± 0.47	>24.13	23.52 ± 0.28	>23.75	4.5 ± 1.2	1.6 ± 0.4
SGP_8884[d]	J004525.38-292402.8	>26.07	>26.41	23.33 ± 0.20	22.73 ± 0.16		>24.06	9.5 ± 1.4	3.3 ± 0.5

From left to right are the object name, the B, R, M_{815}, N_{810}, N_{817} and N_{824} AB-magnitudes, line flux calculated from the narrowband magnitude in which the object was detected and line luminosity. For all measurements less than 2σ the 2σ upper limit has been given.

[a]Galaxy is in the complete sample

[b]Confirmed LAE at $z = 5.721$. See text and Chap. 2 for details.

[c]Signal-to-noise in the range $2 - 3\sigma$ for R band in the 10 pixel aperture, but $< 2\sigma$ in the 6 pixel aperture

[d]Confirmed LAE at $z = 5.652$. See text for details.

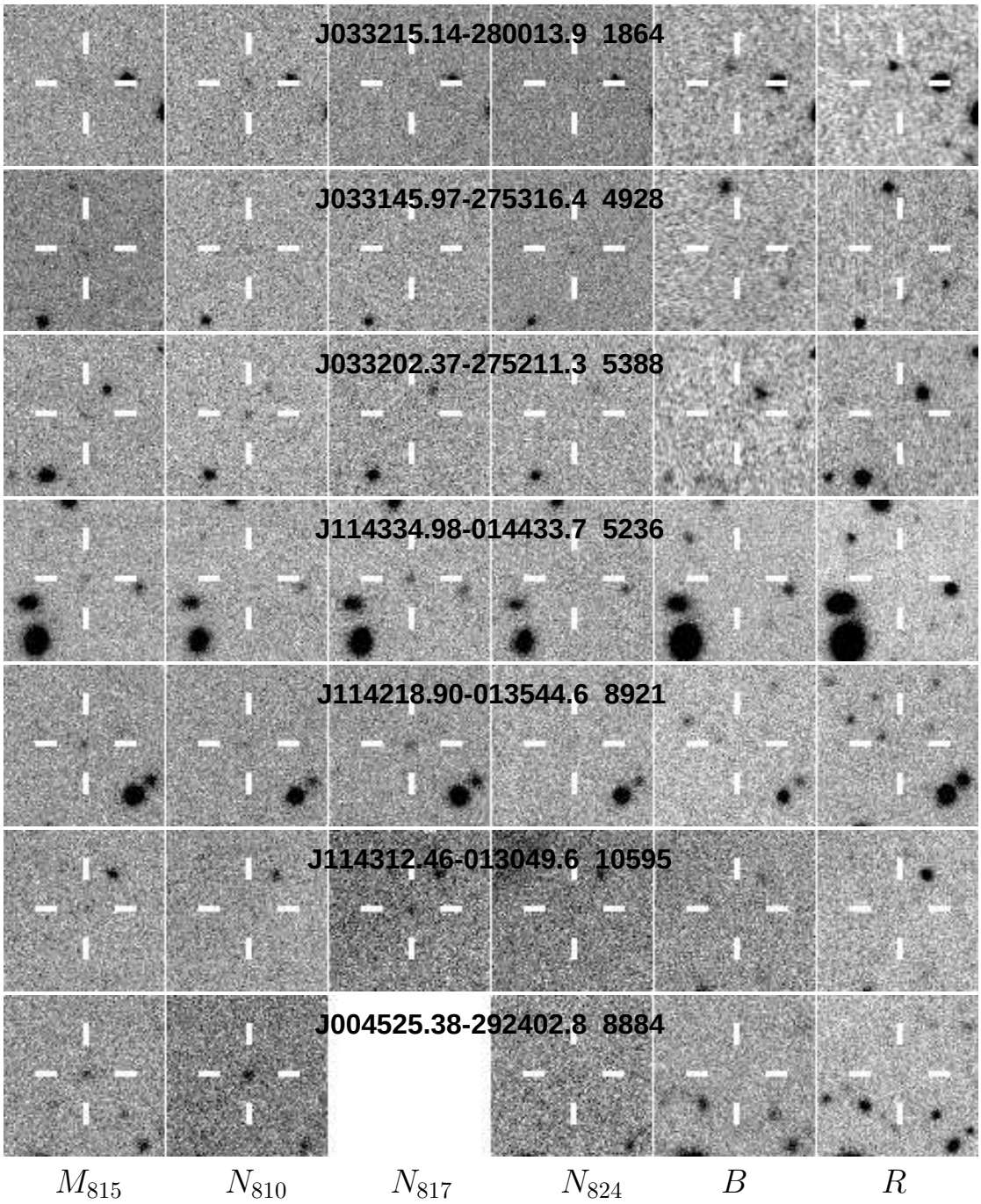

Fig. 3.3: Thumbnails of each region in which the candidate LAEs appears. The thumbnails cover a $19'' \times 19''$ region with a pixel scale of $0\overset{''}{.}238\,\mathrm{pixel}^{-1}$ and North is up and East to the left. From left to right are the filters M_{815}, N_{810}, N_{817}, N_{824}, B and R.

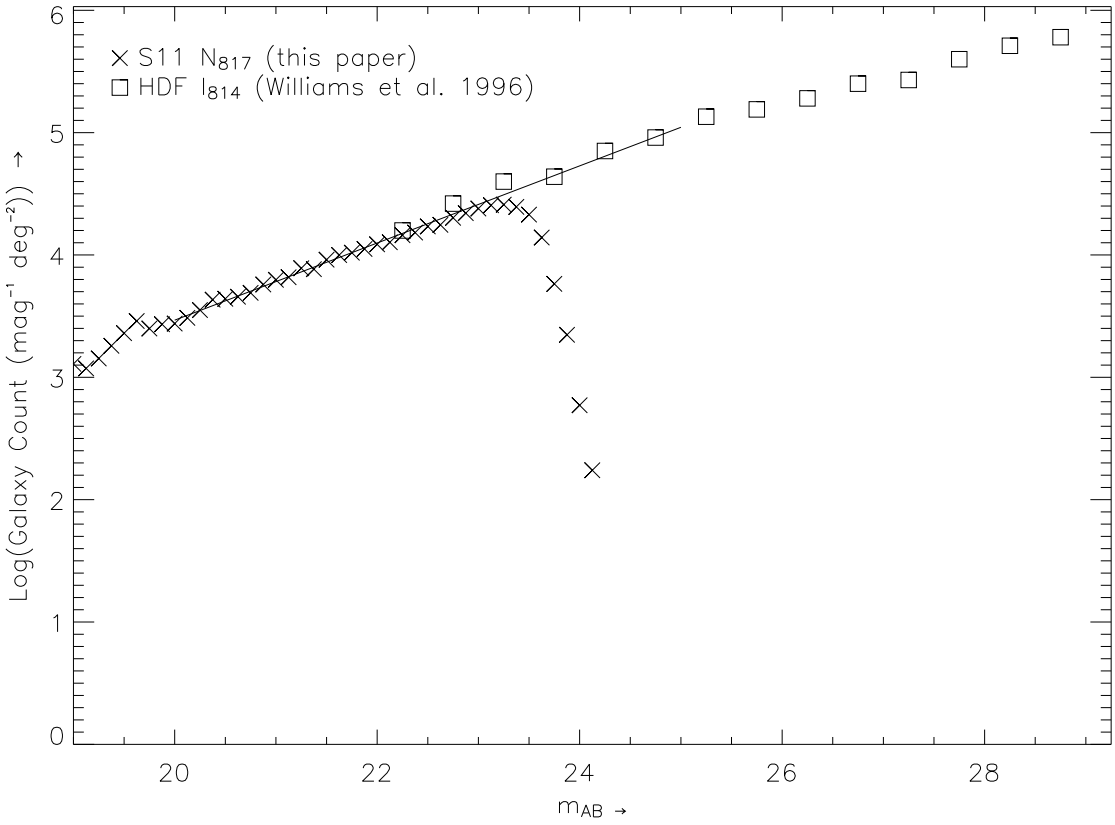

Fig. 3.4: Galaxy counts as a function of *AB*-magnitude for the N_{817} filter in the S11 field. Plotted are the N_{817} source counts of the S11 field (*crosses*) together with the I_{814} galaxy counts of the Hubble Deep Field (*squares*). The solid line indicates the fitted linear relation between the magnitude and galaxy count.

curves in Fig. 3.5 to correct the detected candidate numbers for incompleteness, in contrast to our initial "incomplete" sample (all 7 LAEs). The purpose of the subsample is that it lies within a uniform flux limit. Figure 3.5 shows that our four best filter-field combinations consist of the N_{810} and N_{817} filters in both the CDFS and S11 fields. These four field-filter combinations reach at least 50% completeness at $M_{\rm AB} = 23.38$, or $5.1{\times}10^{-17}\,{\rm erg\,s^{-1}\,cm^{-2}}$. We take this as the flux limit of our complete sample. As such, the number density derived from the complete sample is a more accurate measure of the density of sources down to the nominated flux limit than the number density of the incomplete sample. Figure 3.6 shows the luminosity distribution of the complete sample alongside our initial candidate list, which we call the "incomplete" sample. It shows that in using completeness corrections our detected source density is up by 50%.

3.5 $z \sim 5.7$ Candidate LAE Catalogue

In the previous Sect. we introduced two sets of candidate LAEs: the full (but incomplete) sample of seven candidate LAEs and a subsample thereof, complete to

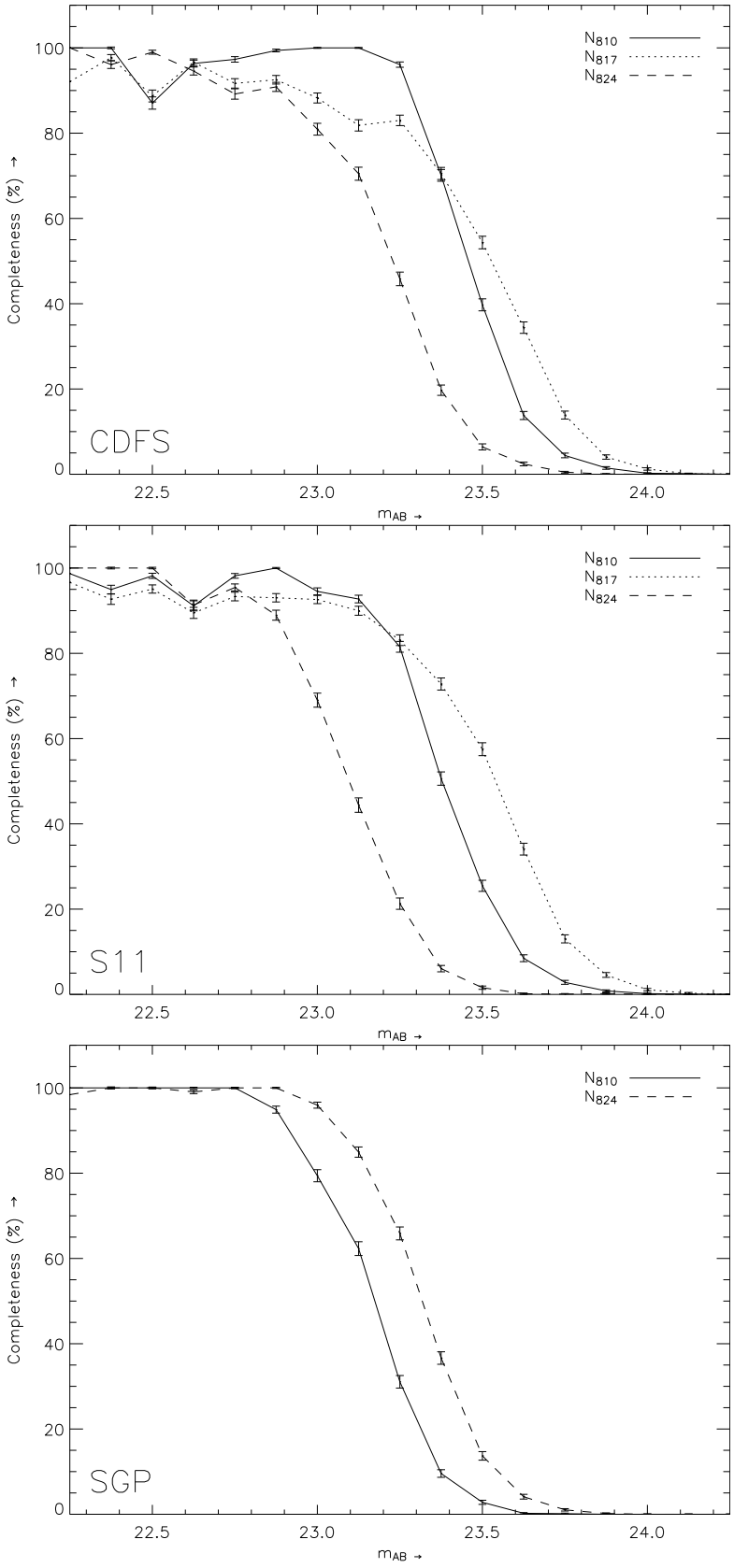

Fig. 3.5: Detection of completeness as function of magnitude derived from the galaxy density-magnitude relation as described in Sect. 3.4. From top to bottom the CDFS, S11 and SGP fields are shown. No N_{817} data are available for the SGP field.

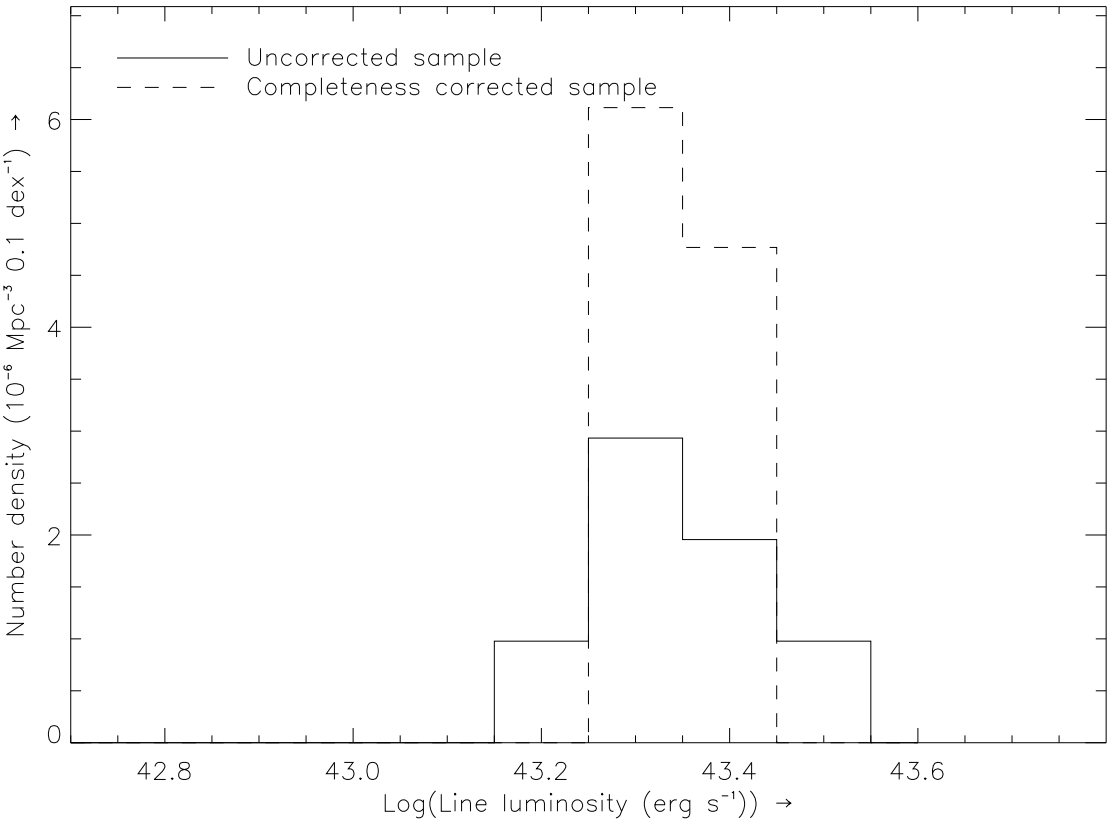

Fig. 3.6: Line luminosity distribution of the candidate LAEs. Two samples are indicated: all the candidates, but not corrected for completeness (*solid*) and the candidates in the complete sample, i.e. candidates of the four deepest narrowband images with a magnitude cut-off at 50% completeness of the worst of these four images (*dashed*).

$F_{lim} = 5.1 \times 10^{-17}\,\mathrm{erg\,s^{-1}\,cm^{-2}}$ (the complete sample). The flux limit of the incomplete sample is almost twice the limit of the complete sample ($3.4 \times 10^{-17}\,\mathrm{erg\,s^{-1}\,cm^{-2}}$).

To examine the luminosity distribution of our sample we use the Schechter function (Schechter 1976), as it is a good representation of the data at bright luminosities. From this, the luminosity density $\mathcal{L}$ of a distribution with a limiting luminosity L_{lim} is given by

$$\mathcal{L}(L \geq L_{lim}) = \phi^* L^* \Gamma(\alpha + 2, L_{lim}/L^*), \tag{3.2}$$

where α and ϕ^* represent the slope of the faint end of the Schechter function and the normalisation constant of the galaxy density, respectively. Γ is the incomplete gamma-function. Currently, the luminosity function for LAEs at $z \sim 5.7$ is poorly defined and authors commonly adopt either one or two of the three parameters from low redshift surveys to calculate the third.

We examine the influence of non-detections of bright ($L \gtrsim L^*$) LAEs for the total Lyα luminosity density by employing the same method as Ajiki et al. (2003),

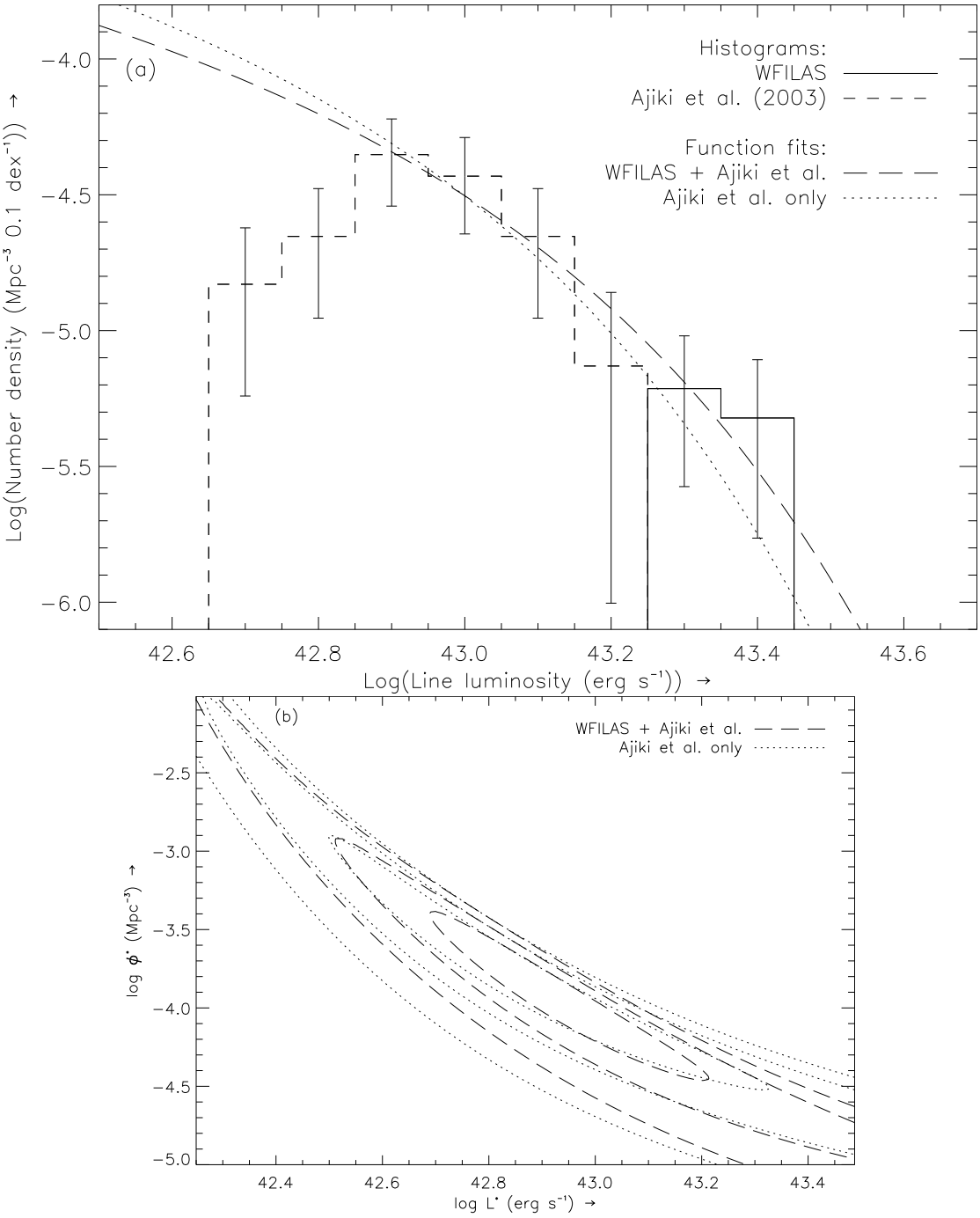

Fig. 3.7: a) Line luminosity distribution of the complete sample of candidate LAEs (*solid histograms*) together with the candidates from Ajiki et al. (2003) (*dashed histograms*). Both samples are corrected for completeness. The errorbars are derived using Poisson statistics. Furthermore, two Schechter function fits are indicated: one to the combined WFILAS and Ajiki sample (*dotted*) and one to Ajiki sample only (*long dashed*). **b)** The 68.3%, 95.4% and 99.7% confidence limits for the fitting parameters L^* and ϕ^*. See text for details.

Table 3.5. Number density of LAEs per luminosity bin as indicated in Fig. 3.7a.

Log(L (erg s^{-1}))	Log(Φ (Mpc^{-3} 0.1 dex^{-1}))
42.7	$-4.83^{+0.21}_{-0.41}$
42.8	$-4.65^{+0.18}_{-0.30}$
42.9	$-4.35^{+0.13}_{-0.19}$
43.0	$-4.43^{+0.14}_{-0.21}$
43.1	$-4.65^{+0.18}_{-0.30}$
43.2	$-5.13^{+0.27}_{-0.87}$
43.3	$-5.21^{+0.19}_{-0.36}$
43.4	$-5.32^{+0.21}_{-0.44}$

another narrowband imaging survey aimed at finding LAEs at $z \sim 5.7$. In the interest of comparison, we follow Ajiki et al. exactly and adopt the Fujita et al. (2003) values for α (-1.53) and ϕ^* ($10^{-2.62}$ Mpc^{-3}). Their approach was to solve Eq. (3.2) for L^*, instead of fitting a Schechter function. Fixing ϕ^* and allowing L^* and α to vary imposes a strong prior on the final fit, it allows us to compare directly to the results of Ajiki et al. by preserving their method. The luminosity density $\mathcal{L}$ was calculated by summing the luminosity of all candidates (corrected for completeness) and divided by the corresponding survey volume. With the given survey limits the equation can be solved for L^*. Equation (3.2) yields the total luminosity density when $L_{lim} = 0$. We have done this for three cases: for the candidates of Ajiki et al. (case A), the complete sample of our candidates (case B) and a combined sample of these two surveys (case C). For our complete sample we derive a higher L^* (+0.12 dex; case B) than Ajiki et al. (2003, case A) which implies an increase of the luminosity density $\mathcal{L}$ of ∼30%. If we scale the luminosity contribution of the candidates from Ajiki et al. to our volume and combine the two samples, L^* is higher ($\log L^* = 42.66$; case C). Table 3.6 summarises the results. Detecting LAEs of such bright luminosity at this redshift demonstrates the necessity of wide field surveys, such as WFILAS, to provide a sample of LAEs at the bright end.

As a second approach, we tried fitting a Schechter function to the combined WFILAS and Ajiki et al. (2003) dataset, using a minimised χ^2 fit (Fig. 3.7). We did not use the two lowest luminosity bins of Ajiki et al. (2003) to constrain the fit because these force the function to decline at the faint end. Instead, we set the faint end slope to $\alpha = -1.53$, similar to the Hα luminosity function at $z \sim 0.24$ from Fujita et al. (2003), on which Ajiki et al. based their work. Figure 3.7b shows a strong correlation between L^* and ϕ^* due to the slow turn-over at the bright end.

From the fitting there are three results to conclude. Firstly, incorporating the four completeness-corrected WFILAS galaxies into the Ajiki et al. (2003) galaxies

Table 3.6. Calculation of the Schecter function parameter L^* and luminosity density $\mathcal{L}$ according to Ajiki et al. (2003) for their sample, our complete sample and the combination of the two.

	α	$\log \phi^{*\,a}$	$\log L^{*\,b}$	$\log {L_{lim}}^{c}$	$\log V^{d}$	$\log \mathcal{L}^{e}$	Comment
Case A	–	–	–	42.85	5.26	39.04	Sum of the candidates from Ajiki et al. (2003)
	-1.53	-2.62	42.61	42.85	5.26	39.04	Integrated luminosity function down to Ajiki et al. (2003) survey limit ($7.0\times10^{42}\,\mathrm{erg\,s^{-1}}$)
	-1.53	-2.62	42.61	–	–	40.27	Integration of the entire luminosity function
Case B	–	–	–	43.26	5.71	38.36	Sum of the candidates from completeness corrected WFILAS sample
	-1.53	-2.62	42.74	43.26	5.71	38.36	Integrated luminosity function down to the limit of the completeness corrected sample ($1.8\times10^{43}\,\mathrm{erg\,s^{-1}}$)
	-1.53	-2.62	42.74	–	–	40.39	Integration of the entire luminosity function
Case C	–	–	–	42.85	5.84	39.19	Sum of the combined WFILAS and Ajiki et al. (2003) samples low luminosity corrections
	-1.53	-2.62	42.66	42.85	5.84	39.19	Integrated luminosity function down to Ajiki et al. (2003) survey limit ($7.0\times10^{42}\,\mathrm{erg\,s^{-1}}$)
	-1.53	-2.62	42.66	–	–	40.32	Integration of the entire luminosity function

For each sample the luminosity density has been derived from the sum of the candidate luminosities divided by the corresponding survey volume. Then Eq. (3.2) was solved for L^*, with given α and ϕ^* from Ajiki et al. (2003). Finally, the entire luminosity function was integrated to give the final luminosity density.

[a] $\mathrm{Mpc^{-3}}$

[b] $\mathrm{erg\,s^{-1}}$

[c] $\mathrm{erg\,s^{-1}}$

[d] $\mathrm{Mpc^3}$

[e] $\mathrm{erg\,s^{-1}\,Mpc^{-3}}$

better constrains the bright end of the luminosity function. Furthermore, it seems that the current generation of surveys is only just reaching the volume coverage necessary to discover LAEs with $L > L^*$. The histogram in Fig. 3.7 shows a decreasing number of sources at the faint end. At face value, this could suggest that the ionising flux of the less luminous sources may be insufficient to escape the slowly expanding envelope of neutral hydrogen that surrounds the HII region in the LAE. Consequently, the sources are undetected and the faint end of the luminosity distribution decreases. However, it is difficult to detect faint LAEs and so the possibility of detection incompleteness cannot be ruled out.

Figure 3.8 shows the sky distribution of our candidates in each field. All candidates but one are in the CDFS and S11 fields. The only candidate in the SGP field is brighter than the candidates in the other fields (line flux $\sim 10^{-16}\,\mathrm{erg\,s^{-1}\,cm^{-2}}$). The reason for this is that the M_{815} filter for the SGP field has a shorter exposure time and lower signal-to-noise than the other fields.

In the CDFS field we note that our three candidates appear to be spatially clustered. Additionally, we note that the confirmed $z = 5.78$ i-drop galaxy of Bunker et al. (2003) is at the same redshift as the WFILAS candidates in this field, just like four candidate LAEs from a narrowband survey by Ajiki et al. (2005). We did not detect these four candidates since they are fainter than the detection limits of WFILAS in this field. Wang et al. (2005) have also done a narrowband survey of the CDFS field. They also find evidence for an overdensity of $z \sim 5.7$ sources in this field. Similarly, Malhotra et al. (2005) find an overdensity at redshift 5.9 ± 0.2 in the HUDF.

3.6 Confirmed LAEs[4]

In Westra et al. (2005) we reported the spectroscopic follow-up of one of the candidates, J114334.98−014433.7 (S11_13368 in that paper, hereafter S11_5236[5]). It was confirmed to be a LAE at $z = 5.721$. Here we present the spectral confirmation of a new candidate, J004525.38−292402.8 (hereafter SGP_8884), at $z = 5.652$. We also show its pre-imaging and compare its Lyα profile to S11_5236. SGP_8884 and S11_5236 are the only two out of the seven candidates presented in this paper for which we have obtained spectra.

3.6.1 Spectral data reduction

A pre-image with an intermediate band filter ($FWHM = 13\,\mathrm{nm}$) centred at 815 nm was taken with VLT/FORS2 on 2005 August 9. The $0\farcs252\,\mathrm{pix^{-1}}$ plate scale undersamples the $\lesssim 0.5''$stellar point spread function of the frames which were taken

[4] Based on observations made with ESO Telescopes at the Paranal Observatories under programmes ID 076.A-0553 and 272.A-5029.

[5] The object names are derived from *SExtractor* IDs. Refinements to our detection procedures since Chap. 2 caused a change in the ID and, therefore, in the object name

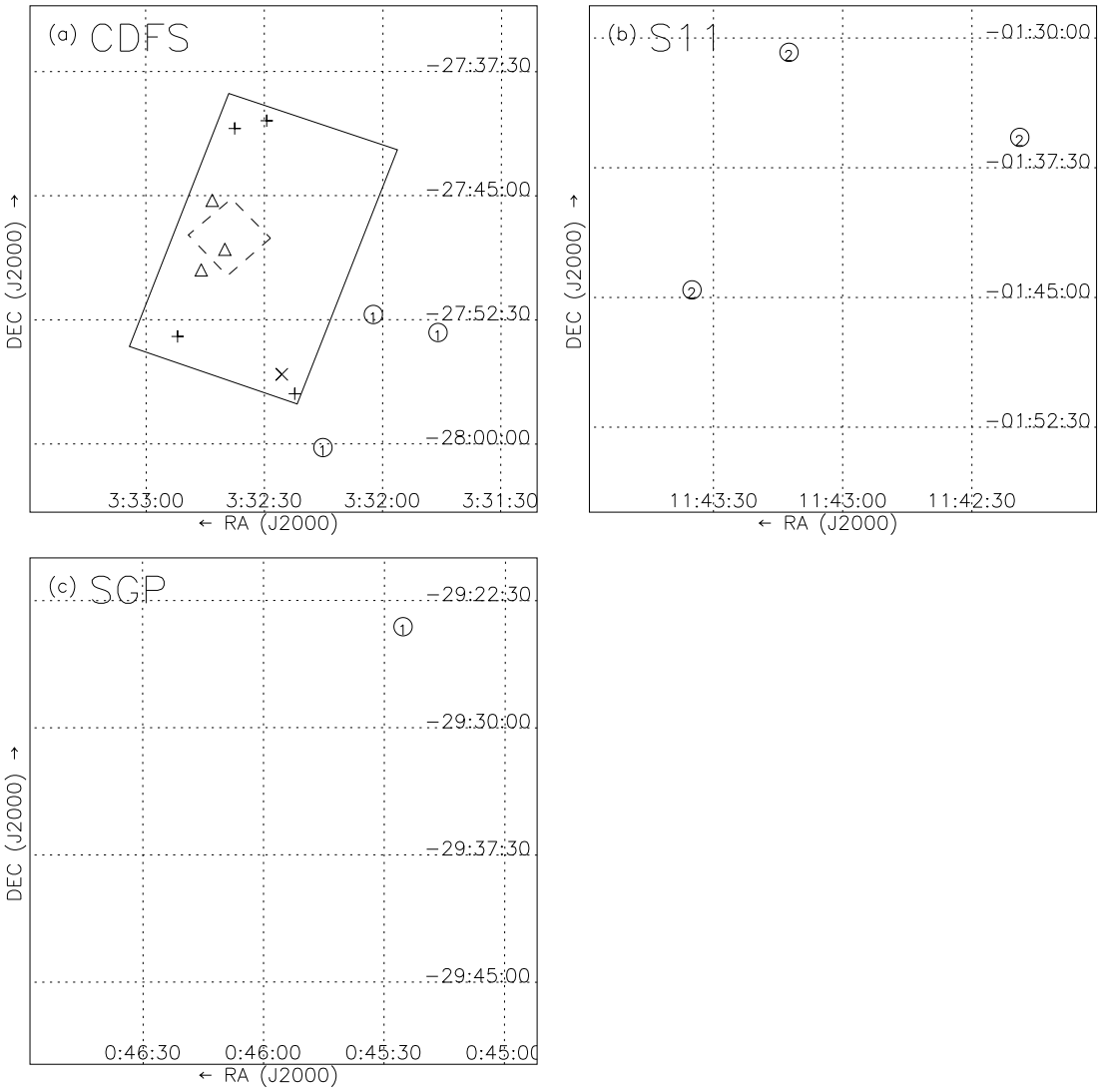

Fig. 3.8: Sky distribution of candidate line emitters per field with North up and East to the left for the **a)** CDFS, **b)** S11 and **c)** SGP fields. The "1", "2" and "3" labels correspond to the N_{810}, N_{817} and N_{824} filters, respectively. The gridlines are separated by 7.5. In the CDFS field the Hubble Ultra Deep Field (*dashed*) and GOODS-S (*solid*) have been indicated. The confirmed i-drop galaxy at $z = 5.78$ of Bunker et al. (2003, *cross)*, LAEs of Ajiki et al. (2005, *plus)* and Stanway et al. (2004, *triangle)* are also indicated. In the CDFS field there seems to be a overdensity of candidates towards the southern part of the field, similar to Wang et al. (2005).

during excellent seeing. SGP_8884 is unresolved, implying that the *FWHM* of the emitting region is $\leq$2.2 kpc. A $38'' \times 38''$ region around the object is shown in Fig. 3.9.

The spectroscopy consists of four exposures of 900 s, taken on 2005 October 3 with FORS2 using the 1028z grism and a $1''$ slit. The frames were overscan subtracted and flatfielded. They were combined by summing individual frames, thereby removing cosmic rays in the process.

The spectrum was flux calibrated using a standard star (HD 49798) taken with a $5''$ slit and corrected for slit-loss. This was calculated assuming a Gaussian source profile with a *FWHM* of $0\farcs72$ as measured from the spatial direction of the spectrum. The flux lost due to the $1''$ slit was calculated and added to the spectrum of the object.

3.6.2 Line fitting

Figure 3.10 shows the reduced spectrum of SGP_8884 alongside its best model fit. The spectrum has an asymmetric line profile, similar to our previously confirmed candidate LAE (Westra et al. 2005). It unlikely originates from a redshifted [OII] line at $z \sim 1.2$ because the resolution of our spectrum is high enough to resolve the [OII] $\lambda\lambda$3726,3728. Figure 3.11 shows the spectrum of one such [OII] emitter at $z = 1.18$ which was included in the same observations as SGP_8884. Furthermore, we do not find any other spectral features in our spectrum, such as Hβ or [N II], which could classify the emission coming from a lower redshift galaxy. Hence, we identify the line as Lyα at $z = 5.652$. With a total spectral line flux of $(1.0 \pm 0.1) \times 10^{-16}\,\mathrm{erg\,s^{-1}\,cm^{-2}}$ (slit-loss corrected), SGP_8884 is the brightest LAE at redshift $\sim$5.7 to date. The line flux derived from the spectrum is consistent with the flux derived from narrowband photometry $(9.5 \pm 1.4) \times 10^{-17}\,\mathrm{erg\,s^{-1}\,cm^{-2}}$, which is given in Table 3.4. The spectral line flux corresponds to a line luminosity of $L_{\mathrm{line}} = 3.5 \times 10^{43}\,\mathrm{erg\,s^{-1}}$ and a star formation rate of $32\,M_{\odot}\,\mathrm{yr^{-1}}$, using the star formation conversion rate of Ajiki et al. (2003). If we adopt $\sim$16 pixels ($= 32\,\mathrm{kpc^2}$) as an upper limit to the size of the emitting region, we derive a star formation rate surface density of $\Sigma_* \gtrsim 1\,M_{\odot}\,\mathrm{yr^{-1}\,kpc^{-2}}$.

Following earlier works (e.g. Dawson et al. 2002; Hu et al. 2004; Westra et al. 2005) we fitted a single component model to the Lyα line SGP_8884. The model consists of a truncated Gaussian with complete absorption blueward of the Lyα line centre. We find an excess of flux in the observed data compared to the model around 8110 Å. This suggests the presence of a second line component redward of the main peak. To test this, we measured the mean continuum levels, both red- and blueward of the line, as well as across the red-flanking region of the line. The continuum is calculated as the weighted mean of the flux density over this region. This yields for continuum in the red-flanking region a flux density of $(3.2 \pm 0.8) \times 10^{-19}\,\mathrm{erg\,s^{-1}\,cm^{-2}\,\AA^{-1}}$. Red- and blueward of the Lyα line the contin-

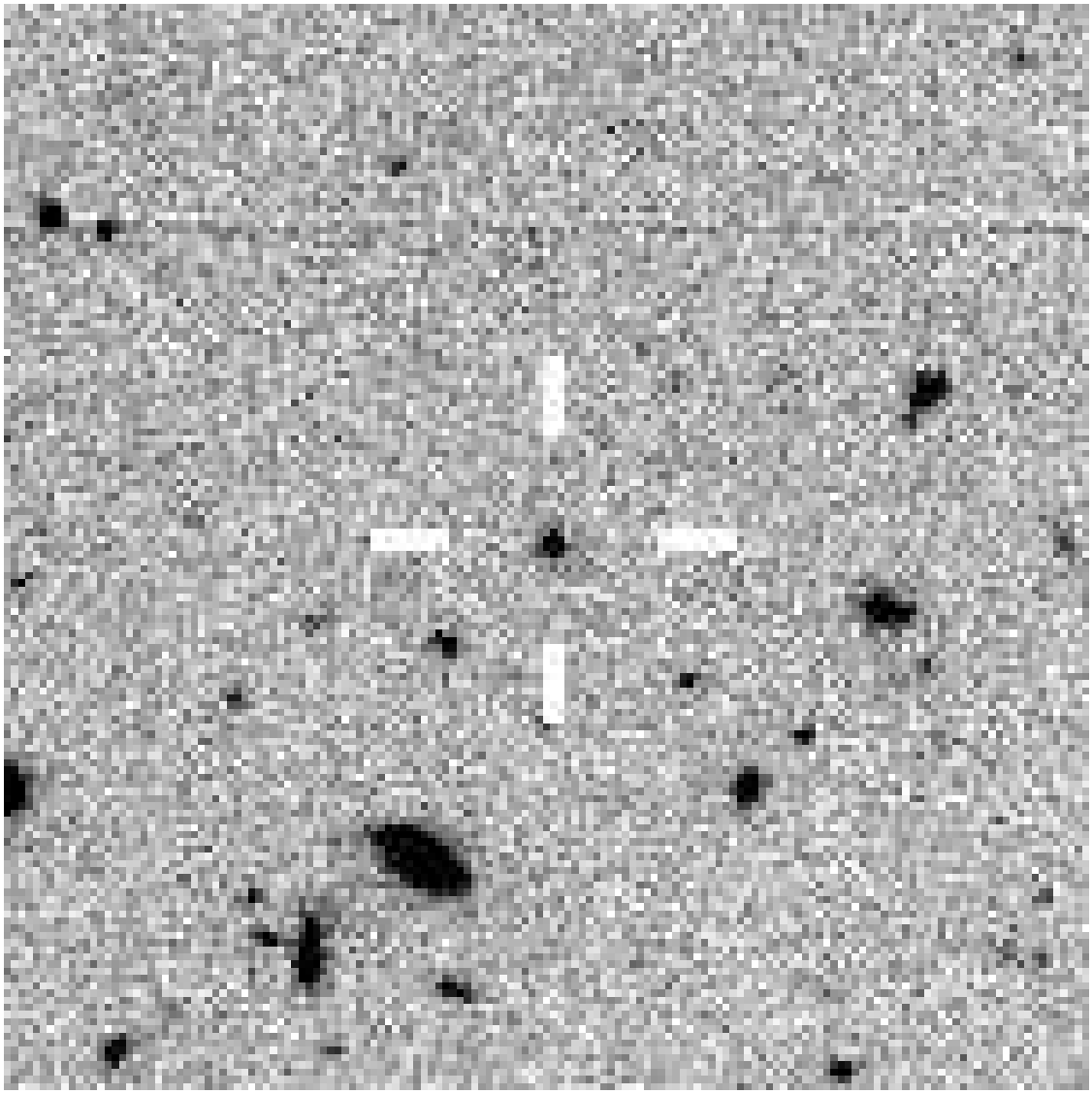

Fig. 3.9: A $38'' \times 38''$ region around the confirmed LAE in the SGP field. The image is created from the pre-image taken with VLT/FORS2. The image has a pixel scale of $0\overset{''}{.}252\,\mathrm{pix}^{-1}$. North is up and East is to the left.

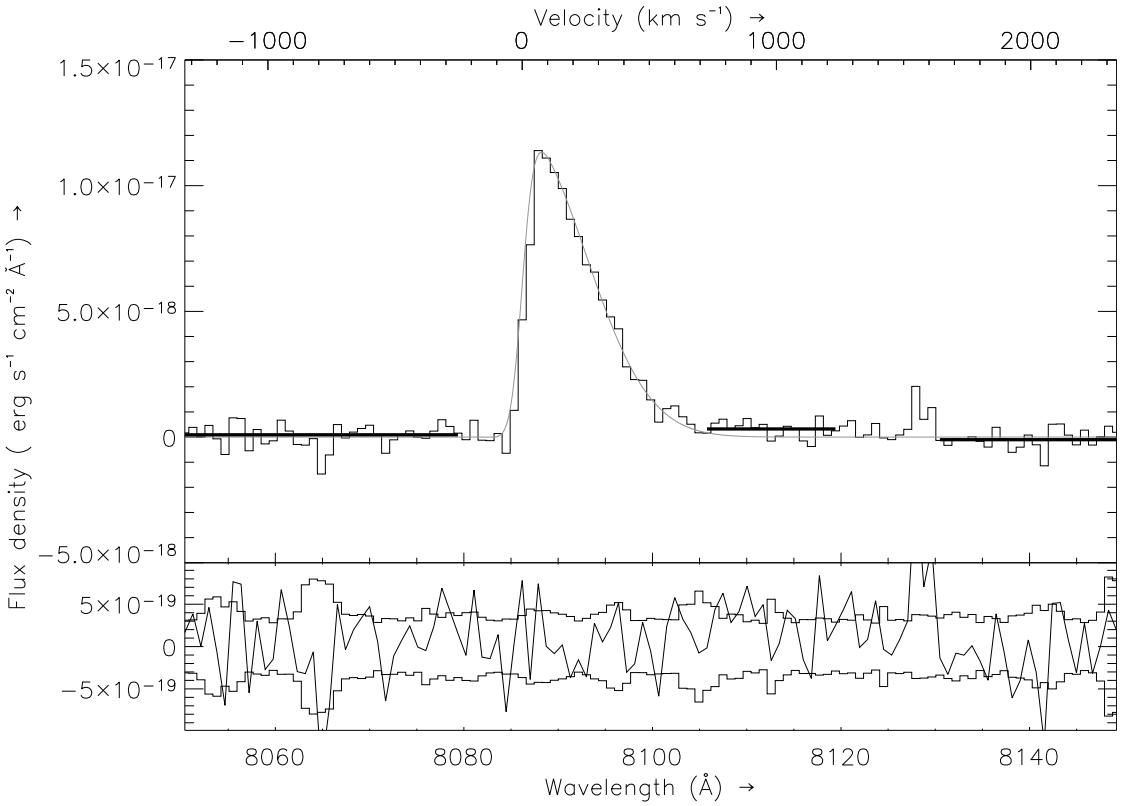

Fig. 3.10: (*Top*) Flux calibrated spectrum of the confirmed candidate LAE SGP_8884, the brightest candidate in our sample. The histogram shows the observed spectrum. Indicated in grey is the best-fitting single component model after convolution with the instrumental profile. The heavy bold lines indicate three regions for which we have calculated a mean continuum. (*Bottom*) Residuals from the observed data minus model fit. The histograms indicate the 1σ-error spectrum from the observed data, which includes both sky- and Poisson noise. The feature at 8125 Å is due to a remnant cosmic ray from one of the spectral frames.

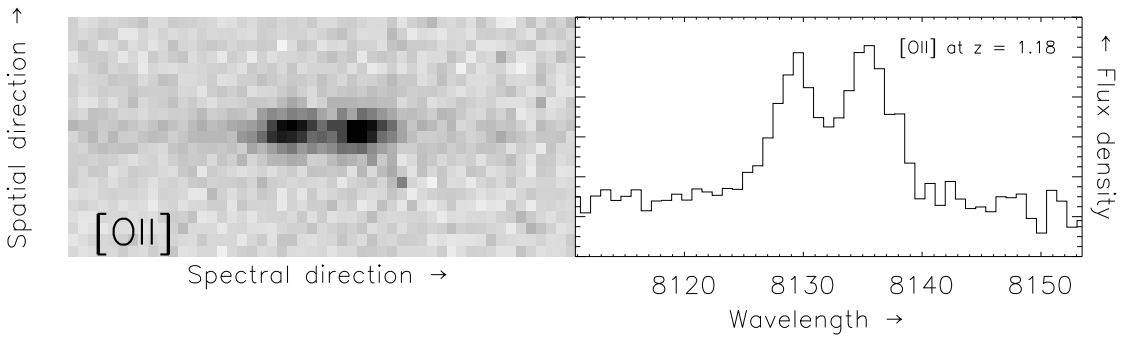

Fig. 3.11: (*Left*) Two dimensional spectrum of an [OII] emitting galaxy at $z = 1.18$ in the SGP field. (*Right*) The extracted one dimensional spectrum. We are able to easily resolve the [OII] $\lambda\lambda$3726,3728 lines with the available resolution. Both spectra are background subtracted.

uum is (-1.0 ± 0.8) × 10^{-19} erg s^{-1} cm^{-2} Å^{-1} and (0.9 ± 0.6) × 10^{-19} erg s^{-1} cm^{-2} Å^{-1}, respectively. These continuum levels are indicated by the heavy bold lines in Fig. 3.10. The lower limit for the rest frame equivalent width derived from the continuum of the red flank is 46 Å. The rest frame equivalent width derived from the 2σ upper limit of the continuum redward of the line is 125 Å.

To see if the excess of flux in the red flank of the Lyα line can be explained by an outflow, we fit a second Gaussian component to the spectrum of SGP_8884, as we did to the spectrum of S11_5236 in Westra et al. (2005). This yields an extremely faint and broad second component ($f_{\rm peak} \sim 5 \times 10^{-19}$ erg s^{-1} cm^{-2} Å^{-1} and $FWHM \sim 1700$ km s^{-1}). The precise parameters for the red component are difficult to constrain given its faint and broad profile. The parameters from the single component model for SGP_8884 and the single and double component models for S11_5236 are given in Table 3.7.

3.6.3 Discussion/Comparison

The Lyα emission we see is due to intense star formation rates synonymous with local starburst galaxies. Star formation rates per unit area in excess of 0.1 $M_\odot$ yr^{-1} kpc^2 are prone to produce large scale outflows of neutral hydrogen from a galaxy, powered by the supernovae and stellar winds of massive stars (Heckman 2002). The most efficient way for Lyα to escape from the compact star forming regions is due to scattering of the photons by the entrained neutral hydrogen (Chen & Neufeld 1994). The kinematics and orientation of the outflowing neutral hydrogen can alter the Lyα profile by absorbing photons bluer if along the line of sight, or backscattering redder than Lyα if behind and receding (e.g. Dawson et al. 2002). Lyα emission can also arise when large scale shocks from starburst winds impinge on clumps ($\sim$100 pc) of condensed gas accreting onto the halo (Bland-Hawthorn & Nulsen 2004).

Most examples of asymmetric Lyα emission at $z \sim 6$ show an extended tail implying backscattering over a fairly wide range of velocities beyond the central Lyα emission (e.g. Fig. 9 of Hu et al. 2004). The limiting physical size of SGP_8884 ($FWHM < 2.2$ kpc) is consistent with the scale of emitting regions in the local starburst galaxy M82 which span 0.5 to 1 kpc (Courvoisier et al. 1990; Blecha et al. 1990). This, and the scale of its outflow, make it fairly typical of both the starbursting sources seen at $z \sim 6$ and their local counterparts.

The tentative discovery of a second component in S11_5236 (Chap. 2 could be explained by either an expanding shell of neutral hydrogen (Dawson et al. 2002; Ahn et al. 2003), or by infall of the IGM onto the LAE (Dijkstra et al. 2005). The flux of the intrinsic Lyα line depends heavily on the model. It is suggested that the total intrinsic Lyα flux emerging from these sources is underestimated by an order of magnitude (e.g. Dijkstra et al.). Therefore, the star formation rates derived from the observed Lyα lines could be heavily underestimated.

Table 3.7. Parameters for the single component model to SGP_8884 before convolution with the instrumental profile.

Component [1]	λ_c [2]	$f_{\rm peak}$ [3]	$FWHM$ [4]	$FWHM$ [5]	Δv [6]	Δv [7]
SGP_8884 single component						
Single peak	8086.2	1.2×10^{-17}	15.7	580		
S11_5236 single component						
Single peak	8172.2	8.3×10^{-18}	13.5	495		
S11_5236 double component, "broad"						
Main peak	8173.1	8.0×10^{-18}	11.3	413		
Red peak	8184.1	1.9×10^{-18}	2.3	85	+11.1	+406
S11_5236 double component, "narrow"						
Main peak	8173.1	8.1×10^{-18}	11.2	413		
Red peak	8184.1	4.8×10^{-18}	0.5	18	+11.0	+403

We also include the parameters for the single component and the two double component models of the previously confirmed LAE S11_5236 (Chap. 2). These parameters differ slightly from Chap. 2, since we have subsequently corrected the spectrum of S11_5236 for slit-losses.

[1]Component of the fit

[2]Central wavelength of the fitted component in Å

[3]Peak flux density in 10^{-18} erg s^{-1} cm^{-2} Å^{-1}

[4,5]$FWHM$ of full Gaussian of the profile in Å and km s^{-1}, respectively

[6,7]Velocity shift of the second component in Å and km s^{-1}.

Figure 3.12 shows a comparison between the line profiles of the two LAEs discovered with WFILAS. S11_5236 differs from SGP_8884 in that a clear peak, $\sim 20 - 90$ km s^{-1} wide, is seen $\sim$400 km s^{-1} redward of Lyα (Westra et al. 2005). The red component is narrower ($\sim$15%) and relatively stronger than SGP_8884. The difference in the width of the red component is even more pronounced ($\sim$30%) when we compare the main peak of the two-component fits to the spectrum of S11_5236 to the single peak of the one-component fits to the spectrum of SGP_8884. This can clearly be seen in panels a and e of Fig. 3.12.

Ultimately, such outflows are thought to be responsible for the chemical enrichment of the IGM by $z \sim 6$ (Aguirre et al. 2001). Outflows are a process facilitating the escape of UV photons, which are the origin for the UV background (Madau et al. 1999).

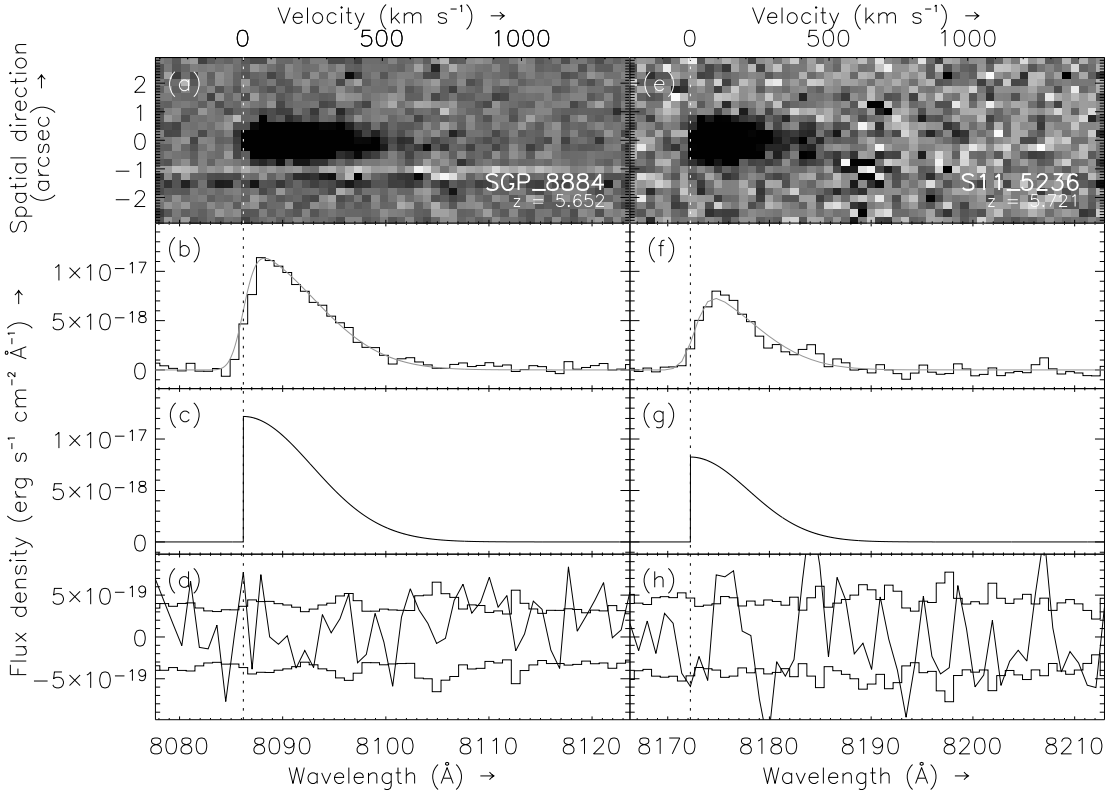

Fig. 3.12: Comparison of the Lyα line profiles of the two WFILAS sources, SGP_8884 and S11_5236. **a)** Two dimensional background-subtracted spectrum of SGP_8884. **b)** Observed Lyα line (*histograms*) with the best-fitting one component model (*grey solid line*). **c)** Same model line profile as in **b)** but before convolution with the instrument profile. **d)** Observed data minus model fit (as plotted in **b)**). Also shown (*histograms*) is the 1σ-error spectrum from the observed data, which includes both sky- and Poisson noise. Panels **e)** through **h)** show the same for S11_5236. The horizontal axes show both the wavelength (in Å; *bottom*) and velocity offset from the centre of the full Gaussian of the Lyα line (in $\mathrm{km\,s^{-1}}$; *top*)

3.7 Summary

In this paper we have presented the Wide Field Imager Lyman-Alpha Search (WFILAS), which uses a combination of narrow-, intermediate and broadband filters on the ESO/MPI 2.2 m telescope to search for LAEs at redshift $z \sim 5.7$. This search has resulted in seven bright ($L \geq 1.1 \times 10^{43}\,\mathrm{erg\,s^{-1}}$) candidate galaxies across three fields spanning almost 0.8 sq. degree.

Most of our candidates are in the regimes of bright luminosities, beyond the reach of less voluminous surveys. Adding our candidates to those of earlier such surveys results in an integrated luminosity density $\mathcal{L} \sim 30\%$ higher than found by such surveys alone. We also find potential clustering in our CDFS field, supporting overdensities discovered by other surveys. Spectroscopic follow-up for confirmation in this area will be crucial.

Two candidates have been confirmed to be LAEs at $z \sim 5.7$ by means of spectroscopy. One of these galaxies is the brightest LAEs at this redshift. The broad, asymmetric profiles of the Lyα line of both objects are consistent with neutral hydrogen backscattering of a central starbursting source.

Acknowledgements

The authors wish to thank the Max-Planck-Institut für Astronomie and the DDT grant of the European Southern Observatory for providing the narrow band filters which are crucial to the WFILAS survey. The broadband and part of the intermediate band data were kindly provided by the COMBO-17 team (Wolf et al. 2004). We also like to thank the anonymous referee for his/her useful suggestions and comments. E.W. wishes to thank A. Frebel for her useful comments and discussions regarding this paper and the Astronomical Society of Australia Travel Grant. D.H.J. is supported as a Research Associate by the Australian Research Council Discovery-Projects Grant (DP-0208876), administered by the Australian National University. C.W. is supported by a PPARC Advanced Fellowship.

References

Adelberger, K. L., Steidel, C. C., Shapley, A. E., & Pettini, M., 2003, ApJ, 584, 45

Aguirre, A., Hernquist, L., Schaye, J., Weinberg, D. H., Katz, N., & Gardner, J., 2001, ApJ, 560, 599

Ahn, S., Lee, H., & Lee, H. M., 2003, MNRAS, 340, 863

Ajiki, M., Mobasher, B., Taniguchi, Y., Shioya, Y., Nagao, T., Murayama, T., & Sasaki, S. S., 2005, arXiv:astro-ph/0510672

Ajiki, M., Taniguchi, Y., Fujita, S. S., Shioya, Y., Nagao, T., Murayama, T., Yamada, S., Umeda, K., et al., 2003, AJ, 126, 2091

Allen, P. D., Moustakas, L. A., Dalton, G., MacDonald, E., Blake, C., Clewley, L., Heymans, C., & Wegner, G. 2005, MNRAS, 360, 1244

Baade, D., Meisenheimer, K., Iwert, O., Alonso, J., Augusteijn, T., Beletic, J., Bellemann, H., Benesch, W., et al., 1999, The Messenger, 95, 15

Barger, A. J., Cowie, L. L., Capak, P., Alexander, D. M., Bauer, F. E., Brandt, W. N., Garmire, G. P., & Hornschemeier, A. E. 2003, ApJ, 584, L61

Becker, R. H., Fan, X., White, R. L., Strauss, M. A., Narayanan, V. K., Lupton, R. H., Gunn, J. E., Annis, J., et al., 2001, AJ, 122, 2850

Bertin, E. & Arnouts, S. 1996, A&AS, 117, 393

Bessell, M. S. 1999, PASP, 111, 1426

Bland-Hawthorn, J. & Nulsen, P. E. J. 2004, arXiv:astro-ph/0404241

Blecha, A., Golay, M., Huguenin, D., Reichen, D., & Bersier, D., 1990, A&A, 233, L9

Bouwens, R. J., Illingworth, G. D., Blakeslee, J. P., & Franx, M., 2005, arXiv:astro-ph/0509641

Bunker, A. J., Stanway, E. R., Ellis, R. S., & McMahon, R. G., 2004, MNRAS, 355, 374

Bunker, A. J., Stanway, E. R., Ellis, R. S., McMahon, R. G., & McCarthy, P. J., 2003, MNRAS, 342, L47

Chen, W. L. & Neufeld, D. A. 1994, ApJ, 432, 567

Courvoisier, T. J.-L., Reichen, M., Blecha, A., Golay, M., & Huguenin, D., 1990, A&A, 238, 63

Cuby, J.-G., Le Fèvre, O., McCracken, H., Cuillandre, J.-C., Magnier, E., & Meneux, B., 2003, A&A, 405, L19

Dawson, S., Rhoads, J. E., Malhotra, S., Stern, D., Dey, A., Spinrad, H., Jannuzi, B. T., Wang, J., et al., 2004, ApJ, 617, 707

Dawson, S., Spinrad, H., Stern, D., Dey, A., van Breugel, W., de Vries, W., & Reuland, M., 2002, ApJ, 570, 92

Dijkstra, M., Haiman, Z., & Spaans, M., 2005, arXiv:astro-ph/0510409

Djorgovski, S. G., Castro, S., Stern, D., & Mahabal, A. A., 2001, ApJ, 560, L5

Fan, X., Narayanan, V. K., Strauss, M. A., White, R. L., Becker, R. H., Pentericci, L., & Rix, H.-W., 2002, AJ, 123, 1247

Feldmeier, J. J., Mihos, J. C., Morrison, H. L., Rodney, S. A., & Harding, P., 2002, ApJ, 575, 779

Foucaud, S., McCracken, H. J., Le Fèvre, O., Arnouts, S., Brodwin, M., Lilly, S. J., Crampton, D., & Mellier, Y. 2003, A&A, 409, 835

Fujita, S. S., Ajiki, M., Shioya, Y., Nagao, T., Murayama, T., Taniguchi, Y., Umeda, K., Yamada, S., et al., 2003, ApJ, 586, L115

Giavalisco, M. & Dickinson, M. 2001, ApJ, 550, 177

Gnedin, N. Y. & Ostriker, J. P. 1997, ApJ, 486, 581

Haiman, Z. & Loeb, A. 1998, ApJ, 503, 505

Heckman, T. M. 2002, in ASP Conf. Ser. 254: Extragalactic Gas at Low Redshift, 292–+

Hildebrandt, H., Bomans, D. J., Erben, T., Schneider, P., Schirmer, M., Czoske, O., Dietrich, J. P., Schrabback, T., et al., 2005, A&A, 441, 905

Hippelein, H., Maier, C., Meisenheimer, K., Wolf, C., Fried, J. W., von Kuhlmann, B., Kümmel, M., Phleps, S., et al., 2003, A&A, 402, 65

Hu, E. M., Cowie, L. L., Capak, P., McMahon, R. G., Hayashino, T., & Komiyama, Y., 2004, AJ, 127, 563

Hu, E. M., Cowie, L. L., & McMahon, R. G., 1998, ApJ, 502, L99+

Kodaira, K., Taniguchi, Y., Kashikawa, N., Kaifu, N., Ando, H., Karoji, H., Ajiki, M., Akiyama, M., et al., 2003, PASJ, 55, L17

Labbé, I., Franx, M., Rudnick, G., Schreiber, N. M. F., Rix, H., Moorwood, A., van Dokkum, P. G., van der Werf, P., et al., 2003, AJ, 125, 1107

Madau, P., Haardt, F., & Rees, M. J., 1999, ApJ, 514, 648

Maier, C., Meisenheimer, K., Thommes, E., Hippelein, H., Röser, H. J., Fried, J., von Kuhlmann, B., Phleps, S., et al., 2003, A&A, 402, 79

Malhotra, S., Rhoads, J. E., Pirzkal, N., Haiman, Z., Xu, C., Daddi, E., Yan, H., Bergeron, L. E., et al., 2005, ApJ, 626, 666

Møller, P. & Fynbo, J. U. 2001, A&A, 372, L57

Oke, J. B. & Gunn, J. E. 1983, ApJ, 266, 713

Ouchi, M., Shimasaku, K., Akiyama, M., Sekiguchi, K., Furusawa, H., Okamura, S., Kashikawa, N., Iye, M., et al., 2005, ApJ, 620, L1

Ouchi, M., Shimasaku, K., Okamura, S., Furusawa, H., Kashikawa, N., Ota, K., Doi, M., Hamabe, M., et al., 2004, ApJ, 611, 685

Rhoads, J. E., Dey, A., Malhotra, S., Stern, D., Spinrad, H., Jannuzi, B. T., Dawson, S., Brown, M. J. I., et al., 2003, AJ, 125, 1006

Rhoads, J. E. & Malhotra, S. 2001, ApJ, 563, L5

Santos, M. R., Ellis, R. S., Kneib, J., Richard, J., & Kuijken, K., 2004, ApJ, 606, 683

Schechter, P. 1976, ApJ, 203, 297

Schlegel, D. J., Finkbeiner, D. P., & Davis, M., 1998, ApJ, 500, 525

Spergel, D. N., Bean, R., Dore', O., Nolta, M. R., Bennett, C. L., Hinshaw, G., Jarosik, N., Komatsu, E., et al., 2006, arXiv:astro-ph/0603449

Stanway, E. R., Glazebrook, K., Bunker, A. J., Abraham, R. G., Hook, I., Rhoads, J., McCarthy, P. J., Boyle, B., et al., 2004, ApJ, 604, L13

Steidel, C. C., Adelberger, K. L., Giavalisco, M., Dickinson, M., & Pettini, M., 1999, ApJ, 519, 1

Steidel, C. C., Adelberger, K. L., Shapley, A. E., Pettini, M., Dickinson, M., & Giavalisco, M., 2000, ApJ, 532, 170

Stiavelli, M., Scarlata, C., Panagia, N., Treu, T., Bertin, G., & Bertola, F., 2001, ApJ, 561, L37

Venemans, B. P., Kurk, J. D., Miley, G. K., Röttgering, H. J. A., van Breugel, W., Carilli, C. L., De Breuck, C., Ford, H., et al., 2002, ApJ, 569, L11

Wang, J. X., Malhotra, S., & Rhoads, J. E., 2005, ApJ, 622, L77

Westra, E., Jones, D. H., Lidman, C. E., Athreya, R. M., Meisenheimer, K., Wolf, C., Szeifert, T., Pompei, E., et al., 2005, A&A, 430, L21

Williams, R. E., Blacker, B., Dickinson, M., Dixon, W. V. D., Ferguson, H. C., Fruchter, A. S., Giavalisco, M., Gilliland, R. L., et al., 1996, AJ, 112, 1335

Wolf, C., Meisenheimer, K., Kleinheinrich, M., Borch, A., Dye, S., Gray, M., Wisotzki, L., Bell, E. F., et al., 2004, A&A, 421, 913

Yan, H. & Windhorst, R. A. 2004, ApJ, 600, L1

Zacharias, N., Urban, S. E., Zacharias, M. I., Wycoff, G. L., Hall, D. M., Monet, D. G., & Rafferty, T. J., 2004, AJ, 127, 3043

4. STAR FORMATION DENSITY AND Hα LUMINOSITY FUNCTION OF AN EMISSION LINE SELECTED GALAXY SAMPLE AT $Z \sim 0.24$ [1]

Eduard Westra and D. H. Jones, MNRAS, submitted

Abstract

We use narrowband imaging ($FWHM = 70$ Å) to select a sample of emission line galaxies between $0.20 \lesssim z \lesssim 1.22$ in two fields covering 0.5 sq. deg. We use spectroscopic follow-up to select a sub-sample of Hα emitting galaxies at $z \sim 0.24$ and determine the Hα luminosity function and star formation density at $z \sim 0.24$ for both of our fields. Corrections are made for imaging and spectroscopic incompleteness, extinction and interloper contamination on the basis of the spectroscopic data. When compared to each other, we find the field samples differ by $\Delta\alpha = 0.2$ in faint end slope and $\Delta \log[L^*(\mathrm{erg\,s^{-1}})] = 0.2$ in luminosity. In the context of other recent surveys, our sample has comparable faint end slope, but a fainter L^* turn-over. We conclude that systematic uncertainties and differences in selection criteria remain the dominant sources of uncertainty between Hα luminosity functions at this redshift.

We also investigate average star formation rates as a function of local environment and find typical values consistent with the field densities that we probe, in agreement with previous results. However, we find tentative evidence for an increase in star formation rate with respect to the local density of star forming galaxies, consistent with the scenario that galaxy-galaxy interactions are triggers for bursts of star formation.

4.1 Introduction

It is now widely accepted that the amount of star formation in Universe as a whole has increased since the formation of the first galaxies, peaking around redshifts $z \sim 2-3$ and subsequently declining by a factor of ten (e.g. Hopkins 2004, and references therein). Cosmic star formation history provides strong constraints on models of galaxy formation and evolution (Pei et al. 1999; Somerville et al. 2001),

[1] Based on observations made with ESO Telescopes at the La Silla Observatory (Programmes 67.A-0063, 68.A-0363 and 69.A-0314) and the A nglo- Australian Telescope.

because it directly traces the accumulation of stellar mass and metal fraction (Pei & Fall 1995; Madau et al. 1996) to their present-day values (Cole et al. 2001; Panter et al. 2003). Its rapid decline over the past 8 Gyr is consistent with "downsizing" scenarios in which galaxies produce fewer stars per unit mass as they evolve (Heavens et al. 2004; Juneau et al. 2005; Thomas et al. 2005; Fardal et al. 2006). The star formation history of the universe has also been used to constrain allowable stellar initial mass functions (Baldry & Glazebrook 2003; Hopkins & Beacom 2006) and cosmic supernova rates (Gal-Yam & Maoz 2004; Daigne et al. 2006).

Star forming galaxies exhibit a strong UV continuum courtesy of newly formed OB stars in sites of star formation. This newborn population can be inferred from the UV directly (e.g. Treyer et al. 1998; Lilly et al. 1996) or through a host of indirect calibrators spread across the electromagnetic spectrum (Rosa-González et al. 2002; Condon 1992; Schaerer 2000). At low redshifts the most direct calibrator – and the least affected by internal extinction – is the Hα recombination line, which emits when stimulated by ionising UV radiation (e.g. Kennicutt 1998).

Narrowband surveys at optical wavelengths have long been recognised as a powerful way of yielding large samples of emission line galaxies, including those selected by Hα at redshifts $z \lesssim 0.4$ (Ly et al. 2007; Pascual et al. 2007; Jones & Bland-Hawthorn 2001). They are advantageous in that they select galaxies in exactly the same quantity that they seek to measure, and are optimised for the detection of the faint emission line signatures indicative of star formation. Narrowband surveys also have the advantage of a simplified selection function, with filters that probe only a very narrow redshift slice, thereby yielding a volume limited sample at a common distance. Many recent emission line surveys have targeted Lyα at high redshift (Ajiki et al. 2003; Hu et al. 2004; Rhoads et al. 2004; Gawiser et al. 2006), as well as Hα, Hβ, [OIII] and [OII] at lower redshifts (Fujita et al. 2003; Hippelein et al. 2003; Ly et al. 2007).

Here we describe a survey for Hα emission line galaxies at $z \sim 0.24$, found as a by-product of the Wide Field Lyman Alpha Search (WFILAS; Westra et al. 2005, 2006). The resulting sample has been utilised to determine the Hα luminosity function at $z \sim 0.24$ and its associated co-moving star formation density. In Section 4.2 we describe the selection of candidates using narrow- and broadband imaging. In Section 4.3 we detail follow-up spectroscopy used to identify the nature of the emission and test completeness of the sample. In Section 4.4 we derive the Hα luminosity function for galaxies at $z \sim 0.24$ and explore its variation with the local environment in Section 4.5. A summary and concluding remarks are made in Section 4.6.

Throughout this paper we assume a flat Universe with $(\Omega_{\rm m}, \Omega_\Lambda) = (0.3, 0.7)$ and a Hubble constant $H_0 = 70\,{\rm km\,s^{-1}\,Mpc^{-1}}$. All quoted magnitudes are in the

AB system (Oke & Gunn 1983)[2].

4.2 Candidate Selection

4.2.1 Narrowband Imaging

The observations were done with the Wide Field Imager (WFI) on the ESO/MPI 2.2 m telescope at the Cerro La Silla Observatory, Chile. The WFI consists of a four by two array of 2k × 4k CCDs giving a total field size of $34' \times 33'$with pixel scale of $0\farcs238$ per pixel. Imaging data were taken from the Wide Field Lyman Alpha Search (WFILAS; Westra et al. 2005, 2006), a wide-field narrowband survey designed to find Lyman-α Emitters (LAEs) at $z \sim 5.7$. We refer the reader to Westra et al. (2006, hereafter Paper I) for a more detailed description, but give the important features of the survey below.

Three fields spaced around the sky were observed in three narrowband filters ($FWHM = 7$ nm) centred at 810, 817 and 824 nm, an intermediate width filter ($FWHM = 22$ nm) centred at 815 nm and broadbands B and R. For one of the fields with missing 817 nm data it was not possible to apply the selection criteria uniformly and so it was excluded from this analysis. The two fields used were the well-studied Chandra Deep Field South (CDFS; e.g. Rosati et al. 2002; Rix et al. 2004) and the COMBO-17 S11 field (Wolf et al. 2003). The width of our narrowband filters is essentially half that of other surveys (e.g. Fujita et al. 2003; Ly et al. 2007) with a corresponding reduction in background and enhancement in the contrast of observations of emission line galaxies. Table 4.1 gives an overview of the emission lines redshifted into these narrowband filters, the associated luminosity distances and co-moving volumes.

The data were processed using a combination of standard IRAF[3] routines (`mscred`) and some custom designed for our data. Image frames were bias-subtracted, flat-fielded and background-subtracted. A fringe pattern present in the intermediate band and narrowband images, which remained after the flat-fielding, was removed using a fringe frame created from 10–30 science frames. Finally, an astrometric correction was applied using the USNO CCD Astrograph Catalogue 2 (UCAC2; Zacharias et al. 2004).

To ensure the quality of the final deep images we only included frames with a seeing of less than 5 pixels ($=1\farcs2$) and without significant fringing. The images were weighted according to their exposure time and combined using the IRAF `mscstack` routine rejecting deviant pixels.

[2] $m_{AB} = -2.5 \log f_\nu - 48.590$, where m_{AB} is the AB magnitude and f_ν is the flux density in $\mathrm{ergs\,s^{-1}\,cm^{-2}\,Hz^{-1}}$

[3] IRAF is distributed by the National Optical Astronomy Observatories, which are operated by the Association of Universities for Research in Astronomy, Inc., under cooperative agreement with the National Science Foundation.

Table 4.1. Redshift coverage, luminosity distance D_L, and co-moving volume for each emission line in each of our narrowband filters N_{810}, N_{817} and N_{824}

	Emission line				
	Hα	Hβ	[OIII]	[OII]	[S II]
Redshift range in N_{810}	0.229 – 0.239	0.659 – 0.673	0.610 – 0.624	1.163 – 1.182	0.199 – 0.210
Redshift range in N_{817}	0.239 – 0.250	0.673 – 0.687	0.624 – 0.638	1.182 – 1.201	0.210 – 0.220
Redshift range in N_{824}	0.250 – 0.261	0.687 – 0.702	0.638 – 0.652	1.201 – 1.219	0.220 – 0.230
D_L (Mpc)	1203.1	4081.9	3726.3	8158.4	1045.1
$V_{\rm CDFS}$ ($10^3\,{\rm Mpc}^3$)	9.4	60.6	53.6	137.2	7.3
$V_{\rm S11}$ ($10^3\,{\rm Mpc}^3$)	8.3	53.2	47.1	120.6	6.4

The CDFS and S11 fields span differing volumes ($V_{\rm CDFS}$ and $V_{\rm S11}$, respectively). For [OIII] we used the wavelength of the [OIII] $\lambda\,5007$ line and for [OII] and [S II] the average wavelength of the individual lines of each doublet.

4.2.2 Photometry and Completeness Corrections

We used *SExtractor* (version 2.3.2; Bertin & Arnouts 1996) in double image mode to do create the initial source catalogues. Each resulting catalogue contains the photometry for the sources in all 6 filters. Sources were selected when at least 5 pixels were $0.8\,\sigma$ above the noise level in the narrowband image used for detection. All photometry was measured in apertures with a 10 pixel diameter ($= 2\farcs4$). Paper I describes the procedure in detail.

Detection completeness was determined using galaxy number-counts in each of the narrowband images as a function of *AB*-magnitude and that of the Hubble Deep Field (HDF) in the *F*814*W* filter (Williams et al. 1996). Completeness is defined in this instance as the ratio of the number of detected galaxies to that of expected, and the completeness correction is its reciprocal. The expected number counts were fit by a simple linear function over the magnitude range [20, 25]. For all the objects that are selected as our candidates this correction is less than 0.1 %.

4.2.3 Selection Criteria and Star/Galaxy Disambiguation

The following four criteria were applied to select our candidate emission-line galaxies from the initial source catalogues:

1. the narrowband image used as the detection image must have the most flux of all the narrowband images and the source must have a $4\,\sigma$ detection or better in the detected narrowband;

2. there must be at least a $2\,\sigma$ detection in the intermediate band image;

3. the broadband image R needs to have a $2\,\sigma$ detection or better;

4. the emission line flux calculated from the narrowband images should be $F_{\rm line} \geq 10^{-16}\,{\rm erg\,s^{-1}\,cm^{-2}}$.

The emission line fluxes that we use in this paper were measured from the narrowband photometry. The background (or underlying continuum) was determined by averaging the flux measured in the two narrowband images that were *not* used for the detection of the source. This was subtracted from the flux measured in the narrowband detection image, which is emission line and continuum flux combined. An aperture correction was calculated according to:

$$C = \max(0.2, {\rm erf}\left(\frac{10}{2a}\right) \times {\rm erf}\left(\frac{10}{2b}\right)) \tag{4.1}$$

and applied to the line fluxes. Here, C is the fraction of light of the object contained within the 10 pixel aperture, a and b are the profile width along the major

and minor axes, respectively (assuming that the galaxy profile is adequately represented by a two-dimensional Gaussian) and $\mathrm{erf}(x)$ is the error function[4]. To ensure that the fluxes of certain large objects were not over-corrected, we limited C to at least 0.2. Dividing the calculated emission flux by C gives the emission line flux F_{line} used in criterion 4.

The emission line flux limit of $10^{-16}\,\mathrm{erg\,s^{-1}\,cm^{-2}}$ is a factor of two higher than the detection limit of our earlier search for high redshift Lyα emitting galaxies using the same imaging data ($F_{\mathrm{limit}} = 5 \times 10^{-17}\,\mathrm{erg\,s^{-1}\,cm^{-2}}$; Paper I). This is because we are no longer limited by the night-sky background, but rather by the brightness of the object continua. This limit was chosen in part to ensure that emission line candidates were within the sensitivity limits of our follow-up confirmation spectroscopy.

Stars represent a significant fraction of contaminants. We found that standard star/galaxy classification from *SExtractor* works satisfactorily for objects brighter than $R = 21$. However, it breaks down for the large number of faint ($R > 21$) objects. Therefore, additional criteria were applied. We examined the size of the objects (major and minor axes), in combination with their shape (the ratio of the major and minor axes) as additional star/galaxy discriminants. Since this size/shape information could potentially lead to the unwanted removal of unresolved line emitting galaxies, we used an additional cut in $(B - R)$ colour as a safeguard to prevent this. The colour cut was chosen to separate unresolved star forming galaxies at $z \sim 0.24$ from the vast majority of early type galaxies (at all redshifts), which are not likely to have significant star formation. We decided to restrict the size/shape discrimination to sources with $(B - R) \geq 1.4$ using the $(B - R)$ colour distribution of Hα emitters at $z \sim 0.24$ and [S II] emitters at $z \sim 0.21$ (confirmed subsequently through follow-up spectroscopy) as a guide. We finalised our stellar selection criteria as follows:

1. the *SExtractor* CLASS_STAR parameter is ≥ 0.95 and $R < 21$. At $R > 21$, sources are too faint for *SExtractor* to reliably distinguish between stars and galaxies;

2. the *SExtractor* A_IMAGE and B_IMAGE parameters (the profile in pixels along the major and minor axes, respectively) are ≤ 4 pixels, the ratio of these parameters is $\frac{\mathrm{A\_IMAGE}}{\mathrm{B\_IMAGE}} \leq 1.06$ and the object has a $(B - R)$ colour ≥ 1.4. This is redder than almost all star forming galaxies at $z \sim 0.24$;

3. the object showed obvious imaging artefacts, such as diffraction spikes or ghost images, in any of its thumbnails.

Figure 4.1 shows the distribution of spectroscopically observed objects that satisfy these criteria as a function of observed $(B - R)$ colour for the CDFS field. The

[4] The error function is defined as $\mathrm{erf}(x) = \frac{2}{\sqrt{\pi}} \int_0^x e^{-t^2} dt$

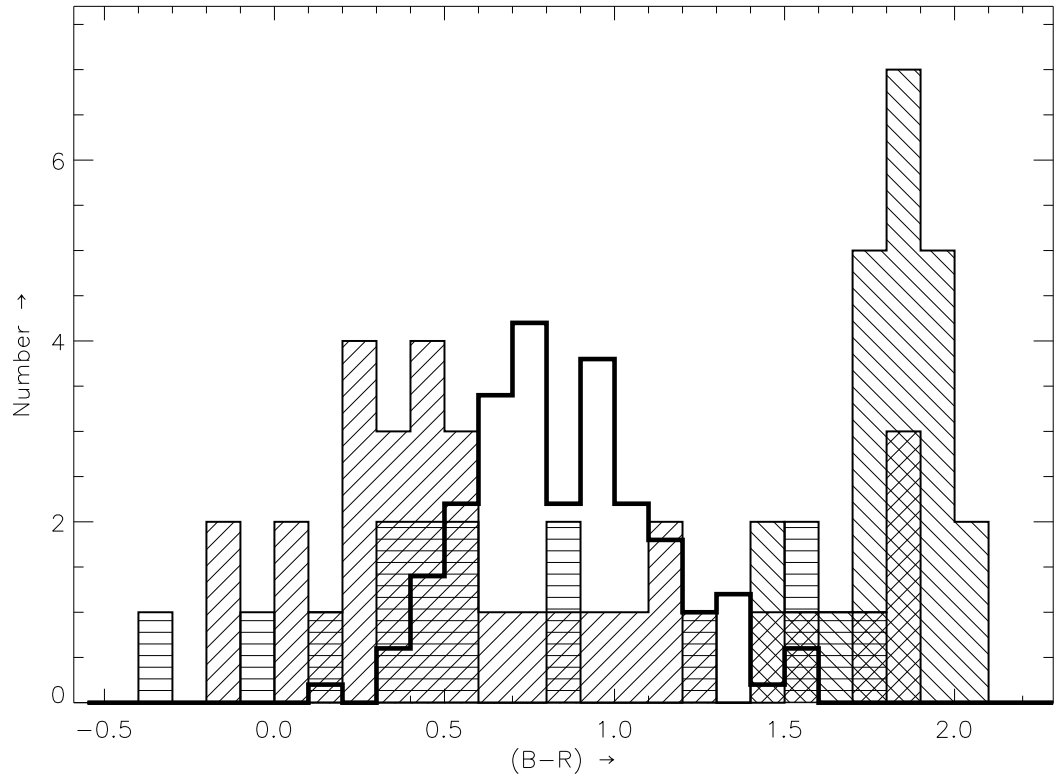

Fig. 4.1: Distribution of observed $(B-R)$ colour for narrowband candidates satisfying various criteria for stellarity: (*a*) *SExtractor* CLASS_STAR ≥ 0.95 and $R < 21$ (*forward cross-hatching*), (*b*) *SExtractor* $\frac{\text{A\_IMAGE}}{\text{B\_IMAGE}} \leq 1.06$ and $(B-R) \geq 1.4$ (*backward cross-hatching*) and (*c*) bright stars showing diffraction spikes or ghost reflections (*horizontal cross-hatching*). The thick histogram shows the combined distribution of Hα and [S II] galaxies ($z \sim 0.24$ and $z \sim 0.21$, respectively) from our full emission line sample subsequently through follow-up spectroscopy (Section 4.3.1), scaled by 0.2.

forward cross-hatched histograms represent objects satisfying criterion 1, the backward cross-hatched those for criterion 2, and the horizontal cross-hatched those for criterion 3. The histogram outlined by the thick solid line represents the observed $(B-R)$ colour distribution of securely confirmed Hα and [S II] emitters ($z \sim 0.24$ and $z \sim 0.21$, respectively), by way of comparison. All objects selected in this way were deemed to be stellar and removed from the candidate list. Finally, all candidates were inspected to remove sources that were contaminated by image artefacts.

From initial candidate numbers of 786 and 848 for the CDFS and S11 fields respectively, 414 and 513 candidates were removed because they met one or more of the stellar criteria. Our final sample yielded 372 candidate emission-line galaxies for the CDFS field and 335 for the S11 field.

4.3 Spectroscopic Follow-up

4.3.1 Observations and Reduction

The emission-line selection criteria established in Section 4.2.3 are sensitive to almost any galaxy with emission lines that have been redshifted into the wavelength range of our narrowband filters, and are bright enough to be detected. The one exception is Lyα, which does not yield detectable flux blueward of the Lyman limit and hence in our broadband images. The main emission lines to expect in our narrowband filters are (from bluest to reddest), [OII] $\lambda\lambda$3726,3728, Hγ λ4342 (although usually too faint, or too much underlying absorption), Hβ λ4863, [OIII] $\lambda\lambda$4959,5007, Hα λ6564 and [S II] $\lambda\lambda$6733,6718. Since the goal of this paper is to establish the star formation density at $z \sim 0.24$, we concentrated only on those galaxies detected as Hα. Alternative approaches by other groups (e.g. Ly et al. 2007) have separated objects based on their broadband colours. Unfortunately, in the case of [S II] galaxies ($z \sim 0.21$) the colours are indistinguishable from those with Hα ($z \sim 0.24$) due to their similar redshifts. Figure 4.2 shows how the Hα and [S II] galaxies occupy the same range of colour [$(B - R) \gtrsim 0.5$] given their near-identical redshifts. Based on this, we classify all of the single-line emitters outside this range [$(B - R) \leq 0.5$] as likely [OII] line-emitters at $z \sim 1.2$. It is worth pointing out that when the [S II] doublet falls inside our narrowband filter set, an extra volume of about 50 % of the volume probed by Hα can be explored. Unfortunately, the fluxes of [S II] and Hα are not sufficiently correlated to permit star formation density determinations from the [S II] line (e.g. Kewley et al. 2001), and so it was not used.

Our approach was to target as large a sample as possible of our candidates to test how successful our candidate selection was. An additional aim was to measure the fraction of the observed candidates with Hα in our narrowband filters. To do this, we ensured that the spectroscopic sample was representative of the narrowband sample as a whole. A two-sided Kolmogorov-Smirnov test yielded probability levels of 99.8 % and 49.3 % for the CDFS and S11 fields, respectively. Once measured, we applied the determined fraction to our entire sample of candidates in each field.

The spectroscopic data were taken with AAOmega (Sharp et al. 2006), an optical multi-object spectrograph. It is fibre-fed from the prime focus of the Anglo-Australian Telescope (AAT) by the 2dF facility (Lewis et al. 2002b) to a dual-beam spectrograph, which in our case was used with spectral ranges 3800–5700 Å and 5700–8700 Å. The resolving power was $\delta\lambda = 3.5$ Å in the blue arm and $\delta\lambda = 5.3$ Å in the red arm. It has 392 fibres available to observe spectra of objects within a 2 degree field of view. The fibres have a minimum placement separation of 30″, although the actual limiting separation depends on the orientation of fibre buttons when placed on the field plates. For fields with a high density of targets, such as our

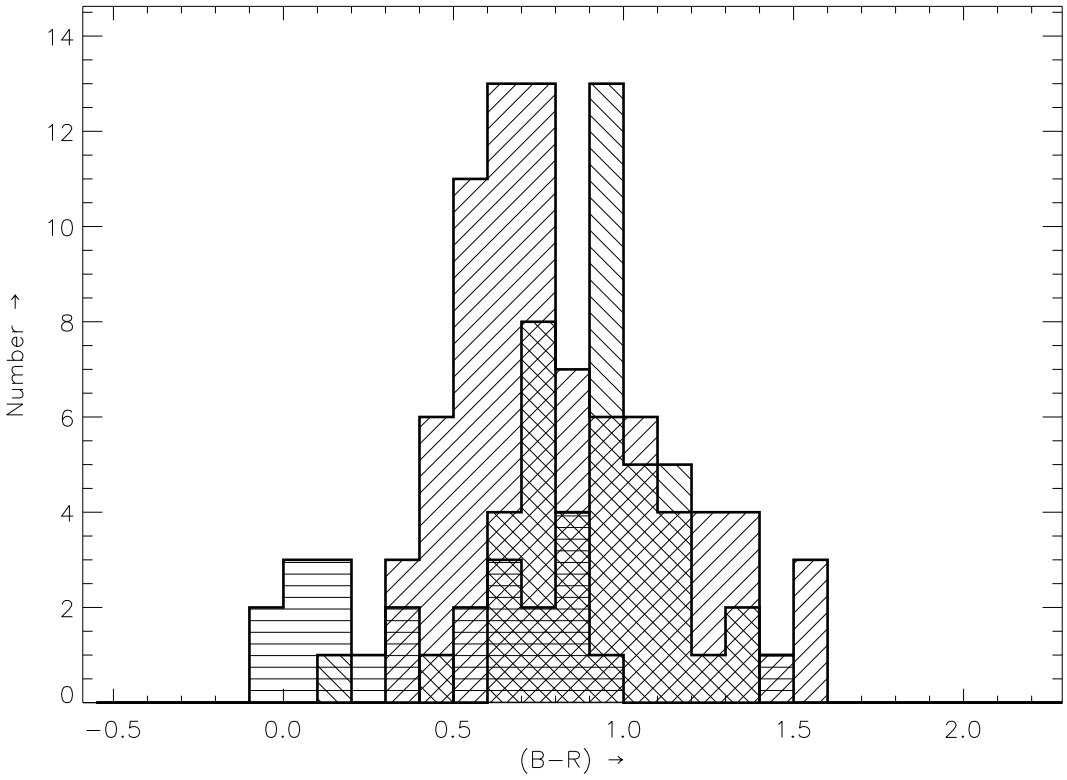

Fig. 4.2: Observed $(B - R)$ colour distribution for various sets of emission-line galaxies within our sample: (*a*) Hα at $z \sim 0.24$ (*forward cross-hatching*), (*b*) [S II] at $z \sim 0.21$ (*backward cross-hatching*) and (*c*) single-line emitters of indeterminate origin (*horizontal cross-hatching*).

$0.5^\circ \times 0.5^\circ$ fields, only ~ 250 fibres could be allocated per configuration, due to such placement limitations. In general, the number of fibres allocated depends upon the target distribution in the field and the choice of algorithm in the `configure`[5] software. We found that using the Simulated Annealing algorithm (Miszalski et al. 2006) allowed a larger fraction of fibres to be allocated to candidates than the older Oxford algorithm.

The data were taken during four separate runs. The first observations were done in classical mode during 2 nights, 2006 March 23 and 24. During this run the S11 field was observed. The other three occasions were done in service mode on 2006 October 10, 2006 November 10, and 2007 March 26. During these runs both fields were targeted. We used the 580V and the 385R volume phase holographic (VPH) gratings for the blue and red arm, respectively. Table 4.2 summarises the observations.

Basic spectral reductions, including bias-subtraction, flat-fielding and wavelength calibration were done using the 2dF reduction pipeline `drcontrol`[5]. The final one-dimensional spectrum for each object was obtained by averaging the re-

[5] `configure` and `drcontrol` are software packages produced and maintained by the AAO. These packages can be obtained from `ftp://ftp.aao.gov.au/pub/2df`

Table 4.2. Details of the spectroscopic follow-up observations

observing dates	field observed	number of configurations	tot. exp. time (sec)	seeing ($''$)
2006/03/23	S11	2	11,700	0.9–1.5
2006/03/24	S11	3	14,400	1.3–1.8
2006/10/10	CDFS	1	9,900	1.8–2.2
2006/11/10	CDFS	1	11,700	1.2–1.5
2007/03/26	S11	1	6,300	2.5

duced spectra of the object in the different observations using our own IDL scripts.

The spectra of several standard stars (LTT 7379, LTT 7987 and CD-32 9927; Bessell 1999) were taken during the final night of the 2006 March run and were reduced in the same fashion as the science data. System throughput as a function of wavelength was derived using each standard star and its sensitivity curve. These curves were scaled to a common level and averaged to give the overall sensitivity. This was applied to all the science spectra to flux calibrate each relative to one another. Unfortunately, absolute flux calibrations are very difficult to do reliably with fibre-based spectrographs, due to the changing configurations of the fibres and the effect this has on their throughput. For this reason, we used the line fluxes measured from our narrowband photometry rather than the fibre spectroscopy.

4.3.2 Spectroscopic Completeness

We used a Monte-Carlo simulation that combined the background of real spectra of our securely confirmed Hα emitting galaxies with transplanted and scaled emission lines to asses our spectroscopic completeness as a function of line flux. We took the spectrum of each Hα emitter and fitted the Hα and [N II] lines together with the continuum. Each line was fitted by a Gaussian and the galaxy continuum (or background sky) was approximated by a first order polynomial. The line centres were parameterised by redshift. The widths of the [N II] lines were set equal and the flux ratio between the red and blue [N II] lines was fixed to 2.96 (Mendoza 1983). The remaining fit parameters were left unconstrained. The model of the Hα-[N II] complex was subtracted from our data, leaving only the underlying noise. To the noise, we added a randomly scaled version of our model with a random offset in wavelength. We then attempted to re-identify any emission line. We did this multiple times for each secure Hα emitting galaxy.

This exercise demonstrated that it was possible to identify at least 90 % of the galaxies at a line flux of $\log F_{\rm line} = -16.0$ ($F_{\rm line}$ in erg s^{-1} cm^{-2}) for all spectroscopic runs. In Figure 4.3 the recovered fraction as a function of line flux is shown for the CDFS and S11 fields. The uncertainties indicated in Figure 4.3 were derived

using the following relation:

$$\sigma_{\rm frac} = \frac{\sqrt{N_{\rm tot}(N_{\rm det}+2)(N_{\rm tot}-N_{\rm det}+1)}}{N_{\rm tot}(N_{\rm tot}+3)} \ , \tag{4.2}$$

where $\sigma_{\rm frac}$ is the calculated uncertainty, $N_{\rm tot}$ the total number of objects in that bin and $N_{\rm det}$ is the number of objects which have a detection of the emission line (after Eq. 4 from Jones et al. 2006). The spectroscopic completion rate is well fit by a function of the form

$$\eta(F) = \begin{cases} \exp[-\gamma(F-F_c)^{20}] & F < F_c \\ 1 & F \geq F_c \end{cases} \ , \tag{4.3}$$

where γ represents the speed at which the function drops off and F_c is the flux at which the function reaches 1.0.

4.3.3 Hα Emission Line Fraction

In almost all cases the spectra of confirmed emission-line galaxies should show additional emission lines elsewhere except cases of Lyα at $z \sim 5.7$ (which are filtered out through their absence of B and R flux) or [OII] at $z \sim 1.2$. This is demonstrated by Figure 4.4, where we show the stacked spectrum of all our confirmed Hα and [S II] galaxies in the CDFS. Hα is usually accompanied by the [N II] $\lambda\lambda$6550,6585 and [S II] $\lambda\lambda$6733,6718 doublets, whereas Hβ and the [OIII] $\lambda\lambda$4959,5007 doublet are almost always seen together. Our spectral resolution ($R \sim 1500$ at 8150 Å) is not enough to fully resolve the [OII] doublet, but high enough to show it as broader than a single emission line. The signal-to-noise ratio of the spectra is not always high enough to clearly determine if a line is broad (in this sense) or not. Alternatively, these galaxies could be Hα emitting galaxies with all other emission lines too faint to be detected.

There are a few galaxies which show only one emission line. Although we expect many of them to be [OII] emitters at $z \sim 1.2$, we cannot rule out the possibility of single-line Hα galaxies at $z \sim 0.24$ in without the use of additional information. In Figure 4.2 we show the observed $(B-R)$ colour distribution of galaxies in the CDFS where the emission line in the narrowband filters has been confirmed as Hα or [S II] through the presence of additional lines. We also indicate the colour distribution of galaxies for which we have only one emission line feature. Some of the single-line detections are bluer than the combined Hα/[S II] distribution. We therefore identify all single-line galaxies with $(B-R) \leq 0.5$ to be [OII] emitters at $z \sim 1.2$ and those with $(B-R) > 0.5$ to be Hα emitters at $z \sim 0.24$.

Of the candidates for which we have spectroscopically confirmed an emission line (189 and 117 in total for the CDFS and S11 fields, respectively), just under a half are Hα at $z \sim 0.24$, a quarter are [S II] at $z \sim 0.21$, roughly a sixth are Hβ or [OIII] at $z \sim 0.6-0.7$ and the remainder are [OII] at $z \sim 1.2$.

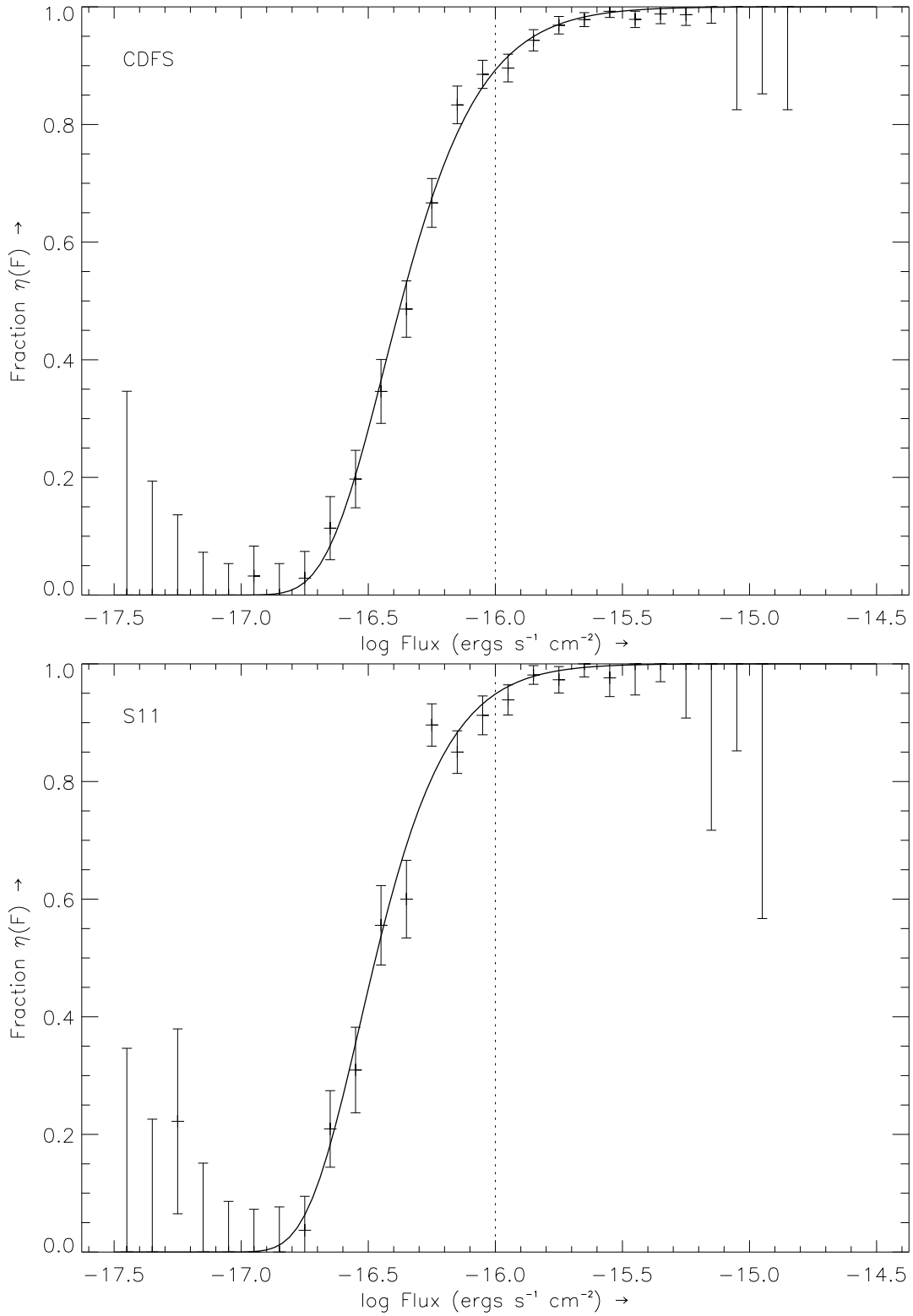

Fig. 4.3: Spectroscopic completeness as a function of line flux for the CDFS (*top*) and S11 (*bottom*) fields as derived from a Monte-Carlo simulation of artificially generated emission lines. See text for details.

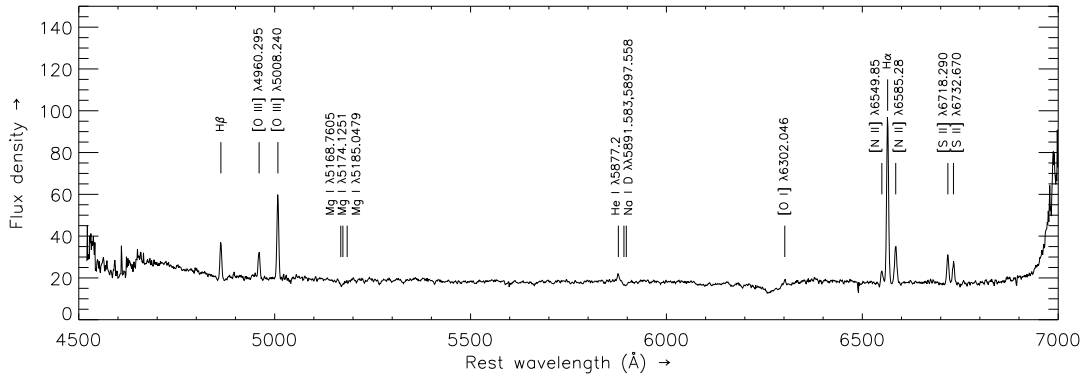

Fig. 4.4: Mean spectrum of emission-line galaxies from the CDFS field. Spectra from 114 galaxies between $z = 0.19$ and 0.27 were de-redshifted before stacking. The most prominent features have been labelled. The apparent absorption feature just bluewards of the [OI] λ6302 line is the remnant of the telluric A-band of the individual spectra being de-redshifted and stacked. This spectrum was used to fit the emission lines to derive the mean extinction as described in Section 4.3.4. Only red arm data from AAOmega (observed wavelength $\sim 5700 - 8700\,\text{Å}$) are shown.

Figure 4.5 shows the fraction of confirmed Hα emitters in our full spectroscopic sample as a function of narrowband flux. It peaks around $\log F_{\text{line}} \sim -15.3$ (with F_{line} in $\text{erg}\,\text{s}^{-1}\,\text{cm}^{-2}$), below which increasing numbers of [OII] galaxies at $z \sim 1.2$ begin to dominate the counts. Each point in Figure 4.5 has a minimum of 10 galaxies per bin and a minimum binwidth of 0.1 dex. The uncertainties in the Hα fraction per bin have been calculated using Eq. 4.2, where N_{det} now represents the number of galaxies with confirmed Hα. We fit a Gaussian of the form

$$\xi(F) = a \times \exp\left(\frac{(F - F_c)}{\sigma^2}\right) + b\ , \tag{4.4}$$

where F_c is the flux central to the peak, σ and a are its width and height, and b is a zero-point offset. The resulting fits are shown in Figure 4.5.

We decided to fit both the CDFS and S11 fields individually, given the likely differences between the field samples due to cosmic variance. Given the relatively narrow range of volume probed through each emission line, we expect over- and underdensities at the different redshift intervals to change the relative numbers of galaxies as a function of flux (Jones & Bland-Hawthorn 2001; Pascual et al. 2001).

4.3.4 Extinction Corrections

Star forming regions are some of the dustiest galaxy environments, making correction for internal obscuration necessary. Many emission line surveys apply a general extinction correction of $A_{\text{H}\alpha} \sim 1$ (e.g. Tresse & Maddox 1998; Fujita et al. 2003). However, it has been shown that there are large variations in extinction between

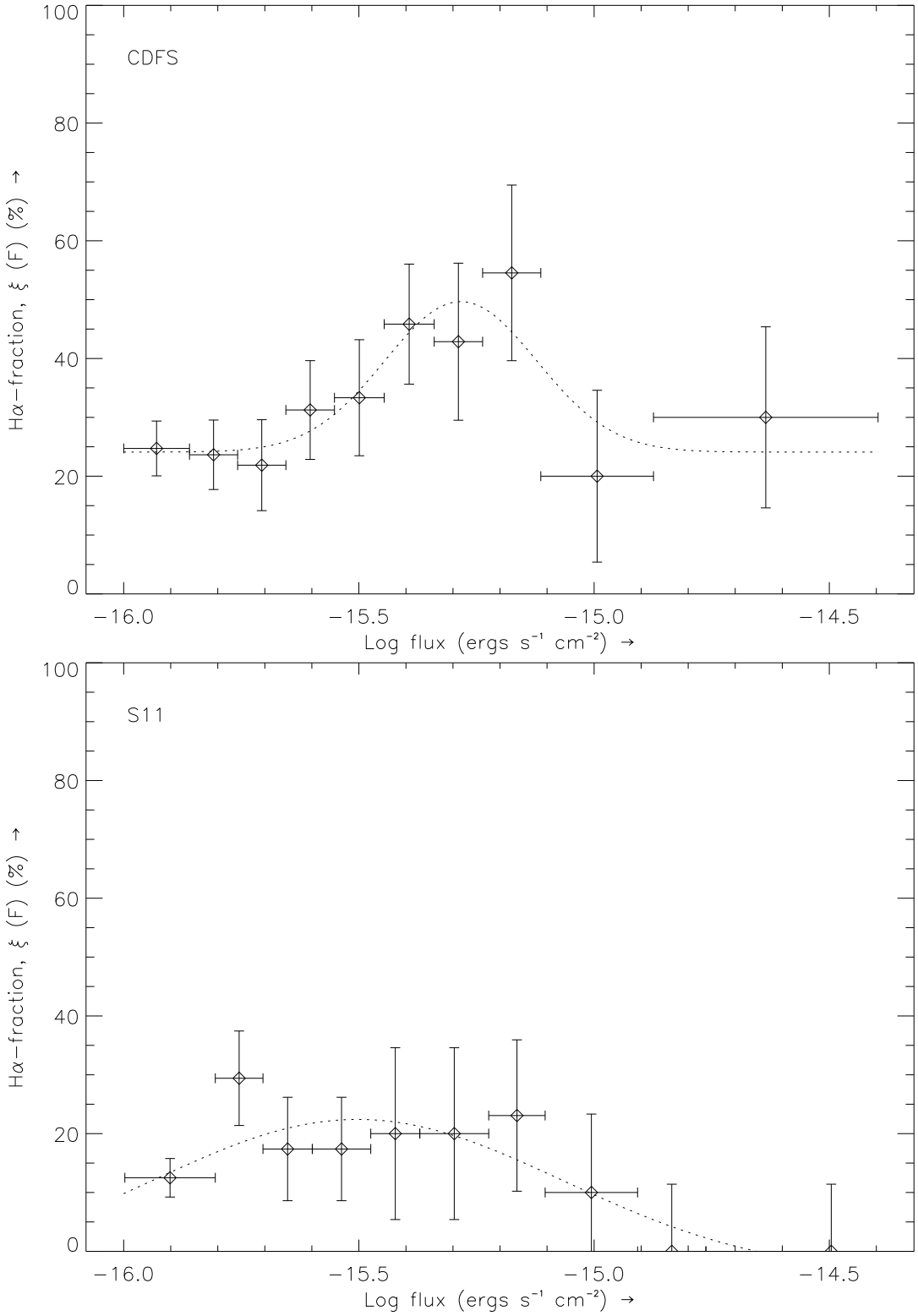

Fig. 4.5: The Hα fraction of our candidates for the CDFS (*top*) and S11 (*bottom*) fields. The data have been binned to have a minimum of 10 galaxies per bin and a minimum width of 0.1 dex. The dotted line is the four-parameter fit to the data points. The horizontal error-bars represent the width of the bins and the vertical bars the uncertainty in the fraction calculated using Eq. (4.2).

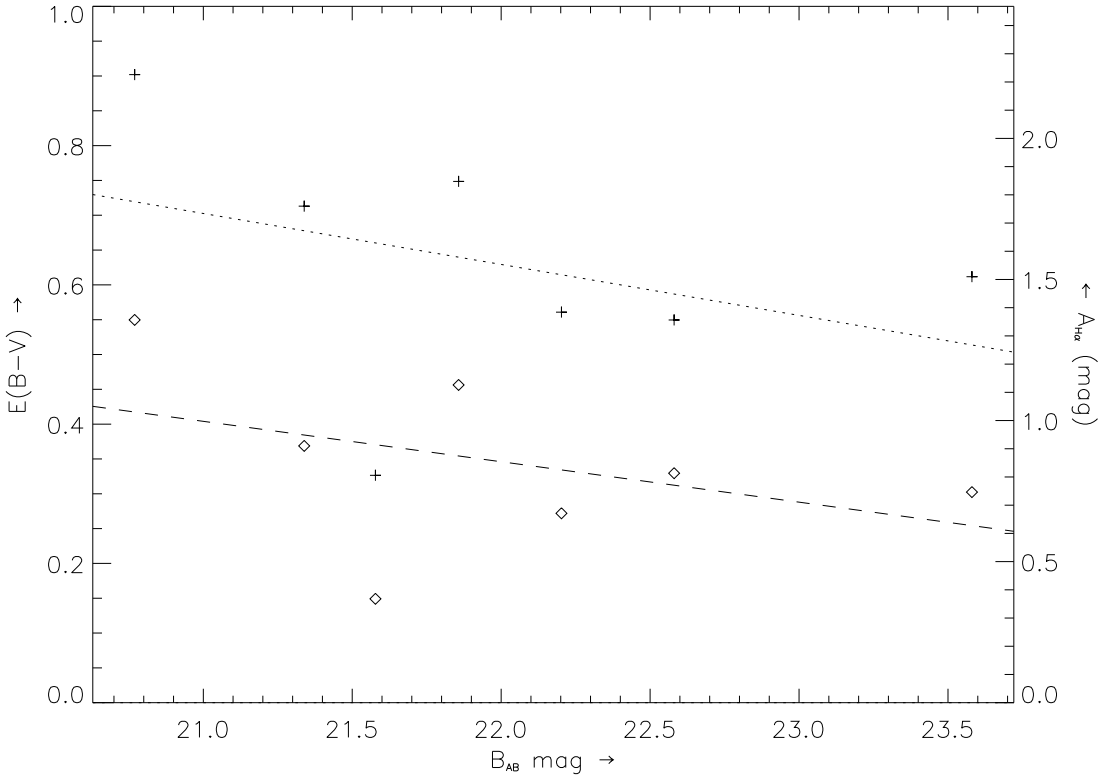

Fig. 4.6: Colour excess E(B-V) and $A_{\mathrm{H}\alpha}$ (assuming $k(\mathrm{H}\alpha) = 2.47$) as a function of B-magnitude as determined by measuring the Balmer decrement of the averaged spectra in the CDFS. The crosses indicate the colour excess without using any correction for stellar absorption in Hα and Hβ. The diamonds indicate the colour excess using the same stellar absorption correction as Hopkins et al. (2003) with EW(Hα) = 1.3 and EW(Hβ) = 1.6. The dotted and dashed line are the linear fits to the respective points.

galaxies (e.g. Jansen et al. 2001). Furthermore, Massarotti et al. (2001) state that applying an average extinction correction always underestimates the true extinction correction. Since our spectra cover a large wavelength range (3800–5700 Å in the blue and 5700–8700 Å in the red) we are able to observe Hα and Hβ simultaneously. We therefore calculate the extinction individually for each galaxy through Hα and Hβ when both lines are detectable. The signal-to-noise ratio is not always high enough to show Hβ clearly in emission. Therefore, we grouped available spectra according to the B-magnitude of the source, obtained an average spectrum, and measured the Balmer decrement value from these.

The colour excess $E(B-V)$ can be calculated using

$$E(B-V) = \frac{2.5 \log R_{\alpha\beta}}{k(\mathrm{H}\beta) - k(\mathrm{H}\alpha)} \ , \tag{4.5}$$

where $R_{\alpha\beta}$ is the ratio of the observed value of the Balmer decrement to its theoretical value, and $k(\mathrm{H}\beta) - k(\mathrm{H}\alpha)$ is the differential extinction between the wavelengths of Hβ and Hα. The theoretical value for the Balmer decrement is 2.87 (for

$T = 10^4$ K and case B recombination; Table 2 of Calzetti 2001) and the value for the differential extinction is 1.163. This assumes $k(V) = 3.1$ and $k(\mathrm{H}\alpha) = 2.468$. We adopt these values throughout the rest of this paper.

In Figure 4.6 we plot the resulting values for $E(B-V)$ as a function of the B-magnitude for two cases: without and with correction for absorption due to the underlying stellar population. The AAOmega spectra have a resolution of ~ 5.3 Å throughout the red arm meaning that we are unable to resolve the Hβ absorption line directly. If we assume no stellar absorption, the colour excess has values up to $E(B-V) \sim 1$, corresponding to $A_{\mathrm{H}\alpha} = 2.5$ mag (or $A_{\mathrm{V}} = 3.2$ mag) using $A_\lambda = k(\lambda) \times E(B-V)$. This is far higher than the average extinction of $A_{\mathrm{H}\alpha} \sim 1$ as assumed elsewhere (e.g. Tresse & Maddox 1998; Fujita et al. 2003). If we instead adopt the median equivalent widths for stellar absorption in Hα and Hβ as measured by Hopkins et al. (2003), 1.3 and 1.6 Å respectively, then the average extinction as shown in Figure 4.6 is roughly $A_{\mathrm{H}\alpha} \sim 0.85$. We note that there is a trend of a decreasing extinction with increasing apparent magnitude (see Figure 4.6). Observe that our sample has a restricted range in redshift, making apparent magnitude B a proxy for absolute magnitude M_B. Similar trends of change in $E(B-V)$ have been found by Jansen et al. (2001). We attribute this trend to the fact that either fainter (and therefore smaller) galaxies potentially contain less dust, or the Hβ flux might be overestimated in mean spectrum of the faintest galaxies as a result of a low signal-to-noise ratio of the Hβ line. We derive an extinction of $A_{\mathrm{H}\alpha} = 0.96$ from the Balmer ratio in the mean spectrum of all emission-line galaxies as shown in Figure 4.4. Since the trend might be due to a low signal-to-noise ratio of the Hβ line, we use a constant value throughout to correct for extinction.

4.4 Luminosity Function and Star Formation Density

4.4.1 Derivation and Fit

With the final emission line catalogue in hand, and the various selection and completeness effects accounted for, our approach to calculating the Hα luminosity function is as follows. We take our measured distribution of line emitters (all emission lines from all redshifts) from the narrowband candidate sample and apply the spectroscopically measured fraction of Hα emitters as a function of flux (Section 4.3.3). We correct for incompleteness in both the spectroscopic identifications (Section 4.3.2) as well as the original narrowband imaging. The corrections for the latter are less than 0.1 % (Section 4.2.2). Finally, we correct our line fluxes for the effects of extinction (Section 4.3.4).

Figure 4.7 shows separate luminosity functions for both the CDFS and S11 fields. We fit a Schechter function (Schechter 1976) to the data points using a

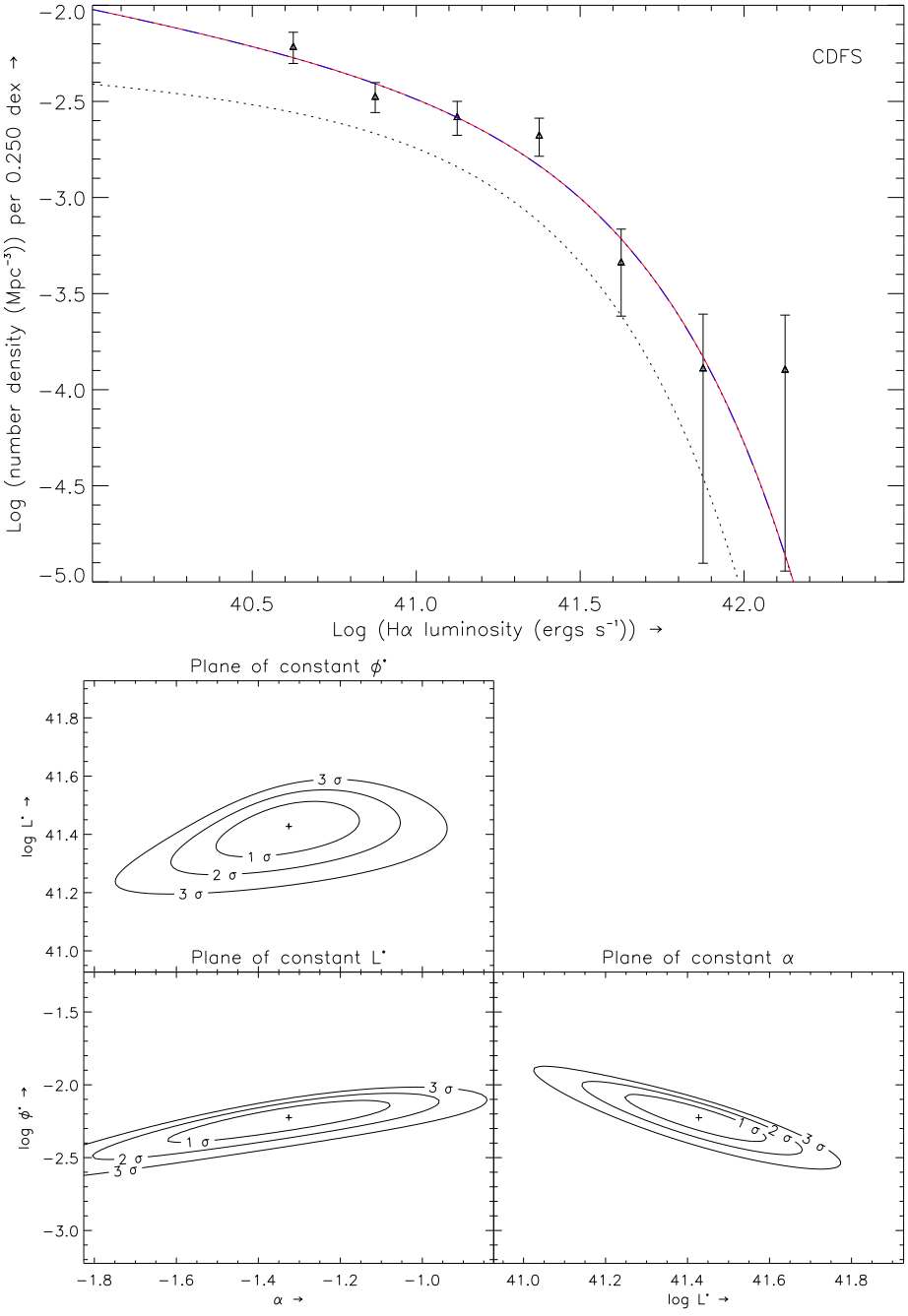

Fig. 4.7: *Top*: luminosity function for Hα galaxies at $z \sim 0.24$ for the CDFS (*left*) and S11 (*right*) fields. The solid line in each of these panels is the fit to the data points, while the dotted line indicates the fit of other field for reference. *Bottom*: Confidence levels for the parameters α, L^* and ϕ^* of the CDFS (*left*) and S11 (*right*) fields. Contours are drawn for each plane in which one of the parameters is held constant. The 1, 2 and 3 σ contours indicated correspond to 68.3%, 95.4% and 99.7% confidence limits, respectively.

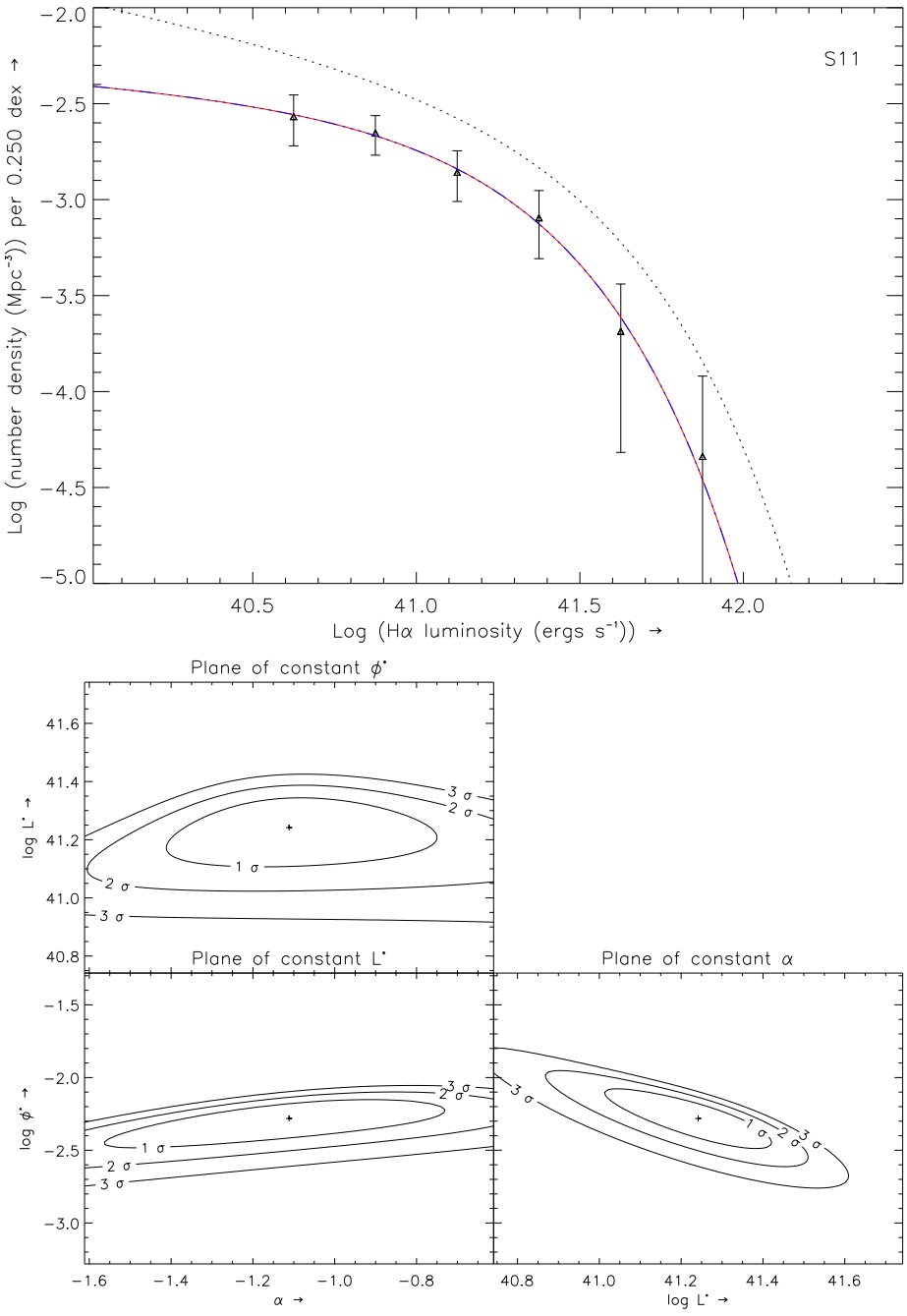

Fig. 4.7 (continued): for the S11 field.

minimised χ^2 fit. The Schechter function is given by

$$\phi(L)dL = \phi^* \left(\frac{L}{L^*}\right)^{-\alpha} \exp\left(-\frac{L}{L^*}\right) d\left(\frac{L}{L^*}\right) \ , \tag{4.6}$$

where ϕ^* represents the normalisation constant of the galaxy density, α the faint end slope, and L^* the characteristic luminosity where the Schechter function rapidly declines at bright luminosities. We used a Levenberg-Marquardt method for finding the minimum χ^2, courtesy of the IDL routine `mpfitfun` from the Markwardt[6] library. Since the three parameters α, L^* and ϕ^* are highly correlated, we used the correlation matrix and the partial derivatives of the Schechter function to calculate the formal uncertainty in the integrated luminosity density $\mathcal{L}$,

$$\sigma^2_{\mathcal{L}} = \sum_{i,j=1}^{3} \left[\frac{\partial \mathcal{L}}{\partial x_i}\frac{\partial \mathcal{L}}{\partial x_j}\right]_{x=\mu} V_{ij} \ . \tag{4.7}$$

Here, x_1, x_2 and x_3 correspond to the Schechter parameters α, $\log L^*$ and $\log \phi^*$ (Cowan 1998). V_{ij} is the covariance matrix, which relates to the correlation matrix ρ_{ij} as $V_{ij} = \rho_{ij}\sigma_i\sigma_j$. σ_i is the formal uncertainty in the i^{th} parameter. We list the resulting values of the parameters and the formal uncertainties, together with the correlation matrices in Table 4.3.

The luminosity density over luminosities $L \geq L_{\text{lim}}$ can be calculated by integrating Eq. 4.6, yielding

$$\mathcal{L} = \phi^* L^* \Gamma(\alpha + 2, \frac{L_{\text{lim}}}{L^*}) \ . \tag{4.8}$$

In the case where limiting luminosity $L_{\text{lim}} = 0$, the luminosity density reduces to $\mathcal{L} = \phi^* L^* \Gamma(\alpha + 2)$. Using the Schechter parameters and uncertainties given in Table 4.3 with $\log L_{\text{lim}} = 40.6$ (L_{lim} in $\text{erg}\,\text{s}^{-1}$, corresponding to our survey flux limit) gives $\log \mathcal{L} = 39.17^{+0.08}_{-0.10}$ and $38.86^{+0.11}_{-0.14}$ in $\text{erg}\,\text{s}^{-1}$ for the CDFS and S11 fields, respectively. The uncertainties are calculated using the correlation matrices in Table 4.3. If we instead use the Hα luminosities of the galaxies directly and sum over all, we obtain $39.22^{+0.02}_{-0.02}$ and $38.86^{+0.03}_{-0.03}$ for CDFS and S11, respectively. The uncertainties in this case are the square-root of the sum in quadrature of individual galaxy luminosity uncertainties and does not take into account Hα emission line fraction uncertainties and, as such, are lower limits.

4.4.2 Comparison to Previous Surveys

In Figure 4.8 we compare our Schechter fits to the results of other surveys using Hα as a measure for star formation. The survey parameters are summarised in Table 4.4. We restricted the comparison to Hα surveys with $z \lesssim 0.40$ in order to limit the systematic uncertainties which play into the comparison when different

[6] Maintained by C. Markwardt at http://cow.physics.wisc.edu/∼craigm/idl/idl.html.

Table 4.3. Schechter parameters for the Hα luminosity functions and the correlation matrices

CDFS			S11		
α	$\log L^*$	$\log \phi^*$	α	$\log L^*$	$\log \phi^*$
-1.33 ± 0.34	41.43 ± 0.22	-2.23 ± 0.32	-1.11 ± 0.51	41.24 ± 0.25	-2.28 ± 0.33
$\begin{pmatrix} 1.00000 & -0.91020 & 0.96458 \\ -0.91020 & 1.00000 & -0.97268 \\ 0.96458 & -0.97268 & 1.00000 \end{pmatrix}$			$\begin{pmatrix} 1.00000 & -0.90948 & 0.95099 \\ -0.90948 & 1.00000 & -0.96826 \\ 0.95099 & -0.96826 & 1.00000 \end{pmatrix}$		

Schechter parameters for the Hα luminosity functions for each field determined using a Levenberg-Marquardt χ^2 minimisation. The correlation matrices ρ_{ij} for each are shown below.

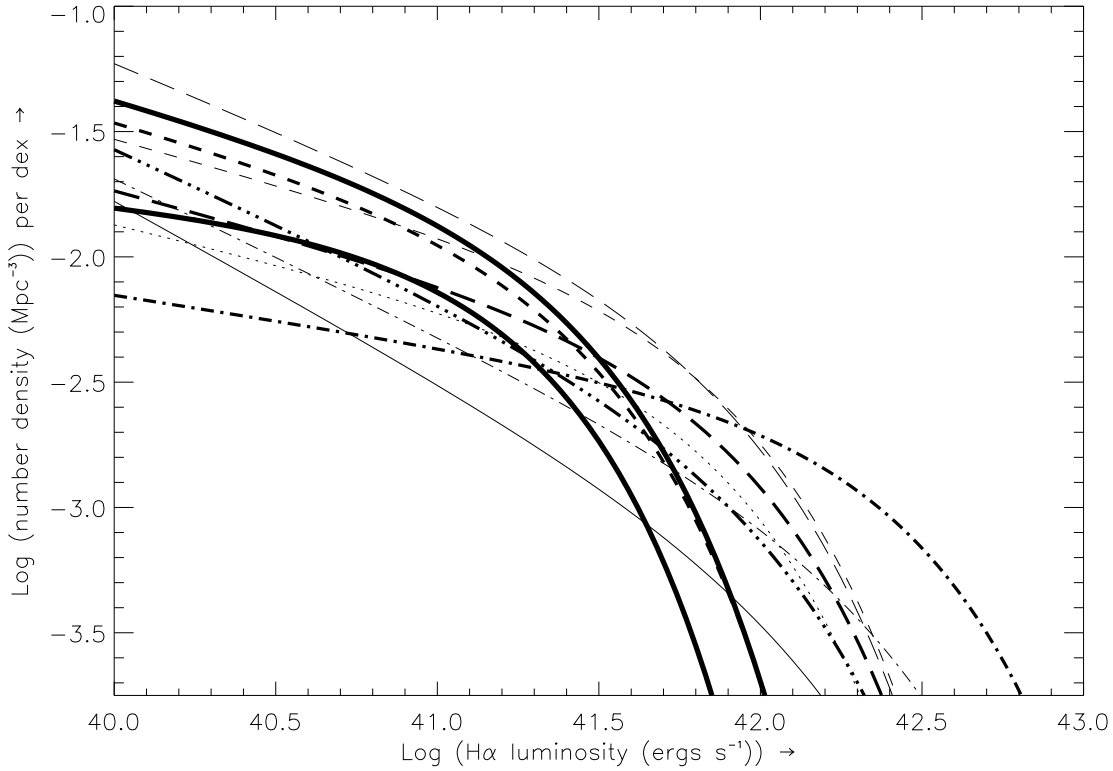

Fig. 4.8: Comparison of the Schechter functions derived for our two fields (thick solid lines) and those of other surveys. The other surveys are Gallego et al. (1995, dot), Tresse & Maddox (1998, dash), Sullivan et al. (2000, dash dot), Fujita et al. (2003, long dash), Hippelein et al. (2003, thick short dash), Pérez-González et al. (2003, thick dash dot) and Ly et al. (2007, $z = 0.07, 0.09$ thick dash dot dot dot; $z = 0.24$ solid; $z = 0.40$ thick long dash). The individual Schechter parameters are given in Table 4.4.

star formation indicators are involved. It can be seen that there is a large range in each of the Schechter parameters between surveys. α ranges from ~ -1.1 to -1.6, $\log L^*$ from ~ 41.3 to 42.2 and $\log \phi^*$ from -3.7 to -2.2. Some of these surveys cover different redshifts to those in our survey. The wide span of the parameters could be attributed by evolution of the luminosity function, as has been suggested by Hopkins (2004) and Ly et al. (2007), who compare surveys over a wider redshift range using different indicators. However, a number of systematic uncertainties exist between surveys that could also attribute to the scatter between the luminosity functions. We now explore each in turn.

The details of galaxy selection inevitably vary from survey to survey. For example, Tresse & Maddox (1998) have selected their galaxies from an I-band selected sample, while Sullivan et al. (2000) used UV imaging to select theirs. It is well known that galaxy selection based on different passbands results in a different faint end slope of the galaxy luminosity distribution (Madgwick et al. 2002; Jones et al. 2004). Passbands that favour bluer and/or star forming galaxies generally

Table 4.4. Values for the parameters of all Schechter functions shown in Figure 4.8

Reference/field	Redshift	α	$\log L^*$	$\log \phi^*$
Gallego et al. (1995)	0.022 ± 0.022	-1.30 ± 0.20	41.87 ± 0.08	-2.79 ± 0.20
Tresse & Maddox (1998)	0.200 ± 0.100	-1.35 ± 0.06	41.92 ± 0.13	-2.56 ± 0.09
Sullivan et al. (2000)	0.150 ± 0.150	-1.62 ± 0.10	42.42 ± 0.14	-3.55 ± 0.20
Fujita et al. (2003)	0.242 ± 0.009	-1.53 ± 0.15	41.95 ± 0.25	-2.62 ± 0.34
Hippelein et al. (2003)	0.245 ± 0.022	-1.35	41.45	-2.32
Pérez-González et al. (2003)	0.025 ± 0.025	-1.20 ± 0.20	42.43 ± 0.17	-3.00 ± 0.20
Ly et al. (2007)	0.0735 ± 0.0075, 0.0855 ± 0.0055	-1.59 ± 0.02	42.05 ± 0.07	-3.14 ± 0.09
Ly et al. (2007)	0.242 ± 0.009	-1.71 ± 0.08	42.20 ± 1.24	-3.70 ± 1.06
Ly et al. (2007)	0.401 ± 0.010	-1.34 ± 0.06	41.93 ± 0.19	-2.75 ± 0.16
This paper, CDFS	0.245 ± 0.016	-1.33 ± 0.34	41.43 ± 0.22	-2.23 ± 0.32
This paper, S11	0.245 ± 0.016	-1.11 ± 0.51	41.24 ± 0.25	-2.28 ± 0.33

L^* is in $\mathrm{erg\,s^{-1}}$ and ϕ^* in $\mathrm{Mpc^{-3}}$. After Table 5 in Ly et al. (2007).

yield higher faint end counts and thus steeper slopes. This undoubtedly has a similar influence on the faint end slope of the Hα luminosity function.

It is also important to note that any survey using an equivalent width selection (or equivalently, a narrowband−broadband colour, e.g. Fujita et al. 2003 and Ly et al. 2007) will tend to be biased against galaxies with low equivalent widths. This will affect mostly the selection of galaxies with a high star formation rate per unit continuum, such as early type spirals (Kennicutt 1992) and galaxies with low Hα flux in general. The Hα luminosity function, of course, only characterises the line flux on its own.

In Section 4.3.4 we discussed the amount of extinction correction for our survey and concluded that it agrees with values found by other surveys. However, there is still a large spread in the extinction values. A range of $A_{\mathrm{H}\alpha} = 0.5 - 1.8$ is typical of those found (Ly et al. 2007; Kennicutt 1998, and references therein), which translates directly into an uncertainty of 0.3 in $\log L^*$. The exception is when all galaxies have individually been corrected for extinction, which imposes large observational overheads. None of the surveys indicated in Figure 4.8 have been able to do so.

Some surveys have only a limited spectroscopic follow up on their candidates, or none at all (Fujita et al. 2003; Ly et al. 2007). Both of these surveys use additional colour criteria to distinct between Hα and other line emitting galaxies at other redshifts. Ly et al. (2007) estimate that there is about 50 % contamination of [O III] galaxies into the Hα sample of Fujita et al. (2003) based on empirical colour selection using spectra from the Hawaii Hubble Deep Field-North. Spectroscopy on several sources in Ly et al. (2007) shows that slight contamination of higher redshift emission line galaxies occurs in their Hα sample. In our own sample, as we noted in Section 4.3.1, there is a large sample of galaxies that has been selected on their [S II] lines, which would have otherwise been mistaken for low redshift Hα had we relied on colour selection on its own. Furthermore, the fraction of contamination by other emission line galaxies varies significantly with observed line flux (Jones & Bland-Hawthorn 2001; Pascual et al. 2001). Hence, spectroscopic observations of all or a large representative sample of the candidates is vital in understanding the amount of contamination by galaxies at different redshifts.

Most of the surveys correct for the presence of the [N II] lines, which straddle Hα with an observed separation of ~ 44 Å at $z \sim 0.24$. Many surveys targeting Hα are often unable to separate Hα and [N II] if they have insufficient spectral resolution and/or narrowband filters that are too wide. Kewley et al. (2006) show that the majority of star forming galaxies have $\log([\mathrm{N\,II}]/\mathrm{H}\alpha) = -0.5$ ($\mathrm{H}\alpha/[\mathrm{N\,II}] = 3.2$), although this could easily be -1.0 or lower in more extreme cases. Most surveys attempt to correct Hα fluxes for [N II] on an individual basis by means of spectroscopy (Gallego et al. 1995; Sullivan et al. 2000; Pérez-González et al. 2003), the use of Fabry-Perot scans (Hippelein et al. 2003) or an empirical dependence of [N II]/Hα ratio and Hα+[N II] equivalent width (Tresse & Maddox 1998). The

narrowband surveys of Fujita et al. (2003) and Ly et al. (2007) assume a constant flux ratio of Hα/[N II] of 2.3 and 4.66, respectively. Given the spread in ratios of Kewley et al. (2006), they could underestimate the Hα flux by up to 30 % and 15 % corresponding to ~ 0.1 in $\log L^*$. In our case, it is possible for the Hα-[N II] complex to fit entirely within one of our narrowband filters, although this is rare. More likely is that one of the [N II] lines (and maybe part of the Hα line) falls partly into the neighbouring filter or even beyond. Hence, we chose not to correct for the presence of [N II], and this introduces a small (up to 30 %) uncertainty in the line flux, corresponding to 0.1 in $\log L^*$.

Cosmic variance has widely been cited as a major contributor to the differences between various surveys (e.g. Ly et al. 2007). We are well-placed to test the impact of this given that we have observed two distinct fields that have been subjected to identical selection and analysis. We have estimated the contribution of cosmic variance to the mean object densities given by the luminosity functions in Figure 4.8. Following the prescription of Somerville et al. (2004) we determined the relative cosmic variance σ_v^2 for several Hα surveys. The estimate of σ_v is an upper limit as our survey has the shape of an elongated prism, while the derivation is for a spherical volume (Somerville et al. 2004). The cosmic variance is calculated by $\sigma_v = b\sigma_{\rm DM}$, where b is the bias parameter (defined as the ratio of the root variance of the halos and the dark matter) and $\sigma_{\rm DM}^2$ the variance of the dark matter. Using a number density of $0.05\,{\rm Mpc}^{-3}$ (Ly et al. 2007) yields a bias of $b \sim 0.7$ for all surveys at $z \lesssim 0.40$. The corresponding variance over our survey volumes (of 9.4×10^3 and $8.3 \times 10^3\,{\rm Mpc}^3$) is $\sigma_{\rm DM} \sim 0.7$ and thus $\sigma_v = 0.49$. This translates to an uncertainty in $\log \phi(L)$ of $+0.2/-0.3$, which is ample to account for the difference between the luminosity functions of the two fields.

Many of the narrowband surveys exhibit similar uncertainties which are sufficiently large to account for the differences between each other. Table 4.5 shows resulting uncertainty in the number density due to the cosmic variance for a sample of narrowband surveys with well-defined survey volumes. Despite the low redshift, Gallego et al. (1995) span a large enough volume that their uncertainty due to cosmic variance is somewhat lower than the surveys at higher redshift. Comparing the uncertainties $\Delta \log \phi(L)$ to the spread of luminosity functions in Figure 4.8, we observe that cosmic variance is one of the dominating factors in the determination of an average Hα luminosity function at these redshifts.

Finally, we make the observation that there is a high degree of correlation between the three Schechter parameters. This is clearly demonstrated by the confidence limit contours in the bottom panels of Figure 4.7 and the correlation matrices in Table 4.3.

Table 4.5. The survey geometries for a sample of narrowband surveys with well-defined survey volumes alongside their root cosmic variance and the associated uncertainty in the number density.

Reference	Redshift range	Sky area (sq. deg.)	Co-moving volume ($10^3\,\mathrm{Mpc}^{-3}$)	σ_v	$\Delta \log \phi(L)$ ($\phi(L)$ in Mpc^{-3})
Gallego et al. (1995)	$z \leq 0.045$	471	3.3×10^2	0.21	$+0.1/-0.1$
Fujita et al. (2003)	$0.233 \leq z \leq 0.251$	0.255	3.9	0.56	$+0.2/-0.4$
Hippelein et al. (2003)	$0.238 \leq z \leq 0.252$	0.086	1.4	0.70	$+0.2/-0.5$
Ly et al. (2007)	$0.233 \leq z \leq 0.251$	0.255	4.7	0.63	$+0.2/-0.4$
This paper, CDFS field	$0.229 \leq z \leq 0.261$	0.262	9.4	0.49	$+0.2/-0.3$
This paper, S11 field	$0.229 \leq z \leq 0.261$	0.230	8.3	0.49	$+0.2/-0.3$

Root cosmic variance was calculated using the prescription of Somerville et al. (2004) assuming bias $b = 0.7$ and a number density of line emitters of $0.05\,\mathrm{Mpc}^{-3}$, following Ly et al. (2007).

4.4.3 Star Formation Density

The amount of extinction-corrected Hα luminosity from an HII region is directly proportional to the quantity of UV ionising flux produced by newborn stars. As such, it can be used to estimate the number of new stars and hence the star formation rate. We can thus derive global star formation densities from the Hα luminosity densities of Section 4.4.1. We use the star formation rate calibration of Kennicutt (1998),

$$\dot{\rho}\ (\mathrm{M}_\odot\,\mathrm{yr}^{-1}) = 7.9 \times 10^{-42} L(\mathrm{H}\alpha)\ (\mathrm{ergs\,s}^{-1}\,\mathrm{cm}^{-2})\ , \tag{4.9}$$

which assumes a Salpeter initial-mass function, case B recombination and an electron temperature of 10^4 K.

In the case of some surveys (Gallego et al. 2002; Hippelein et al. 2003; Pérez-González et al. 2003; this paper), the faint-end slope of the Hα luminosity function is poorly constrained, thus having important consequences for the integrated luminosity density. To overcome these, and in order to make a fair comparison, we calculate the star formation density of other Hα emission line surveys at the same redshift by assuming a common fixed limit rather than integrating from zero luminosity. We choose $\dot{\rho}_{\mathrm{lim}} = 0.33\,\mathrm{M}_\odot\,\mathrm{yr}^{-1}$, which corresponds to the limit of our survey ($\log F_{\mathrm{lim}} = -16.0$ with F_{lim} in $\mathrm{erg\,s}^{-1}\,\mathrm{cm}^{-2}$, or $\log L_{\mathrm{lim}} = 40.6$ with L_{lim} in $\mathrm{erg\,s}^{-1}$), and avoids faint-end extrapolations or assumed faint-end fits of some other surveys.

Our two fields are indicated in Figure 4.9. The other results included in this Figure are derived in the same way as described with Eq. (4.8) in Section 4.4.1. We included only star formation densities from surveys based on emission lines and transformed onto the same cosmology. The majority of these points were calculated using the compilation of Ly et al. (2007). We also included the least-squares fit to the $z < 1$ points of Hopkins (2004) as a point of reference. Note that this fit assumes $L_{\mathrm{lim}} = 0$.

Observe that the star formation density in both our fields agrees quite well with other Hα emission line surveys at the same redshift. Nevertheless, there is a difference of almost 1 dex between the highest and lowest value for the star formation density. The highest value comes from Fujita et al. (2003), which (according to Ly et al. 2007) suffers from contamination of higher redshift emission line galaxies, pushing their value upwards accordingly. Observe in Figure 4.9 that we have also plotted the star formation density fits of Hopkins (2004) which, unlike the points, make use of star formation density values integrated down to zero luminosity. This serves to illustrate the extent to which extrapolation of the faint end fit affects the final determination of star formation density: typically up to $\lesssim 50\,\%$ for $\alpha \sim -1.3$ (larger for steeper values). As discussed earlier, the luminosity functions of several surveys have ill-constrained faint end values.

Obviously the same systematic uncertainties discussed in Section 4.4.2 will also

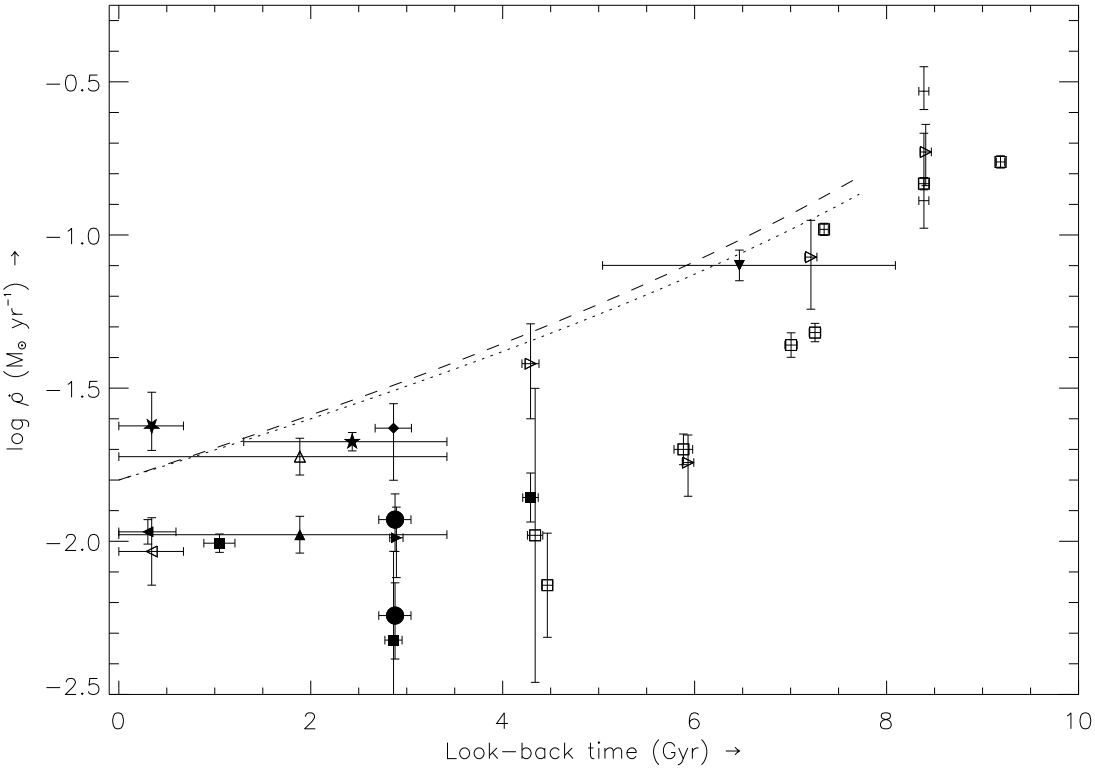

Fig. 4.9: Star formation density as a function of look-back time derived from emission line surveys, where the Schechter function has been integrated from the star formation rate corresponding to the flux limit of our survey, $1 \times 10^{-16}\,\mathrm{erg\,s^{-1}\,cm^{-2}}$ ($0.33\,\mathrm{M_\odot\,yr^{-1}}$). The solid symbols represent the star formation density derived from the Hα line, the open symbols from either the [OII] or [OIII] line. The solid circles are the star formation density from the CDFS and S11 fields of this paper (top and bottom symbol, respectively). Other data are Fujita et al. (2003, open and solid diamonds), Sullivan et al. (2000, open and solid upward-pointing triangle), Tresse et al. (2002, solid downward-pointing triangle), the Ly et al. (2007, open and solid squares), Hippelein et al. (2003, open and solid right-pointing triangles), Gallego et al. (1995, solid left-pointing triangle), Gallego et al. (2002, open left-pointing triangle), Tresse & Maddox (1998, solid upward-pointing star) and Pérez-González et al. (2003, solid downward-pointing star). The dotted and dashed line are the least-squares fit from Figures 1 and 2 of (Hopkins 2004), respectively. They are not corrected for the fact that Hopkins (2004) integrated the Schechter function down to $L = 0\,\mathrm{erg\,s^{-1}}$ and are indicated for comparison purposes only. The parameters used to make this Figure are given in Table 4.4.

play a role here. Furthermore, since we compare the star formation density over a larger redshift range, other emission line star formation indicators have been used (most notably [OII]), thereby introducing their own sources of systematic uncertainty In the case of [OII], extinction corrections are larger and its star formation rate calibrator depends on the abundance of the ionised gas (Kewley et al. 2004). Corrections for both can be made with spectra covering Hα, Hβ and [OIII], as well as [OII]. However, at redshifts $z \gtrsim 0.5$ these lines are progressively lost from the optical, giving rise to uncertainties of up to 0.4 in log(SFR), when applying the Kennicutt (1992) calibrations (Kewley et al. 2004). Beyond this, emission line analyses are pushed into the near-infrared (Glazebrook et al. 1999; Doherty et al. 2006), where brighter night-sky background and instrument thermal contributions increase the difficulty of making observations.

4.5 Environmental Properties

The suppression of star formation rates at the centres of clusters has been well established both through direct observation (Lewis et al. 2002a; Balogh et al. 1997, 1998; Kodama et al. 2001, 2004; Gómez et al. 2003), as well as a changing mix of morphological types (Dressler 1980). Such high density environments provide a range of dynamical mechanisms whereby galaxy encounters rapidly strip gas from any potential star forming galaxies (e.g. Couch et al. 2001, and references therein). Recent observations have suggested a continuation of this trend across structures at larger scales and lower density enhancements than clusters (Gómez et al. 2003; Gray et al. 2004). Accordingly we examine our two fields for evidence of star formation rates that are driven by either the general galaxy environment, or alternatively, the local distribution of star forming galaxies.

Usually, the amount of galaxy clustering is expressed as a function of projected density

$$\Sigma_n = \frac{n}{\pi r_n^2} \ , \tag{4.10}$$

where r_n (in Mpc) is the distance to the nth (usually $n = 10$) nearest neighbouring galaxy with $M_B < -19$. In cluster environments the star formation rate has been observed seems to be quenched at galaxy densities below $1\,\mathrm{Mpc}^{-2}$ (Lewis et al. 2002a; Gómez et al. 2003).

In Figure 4.10(a) we show the fraction of galaxies with a star formation rate exceeding $1\,\mathrm{M}_\odot\,\mathrm{yr}^{-1}$, as well as median and mean star formation rate per galaxy as a function of the projected density of the general galaxy population. This uses data for all of the spectroscopically confirmed star forming galaxies at $z \sim 0.24$ for both of our fields combined. The indicated errorbars in the two top panels were determined using the jackknife estimator[7], while in the bottom panel they

[7] The jackknife estimator is calculated as follows. Let $\hat{\rho}_{(i)} = \hat{\rho}(x_1, \ldots, x_{i-1}, x_{i+1}, \ldots, x_n)$ be the value of the statistic with one element x_i removed, and define $\hat{\rho}_{(\cdot)} = (1/n)\sum_{i=1}^{n} \hat{\rho}_{(i)}$. Then

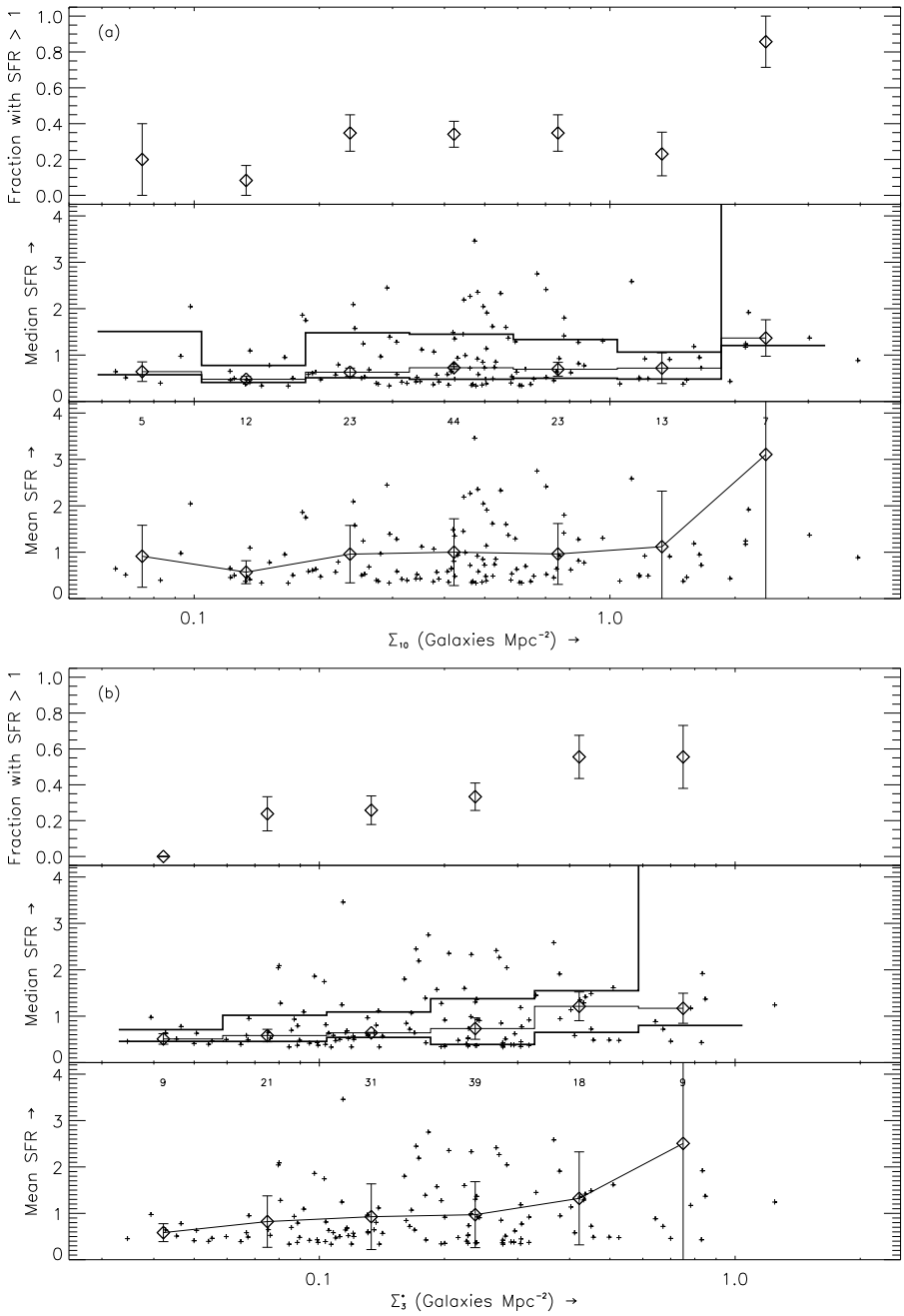

Fig. 4.10: (*a*) The mean and median star formation rate per galaxy (in $\mathrm{M}_\odot\,\mathrm{yr}^{-1}$) and the fraction of galaxies with a star formation rate $> 1\,\mathrm{M}_\odot\,\mathrm{yr}^{-1}$ as a function of the projected density Σ_{10} of ordinary galaxies (taken from the COMBO-17 survey). The errorbars in the two top panels are the jackknife estimates of the standard error, while in the bottom panel they are standard deviations. The small crosses indicate the values for each individual star forming galaxy. The thick lines in the middle panel indicate the 25th and 75th percentile for each bin. The numbers in the bottom panel indicate the number of galaxies included in each point. (*b*) Same as (*a*), but as a function of star forming galaxy density Σ_3^*.

are the standard deviation. We also show the 25th and 75th percentile values for each bin in the middle panel. We determined the projected density by using the usual r_{10} measure of the tenth-nearest star forming galaxy to each ordinary galaxy. Ordinary galaxies were taken from the photometric redshift catalogues of the COMBO-17 survey (Wolf et al. 2003, K. Meisenheimer, priv. comm.) as galaxies with $B_{AB} < 22$ (corresponding to $M_B = -19$) between $0.21 \leq z \leq 0.29$. As the thickness of the redshift slice influences the value of projected density, we scale it using the difference in the thickness of the redshift slice of our survey and the average thickness of the 3σ cluster volumes (where σ is the velocity dispersion of the cluster) used in Lewis et al. (2002a).

Since we did not target any known clusters with our fields, we expect that there will be little or no evidence for star formation suppression in our fields. Typically, the projected density for galaxies within the virial radius of a cluster is $\sim 4\,\mathrm{Mpc}^{-2}$ and at the centre of some rich clusters can be as high as $10\,\mathrm{Mpc}^{-2}$ (Lewis et al. 2002a). Indeed, as Figure 4.10(a) shows, there is negligible change in the star formation rate per unit density for the galaxies in both our fields (noting that the highest density point is affected by poor number statistics). Furthermore, we confirm levels of star formation that are typical for the range of typical field galaxy densities probed by our data as found by previous surveys (e.g. Lewis et al. 2002a; Gómez et al. 2003). Generally, the distribution of star formation rates in a given density bin is rather asymmetric, making the median a more reliable measure than the mean.

In Figure 4.10(b) we show the same measures as for (a), but as a function of projected density of the spectroscopically confirmed star forming galaxies at $0.23 \leq z \leq 0.26$. There are roughly one-third as many star forming galaxies as not, and so we redefine the projected density in terms of distance to the third-nearest galaxy, Σ_3^*. As a consequence, Σ_3^* and Σ_{10} span a similar range of density values. We observe in Figure 4.10(b) that star formation per galaxy increases with increasing density. Noting again that the highest density bin is affected by poor number statistics. Although not conclusive, this is consistent with galaxy evolution scenarios that see galaxy-galaxy interactions as triggers for bursts of star formation (Alonso et al. 2004; Perez et al. 2006).

To examine the apparent relationship between star formation rate and projected density of star forming galaxies, in Figure 4.11 we plot the spatial distribution of our spectrally confirmed Hα galaxies. The size of the points indicates their star formation rate and their shade of grey the redshift. Probable (but unconfirmed) Hα candidates are also shown. These were selected on the basis of colour ($0.5 \leq (B - R) \leq 1.3$; see Figure 4.2) and having either indeterminate or non-existent spectra.

$\hat{\sigma}_J^2 = (n-1)/n \sum_{i=1}^{n} (\hat{\rho}_{(i)} - \hat{\rho}_{(\cdot)})^2$ is the square of the jackknife estimate of standard error (Efron & Gong 1983).

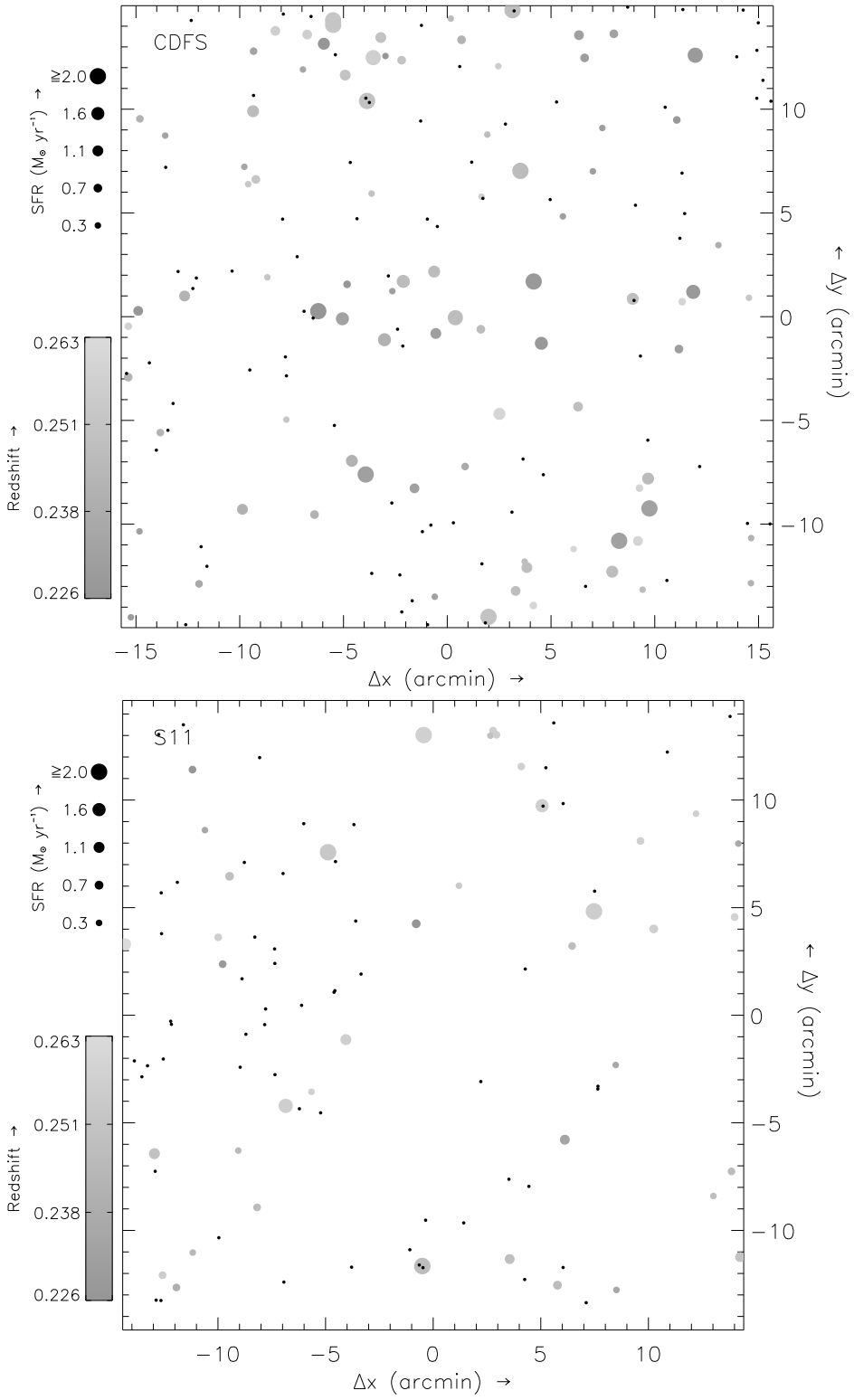

Fig. 4.11: Spatial distribution of the spectrally confirmed Hα galaxies in both our fields (*solid circles*). The size of the circles indicates the star formation rate of the galaxy derived from the narrowband flux and the grey-scale the redshift. The black dots are galaxies that have not been spectroscopically confirmed yet and have a colour $0.5 \leq (B-R) \leq 1.3$, which corresponds to the colour interval of our confirmed Hα galaxies (Figure 4.2).

The distribution of star forming galaxies in the CDFS field (Figure 4.10b) suggests a tendency for grouping of the star forming galaxies. However, the eye is remarkably good at making out patterns in noisy distributions and thus we should be cautious in these interpretations (e.g. p35 of Peebles 1993). On the other hand, the distribution of star forming galaxies at $z \sim 0.24$ in the S11 field (Figure 4.11) is apparently less structured than the CDFS. Because of this, we infer that the trend of increasing star formation with rising density of star forming galaxies is largely attributable to the data from the CDFS field. This contrast between the fields can also be seen in differences in the Hα space-densities given by the two luminosity functions in Figure 4.7. As a consequence, the star formation density of the S11 field is lower than that of the CDFS (Figure 4.8). This is due to the lower Hα fraction in the S11 field compared to the CDFS field (Figure 4.5), to the extend that can be seen given the more limited spectroscopy on the former.

A more robust approach would be the derivation of two-point correlation statistics of the star forming galaxies, which could directly test for clustering tendencies in the CDFS field compared to S11. Such analyses are beyond the scope of this paper, but will be addressed in a future work.

4.6 Summary and Conclusions

In this paper we report the results of a survey for Hα emitting galaxies at $z \sim 0.24$. We used two fields from the Wide Field Imager Lyman Alpha Search (WFILAS). It consists of imaging in three narrowband filters ($FWHM = 70$ Å), an encompassing intermediate band filter ($FWHM = 220$ Å), supplemented with broadband B and R. The narrowband filters cover a redshift range of $0.23 \lesssim z \lesssim 0.26$ for Hα galaxies. These galaxies were selected by having an excess flux in one of the narrowband over to the other two, while also being detected in the intermediate and broadband R filters. This yielded a total of 707 candidate emission line galaxies (after the removal of stellar contaminants) for both fields.

We have confirmed that around half of these galaxies are Hα at $z \sim 0.24$ through spectroscopic follow-up of 206 candidates. A significant number of galaxies were also found at $z \sim 0.21$ by means of their [S II] emission. Other galaxies found were [OII] and Hβ/[OIII] emitters at $z \sim 1.2$ and $z \sim 0.6 - 0.7$, respectively. Through use of the spectroscopy, we refined our colour selection to account for galaxies with a single emission line, leading to a measure of the fraction of Hα galaxies as a function of narrowband flux in both of these regions of the sky. We also used the spectroscopy to determine a generic extinction correction using the Balmer decrement.

We have determined the Hα luminosity function at $z \sim 0.24$ separately for both of our fields after correcting for imaging and spectroscopic incompleteness, extinction and contamination from interlopers. We find small differences in their slope and turn-over luminosity while their normalisations were the same. When

compared to recent Hα surveys, there is remarkable agreement between the luminosity function of our CDFS field with that one the Fabry-Perot imaging survey of Hippelein et al. (2003). Differences between our fields were of the order expected by cosmic variance but less than the scatter between the Hα luminosity functions of recent surveys. We surmise that while cosmic variance is a major contributor to this scatter, it is differences in methodology between surveys (mainly differences in selection criteria) that discrepancies between Hα luminosity functions and its related observables at $z \sim 0.24$. A survey that covers $10 - 20\times$ the volume of one of our fields is required to get the uncertainty due to cosmic variance to the levels of Gallego et al. (1995).

We estimated the star formation density for both our fields to be $\log \dot{\rho} = -1.93^{+0.08}_{-0.10}$ and $-2.24^{+0.11}_{-0.14}$ ($\dot{\rho}$ in $\mathrm{M}_\odot\,\mathrm{yr}^{-1}$) for the CDFS and S11 fields, respectively, down to our survey limit of $\log F_{\mathrm{line}} = -16.0$ (F_{line} in $\mathrm{erg\,s^{-1}\,cm^{-2}}$) or $\log L_{\mathrm{line}} = 40.6$ (L_{line} in $\mathrm{erg\,s^{-1}}$). These values are comparable to other surveys at this redshift when calculated to the same flux limit.

We explored the amount of star formation with respect to the local environment and found that the star formation rates were typical for the field galaxy densities probed, in agreement with the results of previous work. However, we also found tentative evidence of an increase in star formation rate per galaxy with increasing density of the star forming galaxies. This supports scenarios where merger events are triggers for enhanced star formation, provided it can be demonstrated to be occurring on the smallest scales. We explored this trend by examining the spatial distribution of our fields individually and found that it was largely attributable to one field. A formal study of the clustering statistics of this field is required to confirm this and will be the subject of a future study.

Acknowledgements

We are indebted to Rob Sharp for his suggestions on preparing and reducing the AAOmega observations and for his help during the observations. We are also grateful to AAO service observers Will Saunders and Quentin Parker. We thank Klaus Meisenheimer for providing us with the photometric redshift catalogue of the S11 field. E.W. is grateful to Philip Lah for help with Schechter function fitting. This research was made possible by using European Southern Observatory and Anglo-Australian Observatory facilities.

References

Ajiki, M., Taniguchi, Y., Fujita, S. S., Shioya, Y., Nagao, T., Murayama, T., Yamada, S., Umeda, K., et al., 2003, AJ, 126, 2091

Alonso, M. S., Tissera, P. B., Coldwell, G., & Lambas, D. G., 2004, MNRAS, 352, 1081

Baldry, I. K. & Glazebrook, K. 2003, ApJ, 593, 258

Balogh, M. L., Morris, S. L., Yee, H. K. C., Carlberg, R. G., & Ellingson, E., 1997, ApJ, 488, L75+

Balogh, M. L., Schade, D., Morris, S. L., Yee, H. K. C., Carlberg, R. G., & Ellingson, E., 1998, ApJ, 504, L75+

Bertin, E. & Arnouts, S. 1996, A&AS, 117, 393

Bessell, M. S. 1999, PASP, 111, 1426

Calzetti, D. 2001, PASP, 113, 1449

Cole, S., Norberg, P., Baugh, C. M., Frenk, C. S., Bland-Hawthorn, J., Bridges, T., Cannon, R., Colless, M., et al.,

Condon, J. J. 1992, ARA&A, 30, 575

Couch, W. J., Balogh, M. L., Bower, R. G., Smail, I., Glazebrook, K., , & Taylor, M., 2001, ApJ, 549, 820

Cowan, G. 1998, Statistical data analysis (Oxford University Press)

Daigne, F., Olive, K. A., Silk, J., Stoehr, F., & Vangioni, E., 2006, ApJ, 647, 773

Doherty, M., Bunker, A., Sharp, R., Dalton, G., Parry, I., & Lewis, I., 2006, MNRAS, 370, 331

Dressler, A. 1980, ApJ, 236, 351

Efron, B. & Gong, G. 1983, The American Statistician, 37, 36

Fardal, M. A., Katz, N., Weinberg, D. H., & Dav'e, R., 2006, astro-ph/0604534

Fujita, S. S., Ajiki, M., Shioya, Y., Nagao, T., Murayama, T., Taniguchi, Y., Umeda, K., Yamada, S., et al., 2003, ApJ, 586, L115

Gal-Yam, A. & Maoz, D. 2004, MNRAS, 347, 942

Gallego, J., García-Dabó, C. E., Zamorano, J., Aragón-Salamanca, A., & Rego, M., 2002, ApJ, 570, L1

Gallego, J., Zamorano, J., Aragon-Salamanca, A., & Rego, M., 1995, ApJ, 455, L1+

Gawiser, E., van Dokkum, P. G., Gronwall, C., Ciardullo, R., Blanc, G. A., Castander, F. J., Feldmeier, J., Francke, H., et al.,

Glazebrook, K., Blake, C., Economou, F., Lilly, S., & Colless, M., 1999, MNRAS, 306, 843

Gómez, P. L., Nichol, R. C., Miller, C. J., Balogh, M. L., Goto, T., Zabludoff, A. I., Romer, A. K., Bernardi, M., et al., 2003, ApJ, 584, 210

Gray, M. E., Wolf, C., Meisenheimer, K., Taylor, A., Dye, S., Borch, A., & Kleinheinrich, M., 2004, MNRAS, 347, L73

Heavens, A., Panter, B., Jimenez, R., & Dunlop, J., 2004, Nature, 428, 625

Hippelein, H., Maier, C., Meisenheimer, K., Wolf, C., Fried, J. W., von Kuhlmann, B., Kümmel, M., Phleps, S., et al., 2003, A&A, 402, 65

Hopkins, A. M. 2004, ApJ, 615, 209

Hopkins, A. M. & Beacom, J. F. 2006, ApJ, 651, 142

Hopkins, A. M., Miller, C. J., Nichol, R. C., Connolly, A. J., Bernardi, M., Gómez, P. L., Goto, T., Tremonti, C. A., et al., 2003, ApJ, 599, 971

Hu, E. M., Cowie, L. L., Capak, P., McMahon, R. G., Hayashino, T., & Komiyama, Y., 2004, AJ, 127, 563

Jansen, R. A., Franx, M., & Fabricant, D., 2001, ApJ, 551, 825

Jones, D. H. & Bland-Hawthorn, J. 2001, ApJ, 550, 593

Jones, D. H., Peterson, B. A., Colless, M., & Saunders, W., 2006, MNRAS, 369, 25

Jones, D. H., Saunders, W., Colless, M., Read, M. A., Parker, Q. A., Watson, F. G., Campbell, L. A., Burkey, D., et al.,

Juneau, S., Glazebrook, K., Crampton, D., McCarthy, P. J., Savaglio, S., Abraham, R., Carlberg, R. G., Chen, H.-W., et al., 2005, ApJ, 619, L135

Kennicutt, Jr., R. C. 1992, ApJ, 388, 310

—. 1998, ARA&A, 36, 189

Kewley, L. J., Dopita, M. A., Sutherland, R. S., Heisler, C. A., & Trevena, J., 2001, ApJ, 556, 121

Kewley, L. J., Geller, M. J., & Jansen, R. A., 2004, AJ, 127, 2002

Kewley, L. J., Groves, B., Kauffmann, G., & Heckman, T., 2006, MNRAS, 372, 961

Kodama, T., Balogh, M. L., Smail, I., Bower, R. G., & Nakata, F., 2004, MNRAS, 354, 1103

Kodama, T., Smail, I., Nakata, F., Okamura, S., & Bower, R. G., 2001, ApJ, 562, L9

Lewis, I., Balogh, M., De Propris, R., Couch, W., Bower, R., Offer, A., Bland-Hawthorn, J., Baldry, I. K., et al.,

Lewis, I. J., Cannon, R. D., Taylor, K., Glazebrook, K., Bailey, J. A., Baldry, I. K., Barton, J. R., Bridges, T. J., et al.,

Lilly, S. J., Le Fevre, O., Hammer, F., & Crampton, D., 1996, ApJ, 460, L1+

Ly, C., Malkan, M. A., Kashikawa, N., Shimasaku, K., Doi, M., Nagao, T., Iye, M., Kodama, T., et al., 2007, ApJ, 657, 738

Madau, P., Ferguson, H. C., Dickinson, M. E., Giavalisco, M., Steidel, C. C., & Fruchter, A., 1996, MNRAS, 283, 1388

Madgwick, D. S., Lahav, O., Baldry, I. K., Baugh, C. M., Bland-Hawthorn, J., Bridges, T., Cannon, R., Cole, S., et al.,

Massarotti, M., Iovino, A., & Buzzoni, A., 2001, ApJ, 559, L105

Mendoza, C. 1983, in IAU Symposium, Vol. 103, Planetary Nebulae, ed. D. R. Flower, 143–172

Miszalski, B., Shortridge, K., Saunders, W., Parker, Q. A., & Croom, S. M., 2006, MNRAS, 371, 1537

Oke, J. B. & Gunn, J. E. 1983, ApJ, 266, 713

Panter, B., Heavens, A. F., & Jimenez, R., 2003, MNRAS, 343, 1145

Pascual, S., Gallego, J., Aragón-Salamanca, A., & Zamorano, J., 2001, A&A, 379, 798

Pascual, S., Gallego, J., & Zamorano, J., 2007, PASP, 119, 30

Peebles, P. J. E. 1993, Principles of physical cosmology (Princeton Series in Physics, Princeton, NJ: Princeton University Press, —c1993)

Pei, Y. C. & Fall, S. M. 1995, ApJ, 454, 69

Pei, Y. C., Fall, S. M., & Hauser, M. G., 1999, ApJ, 522, 604

Perez, M. J., Tissera, P. B., Lambas, D. G., & Scannapieco, C., 2006, A&A, 449, 23

Pérez-González, P. G., Zamorano, J., Gallego, J., Aragón-Salamanca, A., & Gil de Paz, A., 2003, ApJ, 591, 827

Rhoads, J. E., Xu, C., Dawson, S., Dey, A., Malhotra, S., Wang, J., Jannuzi, B. T., Spinrad, H., et al., 2004, ApJ, 611, 59

Rix, H.-W., Barden, M., Beckwith, S. V. W., Bell, E. F., Borch, A., Caldwell, J. A. R., Häussler, B., Jahnke, K., et al., 2004, ApJS, 152, 163

Rosa-González, D., Terlevich, E., & Terlevich, R., 2002, MNRAS, 332, 283

Rosati, P., Tozzi, P., Giacconi, R., Gilli, R., Hasinger, G., Kewley, L., Mainieri, V., Nonino, M., et al., 2002, ApJ, 566, 667

Schaerer, D. 2000, in Building Galaxies; from the Primordial Universe to the Present, ed. F. Hammer, T. X. Thuan, V. Cayatte, B. Guiderdoni, & J. T. Thanh Van, 389–+

Schechter, P. 1976, ApJ, 203, 297

Sharp, R., Saunders, W., Smith, G., Churilov, V., Correll, D., Dawson, J., Farrel, T., Frost, G., et al., 2006, in Ground-based and Airborne Instrumentation for Astronomy. Edited by Ian S. McLean and Masanori Iye. Proceedings of the SPIE, Volume 6269, pp

Somerville, R. S., Lee, K., Ferguson, H. C., Gardner, J. P., Moustakas, L. A., & Giavalisco, M., 2004, ApJ, 600, L171

Somerville, R. S., Primack, J. R., & Faber, S. M., 2001, MNRAS, 320, 504

Sullivan, M., Treyer, M. A., Ellis, R. S., Bridges, T. J., Milliard, B., & Donas, J., 2000, MNRAS, 312, 442

Thomas, D., Maraston, C., Bender, R., & Mendes de Oliveira, C., 2005, ApJ, 621, 673

Tresse, L. & Maddox, S. J. 1998, ApJ, 495, 691

Tresse, L., Maddox, S. J., Le Fèvre, O., & Cuby, J.-G., 2002, MNRAS, 337, 369

Treyer, M. A., Ellis, R. S., Milliard, B., Donas, J., & Bridges, T. J., 1998, MNRAS, 300, 303

Westra, E., Jones, D. H., Lidman, C. E., Athreya, R. M., Meisenheimer, K., Wolf, C., Szeifert, T., Pompei, E., et al., 2005, A&A, 430, L21

Westra, E., Jones, D. H., Lidman, C. E., Meisenheimer, K., Athreya, R. M., Wolf, C., Szeifert, T., Pompei, E., et al., 2006, A&A, 455, 61

Williams, R. E., Blacker, B., Dickinson, M., Dixon, W. V. D., Ferguson, H. C., Fruchter, A. S., Giavalisco, M., Gilliland, R. L., et al., 1996, AJ, 112, 1335

Wolf, C., Meisenheimer, K., Rix, H.-W., Borch, A., Dye, S., & Kleinheinrich, M., 2003, A&A, 401, 73

Zacharias, N., Urban, S. E., Zacharias, M. I., Wycoff, G. L., Hall, D. M., Monet, D. G., & Rafferty, T. J., 2004, AJ, 127, 3043

5. SUMMARY AND FUTURE WORK

In this thesis seven Lyα-emitting galaxy candidates at $z \sim 5.7$ were identified by the Wide Field Imager Lyman Alpha Search (WFILAS). Three fields were observed with customised intermediate and narrowband filters together with standard broadband filters B and R, using the Wide Field Imager on the ESO/MPI 2.2 m telescope. This sample of luminous ($L_{\mathrm{Ly}\alpha} \geq 1.8 \times 10^{43}\,\mathrm{erg\,s^{-1}}$) candidates complements those of other recent surveys by constraining the bright end of the Lyα luminosity function at these redshifts. Combining the sources with those of Ajiki et al. (2003) increased the luminosity density at $z \sim 5.7$ by $\sim 30\,\%$. One of the three observed fields was the well-studied Chandra Deep Field South (CDFS). The three WFILAS candidates identified in this field were located nearby one another, supporting evidence for an overdensity of $z \sim 5.7$ galaxies detected by other groups.

Two candidates have been confirmed as Lyα emission-line galaxies through spectroscopy using FORS2 on the VLT. One of these is the most luminous Lyα emitter at this redshift to date. Imaging taken under excellent seeing conditions with an intermediate band filter at 8150 Å showed both galaxies to be unresolved ($FWHM < 0\farcs5$). Spectroscopy revealed an asymmetric emission profile for both objects, thus confirming its identification as high redshift Lyα. Furthermore, both objects exhibited the presence of a tentative second Lyα component redward of the line, suggesting an expanding shell of neutral hydrogen surrounding the central source.

Although numerous Lyα-emitting galaxies have now been found at $z \sim 5.7$ and beyond, relatively little is known of their nature. At $z \sim 3$ they appear to be very young objects of low stellar mass, moderate star formation and little dust (Kudritzki et al. 2000; Gawiser et al. 2006). For galaxies at $z \sim 5.7$, similar analyses using spectral energy distribution fitting have thus far been unable to break the degeneracy between the age of the stellar population and type of star formation history (Lai et al. 2007). Future observations in the near- and far-infrared will measure (or place upper limits on) the spectral energy distributions of these sources in the rest-frame optical (e.g. Eyles et al. 2007), thereby differentiating between populations of different ages.

The two confirmed Lyα emission-line galaxies from this thesis are ideal objects for further detailed study given their bright line luminosities for this redshift. The metallicities of both objects have already been constrained to less than $0.1 Z_{\odot}$ using

near-infrared spectroscopy from SINFONI on the VLT (C. Lidman, priv. comm.). The absence of any metal lines redward of Lyα given the strength known of the latter places tighter constraints on metallicity than would be possible with fainter sources. Ongoing follow-up observations of these two objects will give a better indication of the types of stellar populations present in galaxies at this redshift.

Neither of the two spectroscopically confirmed Lyα-emitting galaxies from WFILAS have a secure detection of the rest-frame UV continuum redwards of the Lyα line. This gives a lower limit of ~ 250 Å for their equivalent widths, based on a $1\,\sigma$ upper limit for their continuum. Future deep optical spectroscopy could potentially further constrain the strength of the continuum. High Lyα equivalent widths are potentially indicative of a top-heavy initial mass function due to Population III stars (Malhotra & Rhoads 2002; Gawiser et al. 2006), although such measurements are difficult to make.

Finally, deeper spectroscopy of the Lyα line than what is available at present would permit better modelling of the emission profile. This could yield further insight into the local environment of the Lyα source, in light of recent models which suggest the possibility of gas infall in Lyα emitters (Dijkstra et al. 2006). Furthermore, deep spectroscopy could potentially detect the N v $\lambda\lambda$1239,1243 doublet, thereby allowing an independent determination of redshift, unaffected by intervening absorption in the same way as the blue side of Lyα. Prior knowledge of the true central wavelength of Lyα in the observed frame provides a vital constraint for modelling the line profile.

In the second part of this thesis, the WFILAS survey data were also used to identify emission line galaxies at lower redshifts, in particular Hα at $z \sim 0.24$. Spectroscopic follow-up (using AAOmega on the AAT) was used to determine the fraction of Hα emitters and derive the average extinction corrections subsequently applied to all candidates. The Hα luminosity function was constructed separately for each field and fitted with Schechter functions. It was found that systematic uncertainties – most notably, cosmic variance and differences in survey selection criteria – remain the dominant sources of uncertainty between different Hα luminosity functions at $z \lesssim 0.4$. The influence of the environment on galaxy star formation rate was also investigated. Given the typical field galaxy densities sampled by our two fields, the global rates of star formation were consistent with previous results. However, when compared to the projected density of the star-forming population alone, a tentative increase in star formation rate was found with increasing density. This supports scenarios which involve galaxy-galaxy interactions as triggers for star formation, provided it can be demonstrated to occur on small enough scales. This will be a focus of future work on these data, specifically, by deriving two-point correlation statistics for both fields.

References

Ajiki, M., Taniguchi, Y., Fujita, S. S., Shioya, Y., Nagao, T., Murayama, T., Yamada, S., Umeda, K., et al., 2003, AJ, 126, 2091

Dijkstra, M., Haiman, Z., & Spaans, M., 2006, ApJ, 649, 37

Eyles, L. P., Bunker, A. J., Ellis, R. S., Lacy, M., Stanway, E. R., Stark, D. P., & Chiu, K., 2007, MNRAS, 374, 910

Gawiser, E., van Dokkum, P. G., Gronwall, C., Ciardullo, R., Blanc, G. A., Castander, F. J., Feldmeier, J., Francke, H., et al., 2006, ApJ, 642, L13

Kudritzki, R.-P., Méndez, R. H., Feldmeier, J. J., Ciardullo, R., Jacoby, G. H., Freeman, K. C., Arnaboldi, M., Capaccioli, M., et al., 2000, ApJ, 536, 19

Lai, K., Huang, J.-S., Fazio, G., Cowie, L. L., Hu, E. M., & Kakazu, Y., 2007, ApJ, 655, 704

Malhotra, S. & Rhoads, J. E. 2002, ApJ, 565, L71